



Universidade Federal  
de São João del-Rei

FEDERAL CENTER FOR TECHNOLOGICAL EDUCATION OF MINAS GERAIS  
GRADUATE PROGRAM IN ELECTRICAL ENGINEERING  
BROAD ASSOCIATION BETWEEN CEFET-MG AND UFSJ

# **MAGNETO-INDUCTIVE WAVES IN METAMATERIAL-BASED WIRELESS POWER TRANSFER SYSTEMS**

**FELIPE MACHADO DE FREITAS**

Supervisor: Prof. Dr. Sandro Trindade Mordente Gonçalves

BELO HORIZONTE  
MAY 2023

**FELIPE MACHADO DE FREITAS**

**MAGNETO-INDUCTIVE WAVES IN  
METAMATERIAL-BASED WIRELESS POWER TRANSFER  
SYSTEMS**

Dissertation presented to the Graduate Program in Electrical Engineering at the Federal Center for Technological Education of Minas Gerais as a partial requirement for obtaining the Master's degree in Electrical Engineering.

Concentration Area: Electrical Systems.

Research Line: Applied Electromagnetism.

Supervisor: Prof. Dr. Sandro Trindade Mordente Gonçalves

FEDERAL CENTER FOR TECHNOLOGICAL EDUCATION OF MINAS GERAIS  
GRADUATE PROGRAM IN ELECTRICAL ENGINEERING  
BROAD ASSOCIATION BETWEEN CEFET-MG AND UFSJ  
BELO HORIZONTE  
MAY 2023

F866m Freitas, Felipe Machado de  
Magneto-inductive waves in metamaterial-based wireless power transfer systems / Felipe Machado de Freitas. – 2023.  
89 f.: il., gráfs, tabs., fotos.

Dissertação de mestrado apresentada ao Programa de Pós-Graduação em Engenharia Elétrica em associação ampla entre a UFSJ e o CEFET-MG.

Orientador: Sandro Trindade Mordente Gonçalves.

Banca examinadora: Sandro Trindade Mordente Gonçalves, Christian Voltaire, Márcio Matias Afonso.

Dissertação (mestrado) – Centro Federal de Educação Tecnológica de Minas Gerais.

1. Circuitos eletrônicos – Modelos – Teses. 2. Materiais eletrônicos – Teses. 3. Materiais magnéticos – Teses. 4. Transmissão de energia sem fio – Teses. I. Gonçalves, Sandro Trindade Mordente. II. Centro Federal de Educação Tecnológica de Minas Gerais. III. Universidade Federal de São João del-Rei. IV. Título.

CDD 621.3815



FEDERAL UNIVERSITY OF SÃO JOÃO DEL REI  
PRO-RECTORY OF RESEARCH AND GRADUATE STUDIES  
FEDERAL CENTER OF TECHNOLOGICAL EDUCATION OF MINAS GERAIS  
DIRECTORATE OF RESEARCH AND POST-GRADUATION  
GRADUATE PROGRAM IN ELECTRICAL ENGINEERING



**Felipe Machado de Freitas**

**"Magneto-Inductive Waves in Metamaterial-Based Wireless Power Transfer Systems"**

Dissertation n° 298 presented to the Pós-Graduate Program in Electrical Engineering – Broad Association between the Federal University of São João Del-Rei and the Federal Center for Technological Education of Minas Gerais on May 26, 2023 as a partial requirement to obtain the title of Master in Electrical Engineering, approved by the Examining Board constituted by the professors:

---

Prof. Dr. Sandro Trindade Mordente Gonçalves (Advisor)  
Federal Center for Technological Education of Minas Gerais

*Département Electronique  
Electrotechnique, Automatique  
Ecole Centrale de Lyon  
36, avenue Guy de Collongue  
69130 - ECULLY Cédex - France*

---

Prof. Dr. Christian Vollaire  
École Centrale de Lyon / Ampère Laboratory

---

Prof. Dr. Marcio Matias Afonso  
Federal Center for Technological Education of Minas Gerais

Dedico este trabalho aos meus pais Adão e Maria Aparecida e ao meu grande parceiro Ícaro.

# Acknowledgements

I'm deeply grateful to God for being the light in this research journey.

To my parents, Adão and Maria Aparecida, for their support and dedication, for dreaming of me, and for being a powerful source of motivation. They are, to me, examples of perseverance and dedication.

I am grateful to my advisor, Prof. Dr. Sandro Trindade Mordente Gonçalves, for his precious advice. More than an advisor, he is a source of motivation and inspiration. I hope to collaborate and research together in future projects.

To Ícaro Veloso, for his partnership and presence during the research time in France and Brazil. His support was extremely important; I'm very grateful.

I would like to thank the people who supervised and participated in the realization of this research project. First of all, my supervisors: Christian Vollaire, Arnaud Bréard, and Laurent Krähenbühl, professor-researchers from the Ampère laboratory, for their kindness, their advice, and their availability. Furthermore, I'm grateful to my supervisor Denys Nikolayev, and the Bioelectronics group at IETR for support in the internship in this renowned laboratory. Finally, I also thank the Ampère and IETR Laboratories employees for dealing with the documentation and the administrative steps so that the internship could take place.

I would like to express my deepest gratitude to my family and friends. I am immensely grateful to all the people who helped me in this research project and with whom it was fascinating to discuss and work. I would like to thank, especially IBBx Inovação, the company I worked for during the first year of my master's degree and which gave me the necessary support to monitor the activities of the research project.

To CEFET-MG for promoting this research and allowing me to go from Brazil to France, my stay there in France during the internship period, and for my return to Brazil. I would like to thank the professors who shared knowledge and contributed to this research. And to all the employees who maintain this institution of excellence.

To CNPq, CAPES, and FAPEMIG, for promoting scientific research in Brazil and Minas Gerais.

*“A hundred times every day I remind myself that my inner and outer life depend on the labours of other men, living and dead, and that I must exert myself in order to give in the same measure as I have received and am still receiving.”*

(Albert Einstein, *The World As I See It*)

# Abstract

This work proposes a method of analysis of printed *Magnetic Coupled Wireless Power Transfer* (MCWPT) systems operating in a few MHz based on Circuit Model (CM). Initially, the effect of resonant surfaces on wireless energy transmission and the advantages of their use are discussed. Therefore, the resulting increase in efficiency is discussed based on the *Magneto-Inductive Waves* (MIW) theory. Furthermore, the feasibility of using metasurfaces in *Wireless Power Transfer* (WPT) systems where the transmitter and receiver are misaligned or are coplanar is analyzed. Finally, possibilities for optimizing the impedance of WPT systems to increase transmission efficiency are also presented.

An analytical model is proposed to calculate the self-inductance of printed inductors, their characteristic resistance, and the mutual inductance between coils. The presented formulation for calculating the mutual inductance between inductors is based on Neumann's formula. Due to the generality of this approach, it can also be applied to more complex structures, such as metasurfaces. In the analysis of the MCWPT CM, it is considered that the unknown current along the microstrip is considered as a single value distributed in each modeled coil. First, computational aspects related to model implementation are discussed. Then, the calculated results are compared step by step with commercial software based on electromagnetic methods in the frequency domain. Then, the microstrip model is experimentally validated with measurements of transmission coefficients from an MCWPT printed in FR4, operating at  $24\text{MHz}$ . A new design based on printed square coils is also proposed, but now with reduced size and working at  $13.56\text{MHz}$ . A frequency domain analysis on how the frequency and receiver position on the metasurface affect efficiency is done. Then, the variation of the input impedance and the current distribution on the surface of the metamaterial are analyzed in relation to the variations in the position of the receiver and in the charge rate on the resonant surface. For this, the MIW theory is used in a specific application: Passive Position Tracking in Dynamic MCWPT Systems. Finally, it discusses the importance of knowing the current distribution and impedance optimization parameters for an MCWPT system.

The results show that the proposed method is valid for modeling printed inductors. In addition, the model proved to be computationally more efficient for the analysis of large systems when compared to commercial full-wave simulation software, and the practical results point to conformity.

**Keywords:** Circuit model, magnetic metamaterial, MIW, near field coupling, wireless power transfer.



# Resumo

Este trabalho propõe um método de análise de sistemas *Magnetic Coupled Wireless Power Transfer* (MCWPT) impressos operando em poucos MHz baseado em Modelo de Circuito (CM). Inicialmente discute-se o efeito das superfícies ressonantes na transmissão de energia sem fio e as vantagens de seu uso. Logo, o consequente aumento de eficiência é discutido com base na teoria de *Magneto-Inductive Waves* (MIW). Além disso, é analisada a viabilidade do uso de metasuperfícies em sistemas *Wireless Power Transfer* (WPT) onde o transmissor e o receptor estão desalinhados ou são coplanares. São apresentadas, também, possibilidades de otimização da impedância dos sistemas WPT para aumentar a eficiência da transmissão.

Um modelo analítico é proposto para calcular a auto-indutância de indutores impressos, sua resistência característica e a indutância mútua entre bobinas. A formulação apresentada para o cálculo da indutância mútua entre indutores é baseada na fórmula de Neumann. Devido à generalidade desta abordagem, ela também pode ser aplicada a estruturas mais complexas, como metasuperfícies. Na análise do CM do MCWPT, considera-se que a corrente desconhecida ao longo da microfita é considerada como um único valor distribuído em cada bobina modelada. Primeiramente, são discutidos aspectos computacionais relacionados à implementação do modelo. Em seguida, os resultados calculados são comparados passo a passo com software comercial baseado em métodos eletromagnéticos no domínio da frequência. Em seguida, o modelo de microstrip é validado experimentalmente com medições de coeficientes de transmissão de um MCWPT impresso em FR4, operando em  $24\text{MHz}$ . Além disso, é proposto um novo design baseado em bobinas quadradas impressas, mas agora com tamanho reduzido e operando a  $13,56\text{MHz}$ . Com este sistema realiza-se uma análise no domínio da frequência sobre como a frequência e a posição do receptor sobre a metasuperfície afetam a eficiência. Em seguida, analisa-se a variação da impedância de entrada e a distribuição de corrente na superfície do metamaterial em relação às variações na posição do receptor e na taxa de carga na superfície ressonante. Para isso, a teoria de MIW é utilizada em aplicação específica: Rastreamento de Posição Passiva em Sistemas MCWPT Dinâmicos. Finalmente, discute a importância de conhecer a distribuição de corrente e os parâmetros de otimização de impedância para um sistema MCWPT. Os resultados mostram que o método proposto é válido para modelar indutores impressos. Além disso, o modelo se mostrou computacionalmente mais eficiente para análise de grandes sistemas quando comparado a softwares comerciais de simulação de onda completa, e os resultados práticos apontam para a conformidade.

**Palavras-chave:** Modelo circuitual, metamaterial magnético, MIW, acoplamento de campo próximo, transferência de energia sem fio.

# List of Figures

Figure 1.1 – The evolution of Wireless Power Transmission. . . . .	17
Figure 2.1 – Classification of the main Wireless Power Transfer techniques based on efficiency and distance range. . . . .	23
Figure 2.2 – General structure of an MCWPT system. . . . .	25
Figure 2.3 – Equivalent circuit for the two-coil MCWPT system. . . . .	26
Figure 2.4 – Equivalent circuit for the MCWPT system with a metamaterial structure composed of $m \times n$ unit cells. The dashed lines represent the interaction of the source coil with the receiver coil (red) and the unit cells (green). . . . .	27
Figure 2.5 – Equivalent circuit of an array of coils with a load connected at the end. . . . .	30
Figure 2.6 – Two port network representation of the equivalent circuit that models the MCWPT system with the metasurface. In this representation, $\Gamma_G$ , $\Gamma_{in}$ , $\Gamma_{out}$ , $\Gamma_L$ are respectively the reflection coefficients seen at the generator, at the system input, at the system output, and at the load. In addition, $Z_{in}$ is the input impedance, and $Z_{out}$ is the output impedance. . . . .	33
Figure 2.7 – Three types of LC circuit configurations for impedance matching networks: (a) L-type, (b) T-type, and (c) $\pi$ -type. . . . .	35
Figure 2.8 – Four types of NIC for non-Foster matching networks: (a) Negative impedance circuit, (b) Negative resistance circuit, (c) Negative capacitance circuit, and (d) Negative inductance circuit. . . . .	36
Figure 3.1 – Specification of the square printed coil geometry used in this work: (a) top layer, (b) bottom layer. . . . .	38
Figure 3.2 – Two simple square printed coils representing two closed circuits $\Gamma_1$ and $\Gamma_2$ with current elements $I_1 d\vec{r}_i$ and $I_2 d\vec{r}_j$ , respectively. . . . .	40
Figure 3.3 – Integration model for the case of two side-by-side coplanar coils, the contribution of segment 3 of the first coil ( $y_{1,3}$ ) with segment 1 of the second coil ( $y_{2,1}$ ). . . . .	41
Figure 3.4 – Integration model for the case of two non-coplanar coils, the contribution of segment 1 of the first coil ( $y_{1,1}$ ) with segment 1 of the second coil ( $y_{2,1}$ ). . . . .	41
Figure 3.5 – Surface current distribution in the printed inductor: (a) front view, (b) back view. . . . .	44
Figure 3.6 – The variations of $M$ as a function of the cell’s relative position $(x_i, y_j)$ on a 2D metamaterial, $10 \times 10$ cells. It is taking as reference the cell $i = j = 1$ . . . . .	46
Figure 3.7 – The computational cost for the calculation of the mutual inductance matrix of the metasurface. . . . .	46

Figure 3.8 – $ S_{21} $ results from the proposed circuit model as well as full-wave simulations in CST <sup>®</sup> and measurements for different positioning in a two-coil WIPT system without resonant metasurface. . . . .	48
Figure 3.9 – MCWPT system with a resonant surface: (a) experimental setup applied to wireless power coupling studies; (b) simulated, calculated, and measured $S_{21}$ results. . . . .	49
Figure 3.10–Considerations: (a) capacitor series model, and (b) metasurface cell model used. . . . .	49
Figure 4.1 – Transmission coefficient values $S_{21}$ for the two-coil systems described in Table 4.1: curves obtained by the proposed model and by simulation in the CST and the difference found in each case. . . . .	53
Figure 4.2 – Mutual inductance $M_{sr}$ decay in a two-coil MCWPT system as the distance between the transmitting coil (Tx) and the receiving coil (Rx) increases. . . . .	55
Figure 4.3 – Specification of the square printed coil geometry used in this work: (a) top layer, (b) bottom layer in case of Tx or Rx coils, and (c) bottom layer in case of metamaterial cells. The coils dimensions are: $d_{out} = 32.5 \text{ mm}$ , and $d_{in} = 10.08 \text{ mm}$ . . . . .	56
Figure 4.4 – Prototypes of the coils Rx and Tx designed for the MCWPT system. . . . .	56
Figure 4.5 – Prototypes of the metasurface designed for the MCWPT system. . . . .	56
Figure 4.6 – Simulated and measurement $S_{21}$ results considering the Inferior Limit (IL) and Upper Limit (UL) of capacitor with tolerance of 5%. . . . .	57
Figure 4.7 – Simulated, calculated, and measured $S_{21}$ results considering a capacitance 4% bigger than its nominal value. . . . .	58
Figure 4.8 – Diagram for the experimental setup used in the transmission coefficient measurements. . . . .	59
Figure 4.9 – $PTE$ of the MCWPT system under analysis. The source coil is on the first cell of the resonant surface 10 x 10 cells while the position of the receiver varies over the other pads: (a) distribution of the maximum $PTE$ in respect to the receiver position, (b) frequency where the maximum $PTE$ occurs. . . . .	60
Figure 4.10–Displacement of the receiver on the surface: (a) Tx current amplitude variation, and (b) the receiver position on the surface. . . . .	62
Figure 4.11–Magnitude of the impedance seen by the source considering the receiver displacement over a metasurface with 10 x 10 cells at $f = 13.56 \text{ MHz}$ ). . . . .	63
Figure 4.12–Phase of the impedance seen by the source considering the receiver displacement over a metasurface with 10 x 10 cells at $f = 13.56 \text{ MHz}$ ). . . . .	63
Figure 4.13–Schematic of a dynamic MCWPT system. The detector block works as a signal transmitter, and it performs the impedance reading algorithm and the detection of the position of the device. . . . .	64

Figure 4.14–Input impedance $Z_{in}$ (magnitude and phase) seen by the detector block (Figure 4.13) as a function of the position of the receiver, considering different values for the receiver impedance $Z_L$ . . . . .	65
Figure 4.15–The resonant surface solutions ( $10 \times 10$ cells, $f = 13.56$ MHz) colors represent the cell the current modulus obtained with the complete circuit the model proposed. . . . .	66
Figure 4.16–Current density obtained by simulation using $CST^{\text{®}}$ for the $10 \times 10$ cells MCWPT system operating at $f = 13.56$ MHz . The colors represent the density of the current obtained with the simulation. . . . .	66
Figure 4.17–The resonant surface solutions ( $10 \times 10$ cells) colors represent the cell the current modulus obtained with the complete circuit the model proposed: (a) operating in $f = 13$ MHz, and (b) operating in $f = 14$ MHz. . . . .	67
Figure 4.18–Equivalent circuit for the two-coil MCWPT system structure with IOC. . . .	68
Figure 4.19–Circuit for the two-coil MCWPT system structure with IOC simulated in $ADS^{\text{®}}$ . . . . .	69
Figure 4.20– $S_{21}$ curves for the circuit shown in Figure 4.19 when simulated using the proposed model in $Matlab^{\text{®}}$ and $ADS^{\text{®}}$ . . . . .	70
Figure 4.21–MCWPT system scheme considers the circuit of the Tx element, the circuit of the receiver part, and the circuit model of each cell of the resonant surface. . . . .	71

# List of Tables

Table 3.1 – Characteristic of the printed inductor shown in Figure 3.1 used in the study . . .	38
Table 3.2 – Values obtained characteristic of the printed inductor used in the study . . . . .	43
Table 3.3 – Values obtained to calculate the mutual inductance between two side-by-side coplanar coils using Gaussian quadrature and approximation . . . . .	44
Table 3.4 – Values of the mutual inductance between two printed coils for the experimental case and the case calculated by the proposed model . . . . .	45
Table 4.1 – Characteristic electrical parameters of a printed coil as a function of the number of turns, and there is an optimization of other constructive parameters, such as line width and distance between lines, in addition to external and internal dimensions. . . . .	52
Table 4.2 – Power Transmission Efficiency (PTE) and maximum achievable efficiency ( $\eta_{MCWPT}^{max}$ ) values for two-coil MCWPT systems with different configurations. . . . .	54

# List of Acronyms

CM	Circuit Model
DBS	Deep Brain Stimulators
DWPT	Dynamics Wireless Power Transfer
CEFET-MG	Centro Federal de Educação Tecnológica de Minas Gerais
EV	Electric Vehicles
FEM	Finite Element Method
FF	Far-Field
FR4	Flame Resistant 4
IC	Integrated Circuit
IETR	Institut d'Electonique et des Technologies du numéRique
IOC	Impedance Optimizer Circuit
IoT	Internet of Things
IPT	Inductive Coupling Technique
ISM	Industrial, Scientific, and Medical
IWPT	Inductive Wireless Power Transfer
MCWPT	Magnetic Coupled Wireless Power Transfer
MF	Mid-Field
MIT	Massachusetts Institute of Technology
MIW	Magneto-Inductive Wave
NF	Near-Field
NFC	Near-Field Communication
NIC	Negative Impedance Converter
PCB	Printed Circuit Board
PTE	Power Transmission Efficiency
RWPT	Resonant Wireless Power Transfer
SOLT	Short-Open-Thru
UFSJ	Universidade Federal de São João del-Rei
VNA	Vector Network Analyzer
WPT	Wireless Power Transfer

# Contents

<b>1 – Introduction</b>	<b>16</b>
1.1 Historical Context	16
1.2 Motivation and Relevance	18
1.3 Objectives	19
1.4 Methodology	20
1.5 Scope	21
<b>2 – Magnetic Coupled Wireless Power Transfer</b>	<b>22</b>
2.1 Overview of Wireless Power Transfer Techniques	22
2.2 Magnetic Coupled Wireless Power Transfer System	24
2.2.1 MCWPT Circuit Model	25
2.2.2 MCWPT Efficiency	28
2.3 Magneto-Inductive Waves in the MCWPT Systems	29
2.3.1 Introduction to Magneto-Inductive Waves	29
2.3.2 Magneto-Inductive Waves Propagation	31
2.3.3 Efficiency Analysis of the MCWPT System	32
2.4 Impedance Optimization of the MCWPT Systems	33
2.4.1 Passive Matching Circuit	34
2.4.2 Active Matching Circuit	35
2.5 Partial Conclusions	36
<b>3 – Circuit Modeling for Analysis of the MCWPT Systems</b>	<b>37</b>
3.1 Problem Description	37
3.2 Calculation of the Characteristic Parameters of the Coil	38
3.3 Calculation of the Mutual Inductance Between Coils	39
3.4 Validation	42
3.4.1 Measurement of the Characteristic Parameters of the Coil	43
3.4.2 Evaluation of the Mutual Inductance Between Coils	43
3.4.3 Frequency Analysis of MCWPT Systems with Resonant Metasurface	47
3.5 Partial Conclusions	50
<b>4 – Analysis of MCWPT Systems</b>	<b>51</b>
4.1 The Optimization Variables in MCWPT Printed Systems	51
4.2 Revalidation of the Proposed Circuit Model	55
4.3 Measurement Setup Description	58
4.4 Maximum Efficiency	59

4.5	Variation in Source Current and in the Source Impedance . . . . .	61
4.6	Current Distribution Analysis on the Resonant Surface . . . . .	65
4.7	Impedance Optimization Analysis . . . . .	68
4.8	Partial Conclusions . . . . .	71
<b>5</b>	<b>– Final Considerations . . . . .</b>	<b>72</b>
5.1	Conclusions . . . . .	72
5.2	Future Works and Perspectives . . . . .	73
5.3	Publications and Complementary Activities . . . . .	74
	<b>Bibliography . . . . .</b>	<b>76</b>
	 <b>Appendix . . . . .</b>	 <b>81</b>
	<b>APPENDIX A – Finding Parameter <math>S_{21}</math> . . . . .</b>	<b>82</b>
	<b>APPENDIX B – Radiation Resistance of a Loop Antenna . . . . .</b>	<b>83</b>
	<b>APPENDIX C – Measurement Setup of the Characteristic Parameters of Coil . . . . .</b>	<b>84</b>
	<b>APPENDIX D – Measurement Setup of the Mutual Inductance . . . . .</b>	<b>85</b>
	<b>APPENDIX E – Measurement Setup of the S-Parameter of the System . . . . .</b>	<b>86</b>
	<b>APPENDIX F – ADS Simulation . . . . .</b>	<b>87</b>



# 1 Introduction

The recent scientific and technological advances have consolidated the presence of wireless technologies in daily life. From consumer electronics such as smartphones, tablets, laptops, and household appliances to robots and sensors in industrial applications and biomedical devices, wireless technology has increased the potential applications, creating a network of interconnected devices and allowing real-time control and data processing. Thus, technological paradigms such as the Internet of Things (IoT) and Industry 4.0 have emerged from these latest advances, and they are now shaping how society understands and interacts with electronic devices. However, the autonomy of these devices is limited by their dependence on batteries, which are one of the most expensive, bulky, and environmentally potentially harmful components in electronics. Moreover, even though a significant evolution in energy storage systems has occurred in recent years, the lifetime of these components is still short, and they require frequent replacement and maintenance. In this context, efficient Wireless Power Transfer systems capable of powering loads or charging energy storage elements have been investigated, thus rendering this research field highly promising.

## 1.1 Historical Context

The concept of Wireless Power Transfer (WPT) has a long history, dating back to the late 19th century, as shown in the timeline in Figure 1.1. Even though Nikola Tesla proposed the concept of wireless energy transfer in the late 1800s (TESLA, 2021), it was in the early 1900s that Marconi demonstrated the wireless transmission of electrical energy with the first successful long-distance wireless telegraph and, in 1901, broadcasted the first transatlantic radio signal (PATIL; PATIL, 2021). However, after that, most of the research and development focused on transmitting data and information. It was only after the 1960s that wireless power transfer became an essential concept for sustainable energy, with the development, for example, antennas connected to rectifier circuits (rectennas) for harvesting the electromagnetic energy dispersed in the environment (BROWN, 1980). After a sharply increasing interest from the scientific community and the fast development of electronic devices, WPT technology has been currently commercialized for consumer electronics, such as wireless charging for smartphones and other devices.

The first commercial wireless power transfer devices were introduced in 1990 by Delco Electronics® (a company of the General Motors - GM® group), creator of the now obsolete Magne-Charge™ system. This system was primarily developed and used for the inductive charging of vehicles (LESKARAC et al., 2015). A few years later, researchers from the Massachusetts Institute of Technology (MIT) proposed and demonstrated for the first time the concept of WPT based on magnetic resonance (KURS et al., 2007), from which spin-off companies emerged like

WiTricity<sup>®</sup> and eCoupled<sup>™</sup> that developed and commercialized this technology. Consequently, WPT was soon integrated into consumer electronics and became a popular feature in smartphones and laptops. The convenience of wireless solutions for charging battery-powered portable devices has led to the continued growth of the wireless power transfer market (YASIR; HAQUE, 2013).

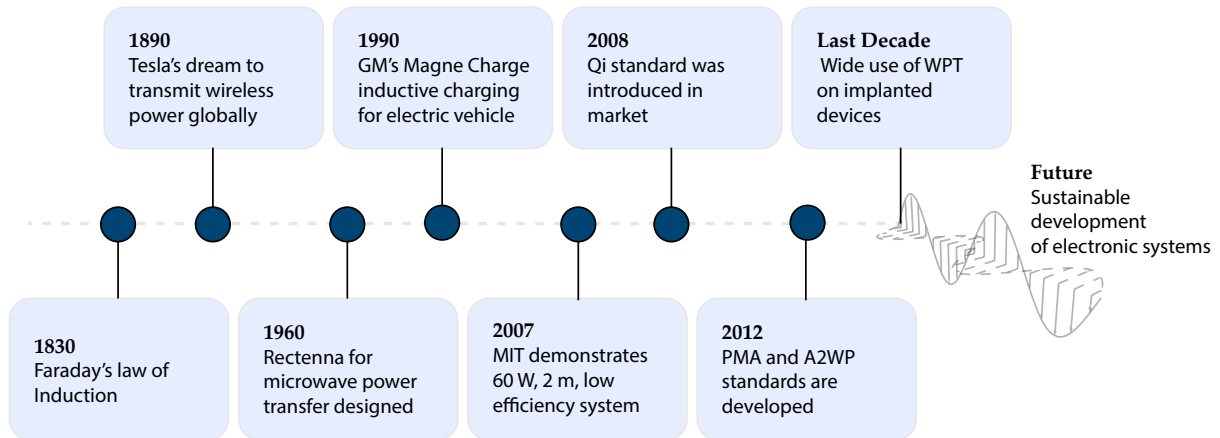


Figure 1.1 – The evolution of Wireless Power Transmission.

As shown in Figure 1.1, other WPT technologies and standards emerged from the MIT demonstrations, including Qi, Power Matters Alliance (PMA<sup>™</sup>), and Alliance for Wireless Power (A4WP<sup>™</sup>) (RAO<sup>1</sup>; GEETHA, 2016). For example, Qi technology is based on international standards widely used in smartphones, smartwatches, and other small electronic devices. With Qi wireless charging, users can place their devices on a charging pad, eliminating the need for cords and making it easier to charge multiple devices simultaneously. On the other hand, PMA<sup>™</sup> and A4WP<sup>™</sup> are two organizations that developed WPT standards. PMA<sup>™</sup> was established in 2012 and focused on developing magnetic induction-based wireless charging technology for consumer electronic devices. A4WP<sup>™</sup> was established in 2012 as well and concentrated on developing resonance-based wireless charging technology that can charge multiple devices simultaneously with greater freedom of placement. In 2015, A4WP<sup>™</sup> and PMA<sup>™</sup> merged to form the AirFuel Alliance<sup>™</sup>.

Over the last decade, WPT has been widely researched and developed for implantable medical devices. In this context, WPT enables powering medical devices without needing batteries or external power sources, increasing their reliability and reducing the risk of infection or other complications associated with battery replacement. One of the most notable applications of WPT in implantable medical devices is in pacemakers, in which WPT is used to recharge the battery or even operate without a battery entirely (LIN et al., 2020). Another application is in cochlear implants, in which wireless systems are used to deliver power to the implant and simultaneously collect data from the implant (KHAN et al., 2020). In addition, in recent years, advances in WPT technology have enabled the development of new implantable devices, such as ultra-miniature Deep Brain Stimulators (DBS) systems and retinal implants (KHAN et al., 2020), which were not possible before due to the limitations of battery-powered devices.

The growing concern about environmental issues, the advent of new generations of communication systems, and, consequently, the evolution of electronics establish a particular role for WPT technologies, which should be increasingly efficient. The current trend is using devices combining different WPT and energy harvesting technologies to take maximum advantage of the transmitted power and the energy available in the environment. Currently, most charging devices using WPT are based on Magneto-Inductive Waves (MIWs). Despite these advances, some challenges are still faced while implementing WPT in devices, such as achieving high efficiency and operational reliability as well as limiting users' electromagnetic exposure under safe levels. For this reason, researchers are continuously improving WPT technology to address these challenges and make it a more practical solution for a broader range of devices.

## 1.2 Motivation and Relevance

Magneto-Inductive Waves are electromagnetic waves that propagate along metallic and dielectric conductors. MIW is becoming increasingly popular in Wireless Power Transfer and communication systems because it allows the transfer of power or data without needing physical contact or cables. The motivation for studying wireless energy transfer systems based on magneto-inductive waves or magnetically coupled systems is to develop efficient, safe, and practical ways to transmit energy or data wirelessly over short and mid-range distances. Due to the potentialities of this technology, applications can be found in many fields, such as charging electric vehicles and medical devices, tracking and powering electronic devices, battery-free Near-Field Communication (NFC) systems commonly used in contactless payment systems, and simultaneously transferring power and data between mobile devices. Ultimately, using magneto-inductive waves is particularly attractive because of their ability to achieve high-efficient power and data transmission through non-conducting media, isolating the receiver from the power source, thus reducing the risk of electric shock. This technology allows these devices to be charged simply by placing them on a charging pad, eliminating the need for a physical charging cable.

One of the most promising applications of MIW-based WPT systems is the wireless charging of Electric Vehicles (EVs). In this context, a transmitter coil generates MIWs, which are then received by a receiver coil in the EV to charge its battery wirelessly, as proposed in (TRIVIÑO; GONZÁLEZ-GONZÁLEZ; AGUADO, 2021). MIW solutions are particularly envisaged due to their advantages in charging systems, including their constructive simplicity and reduced users' electromagnetic exposure compared to other wireless charging methods. In addition, MIW systems can also be used to locate devices in Dynamics Wireless Power Transfer (DWPT), as shown in (RAKLUEA et al., 2022). However, the technology is still in development and faces challenges in terms of efficiency and cost.

In medical devices, MIW is also applied to wirelessly charge implantable medical devices such as pacemakers and neurostimulators by creating a magnetic field near the device, inducing

an electrical current in the implanted receiver, thus eliminating the need for a direct electrical connection to the device; this type of technology is called Magnetic Coupled Wireless Power Transfer (MCWPT). Therefore, wirelessly powered implants are less invasive and reduce the risk of infection or other complications associated with surgery to replace (LIN et al., 2020) batteries. Another possibility is using WPT technology using MIW to develop battery-free biosensors, as shown in (LIN et al., 2020). Additionally, MIW can be used to locate implanted or ingested biosensors, as discussed in (UMAY; FIDAN; BARSHAN, 2017).

Magnetic Coupled Wireless Power Transfer systems consist of wires or microstrip coils connected to signal generators, power amplifiers, impedance-matching networks, and rectifier circuits. In addition, some systems have resonant surfaces that help to increase the inductive coupling between the source and receiver. Although these MCWPT systems, with or without metamaterials, are generally simple from a constructive point of view, their design can be challenging. Each of the different stages imposes its complexities, which can be computationally costly, as is the case of the electromagnetic analysis of the coils and metasurfaces, once they also have lumped elements in addition to having structural details, which increases the model complexity.

In this context, the present work proposes an alternative approach for analyzing and designing printed MCWPT systems and metasurfaces for this application, applying numerical methods and approximations to reduce computational complexity and processing time. The proposed model is based on Circuit Models (CMs), enabling faster optimization with a lower computational cost. In addition, this model makes it possible to perform an efficiency analysis of the WPT system operating in a few MHz (frequency range from 1 to 30 MHz) and its behavior in the frequency domain. Therefore, it can be used as a rapid tool for designing the electronic systems that will be incorporated.

### 1.3 Objectives

This work initially arose from a numerical circuit design of MCWPT devices. Thus, as a starting point, this work aims to theoretically, computationally, and experimentally explore the characteristics of MCWPT systems of small dimensions, built-on microstrip structures, loosely coupled, and operating in a few MHz (1 to 30 MHz). In addition, efficiency analysis is carried out, giving insights into different ways to enhance the performance of these devices. Finally, with comparative analyses with simulated and measured results, further improvements and perspectives on future work are discussed.

The specific secondary objectives are:

- A literature review focused on MCWPT systems is performed. This review makes it possible to characterize and understand all the factors that affect the efficiency of this technique, as well as the improvement methods proposed in the literature;

- A CM that accounts for the dynamics of electromagnetic phenomena must be proposed. The microstrip inductive structures in which lumped elements are added are analyzed. All aspects related to the computational implementation of the proposed model are described and evaluated through validations carried out by simulations and measurements. In addition, an analysis of the accuracy range of the models is carried out based on the results obtained from commercial software and experimental measurements;
- Explorations are carried out to study the frequency behavior of transmission efficiency, input impedance variation, and current distribution in the metamaterial. All analyses are performed using a CM for analyzing tridimensional structures. Then, the optimization variables of an MCWPT system as well as ways to improve the efficiency and limitations of the system, are explored.

## 1.4 Methodology

In the present work, a bibliographic review is initially carried out regarding magnetically coupled wireless power transfer systems manufactured with microstrip technology, including applications in which metamaterial slabs enhance performance. In addition, a literature review focused on the methods used in modeling these magnetic coupled WPT systems is presented. In addition, a brief theoretical analysis of the performance parameters is performed, giving insight into the factors that can maximize the efficiency and strategies to minimize impedance mismatching on MCWPT systems.

After that, a circuit modeling is proposed based on the first principles for calculating the self-inductance and the radiation resistance of printed inductors as well as the mutual coupling between coils. This modeling describes the electromagnetic behavior of MCWPT systems and allows us to analyze performance parameters such as efficiency, the quality factor ( $Q$ ), and impedance. First, using the Matlab<sup>®</sup> programming environment, the coils were characterized using approximations and closed-form methods for calculating parameters such as self-inductance and radiation resistance. Subsequently, the Neumann method is carried out to calculate the mutual inductance between the coils.

Once the models were created, the experimental validation strategy was described step-by-step using a prototyped MCWPT system. The equipment and instruments from the Laboratory Ampère at the École Centrale de Lyon were used for the experimental setup: the impedance meter, network analyzer, and spectrum analyzer. Furthermore, the simulations in commercial software were used for both electromagnetic analysis and SPICE simulations. For this, the facilities of the Institut d'Electronique et des Technologies du numéRique (IETR) were also used.

## 1.5 Scope

This dissertation is organized as follows. This chapter contains a historical contextualization of WPT systems, the motivation and objectives for this work, and the methodology used. Some reference works in this field are also presented.

In Chapter 2, a bibliographic and theoretical review is carried out. First, a brief introduction to the concept of wireless power transfer found in the literature is presented. Then, it defines wireless energy transfer systems with magnetic coupling and the main conceptual aspects of this technology. Then the efficiency and the factors that affect it are analyzed using as a reference the two-coil system. Next, the properties and advantages of resonant surfaces in energy transmission are discussed. Then, in light of the magneto-inductive waves theory, the efficiency enhancement with the strengthening of the magnetic coupling in the presence of the metasurface is discussed, as well as the viability of its use in systems where the transmitter and receiver are misaligned. Finally, it presents different possibilities for optimizing the impedance of WPT systems, thus increasing transmission efficiency.

Subsequently, in Chapter 3, the electromagnetic problem concerning MCWPT systems is described and formulated by applying approximate and quasi-static methods in a CM proposed. First, the characteristic parameters, such as resistance and self-inductance of a printed inductor, are calculated using approximation methods. Next, the one-dimensional numerical formulation analogous to the thin-wire approximation is used to calculate the mutual inductance. Finally, the experimental validation of the proposed models takes place; the results found in simulations and experiments for the system under study are presented, as well as a comparison between the numerical simplification used to calculate the mutual inductance integral with a traditional numerical method for integration.

Chapter 4 is devoted to exploring the optimization variables of a microstrip-printed MCWPT system. For this, a new system based on printed and square topology coils, now miniaturized, is designed at 13.56 MHz (Industrial, Scientific, and Medical band). This system is used to analyze how the frequency and receiver position over the metasurface affects the energy transmission efficiency of the system. The chapter also analyzes the source impedance variation and the current flow on the metamaterial surface regarding the receiver position and the load variation on the resonant surface. The MIW theory is used and explored for a specific application: Passive Position Tracking in Dynamic MCWPT Systems.

Finally, in Chapter 5, the results discussed in the dissertation are summarized, future work and perspectives for improvement are discussed, and the scientific publications produced during this project are presented.

## 2 Magnetic Coupled Wireless Power Transfer

In this chapter, the concept of wireless power transfer is briefly introduced. Then, it presents a definition of Magnetic Coupled Wireless Power Transfer systems and the physical principle underlying this technology. Then, the efficiency and its defining parameters are analyzed using a two-coil system. Afterward, the effect of resonant surfaces in wireless energy transmission and the advantages of their use are discussed. Next, the magnetic coupling enhancement in the presence of metasurfaces and the consequent efficiency increase is discussed based on the magneto-inductive wave theory. In addition, the feasibility of using metasurfaces in WPT systems in systems where the transmitter and receiver are misaligned is analyzed. Finally, possibilities for optimizing the impedance of WPT systems are presented to increase transmission efficiency.

### 2.1 Overview of Wireless Power Transfer Techniques

WPT technology can be implemented with several methods. However, the main approaches for transmitting energy wirelessly through electromagnetic waves are the Far-Field (FF) or radiative technique and the Near-Field (NF) or non-radiative approach. The strategies used in the FF group use microwaves, lasers, or solar energy. On the other hand, the second method employs NF coupling, which can be capacitive or inductive.

The WPT technique based on radiative electromagnetic waves has the main advantage of achieving energy transmission over greater distances than NF coupling techniques, as shown in Figure 2.1. This factor is mainly because, in the FF, the transmission distance is much greater than the physical length of the transmitter. Therefore, devices that allow wave focusing and beamforming, such as metamaterials or antenna arrays, are generally used to achieve higher efficiency. However, the maximum power transfer achievable by this technique is lower due to wave attenuation, with its usage often limited to charging low-power devices.

Methods based on NF coupling, either capacitive or inductive, are applied when the transmission distance range is much smaller than the wavelength; *i.e.*, the transmitter and receiver are relatively close. In this case, the impedance seen by the source is significantly affected by the impedance of the receiver. Therefore, the major limitation of this technique is that the transmission efficiency decreases dramatically as the separation between transmitter and receiver or in case of misalignments between them. Therefore, its applications are limited to a transmission range of a few centimeters. However, near-field methods are widely used commercially because of their higher efficiency and power transfer levels while being constructively simple and having low-cost physical implementation.

In some applications, as discussed in (CHEN et al., 2018) and (DAS; YOO, 2017), the

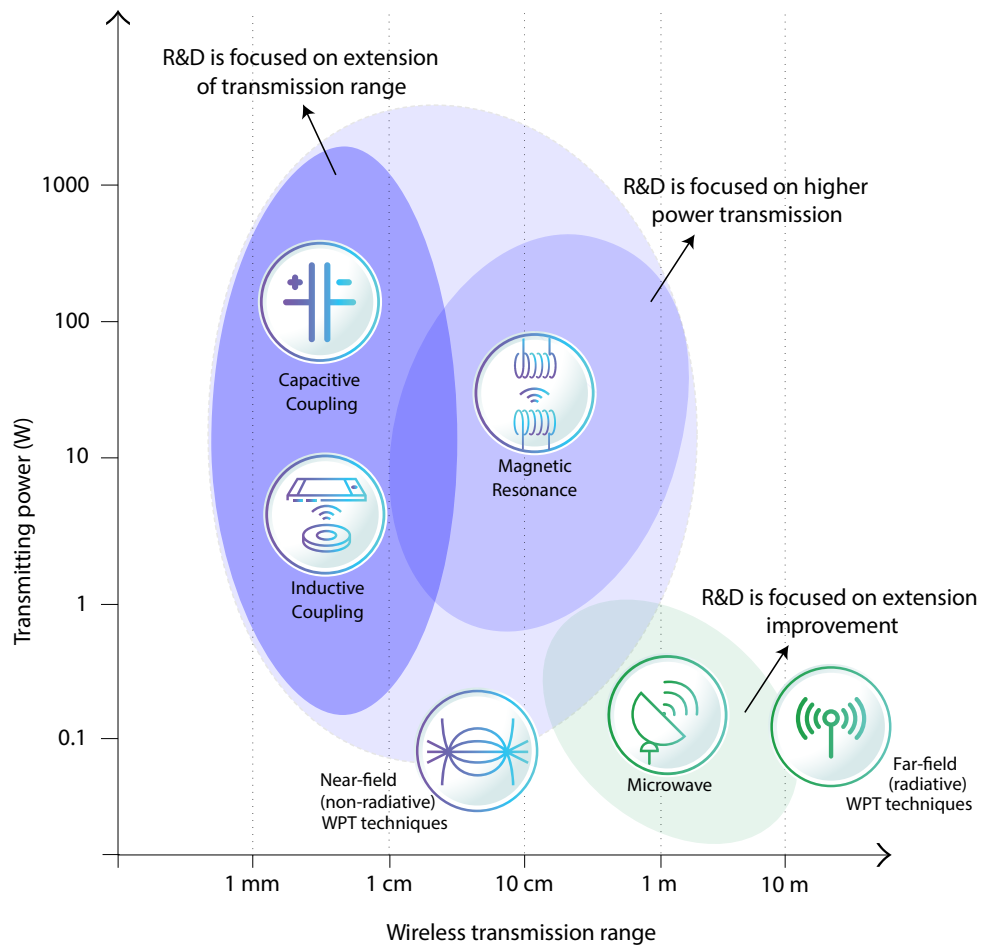


Figure 2.1 – Classification of the main Wireless Power Transfer techniques based on efficiency and distance range.

WPT technique used is called MidField (MF). This designation is commonly used for WPT applications on implanted biomedical devices. This approach combines the advantages of near- and FF techniques, leading to greater efficiency in lossy media, especially when the receiver is much smaller than the source (HO; KIM; POON, 2013).

In the context of Inductive Wireless Power Transfer (IWPT) systems, there are several publications in the literature in which metamaterials are used between the transmitter and receiver to enhance the wireless power link and to increase transmission efficiency (SHAN et al., 2022) or also to focus the magnetic field (SOARES; RESENDE, 2022). These artificial materials are able to restore the near-field evanescent waves and consequently collimate magneto-inductive waves, surpassing the optical diffraction limits. It is possible since these materials present negative effective magnetic permeability (ALMEIDA; FEITOZA, 2018) or negative effective permittivity (PELEKANIDIS et al., 2017), or in some cases, even both electromagnetic parameters are negative (PENDRY, 2000).

In addition, other WPT approaches use mechanical waves, such as devices that use the ultrasonic (MENG; KIANI, 2017) or the piezoelectric effect (CALIÒ et al., 2014). However, this type of technology still has low efficiency, and as they use mechanical waves, they are often conditioned to specific environments.



The choice of the ideal WPT technique as well as its maximum achievable efficiency, depends on the nature of the application, the distance between the transmitter and the receiver, the operating frequency, and the environment in which the system is operating, among other system-level factors such as size, materials, and electronic circuitry. For example, the literature review in (BASIR; YOO, 2020) compares different WPT techniques for charging biomedical implantable devices, considering their operating and construction conditions and presenting the efficiency in each case.

This work is focused on one of the most recurrent WPT methods: magnetic induction, which still does not have advanced studies in modeling and design in certain applications, such as misaligned systems. As mentioned earlier, this method belongs to the group of near-field techniques. Unlike the capacitive method, which uses the electric field between two plates, one transmitting and the other receiving, the magnetic induction method uses the power stored on the magnetic field between two coupled coils. Compared to the capacitive approach, the advantage of magnetic technology is that energy transmission is more focused from the transmitter to the receiver, leading to greater efficiency when the receiver and the transmitter are farther apart, as presented in (DAI; LUDOIS, 2015).

In the literature, some authors separate the magnetic coupling method of energy transmission into two approaches: the purely inductive method employed in Inductive Wireless Power Transfer (IWPT) and the resonant magnetic method or Resonant Wireless Power Transfer (RWPT). The first method is restricted to applications where the transmitter and receiver devices are close and strongly coupled. On the other hand, when there is a larger distance range between transmitter and receiver can be achieved using coils resonant at the same frequency, that is, using the second method. However, this approach is more susceptible to a sharp reduction in the efficiency when the coils are too close, a phenomenon called the frequency splitting effect.

This work presents a general study and mathematical modeling of MCWPT systems, focusing on resonant systems where the receiver and transmitter are misaligned or coplanar on a metasurface. In addition, studies focused on applications of this type are not as advanced as others. The following sections present the definitions and main characteristics of these magnetic systems, as well as the analysis of the main performance parameters.

## 2.2 Magnetic Coupled Wireless Power Transfer System

Magnetic Coupled Wireless Power Transfer Systems have many different implementations, depending on the application and the resources available for its realization. However, all of them follow the general structure presented in Figure 2.2 in which the main components of an MCWPT system are shown in a block diagram. In this representation, a simple model with two coupled coils is considered, on one side a transmitter (Tx) and the other the receiver (Rx), both magnetically coupled. Additionally, each coupler has a capacitive reactance tuned at the resonant frequency, defined as the system's operating frequency. Furthermore, both Tx and Rx

coils can have an impedance-matching subsystem. Finally, what differentiates transmitting and receiving parts is that there is a source of RF power connected to Tx, and in the Rx, there is a load to be fed.

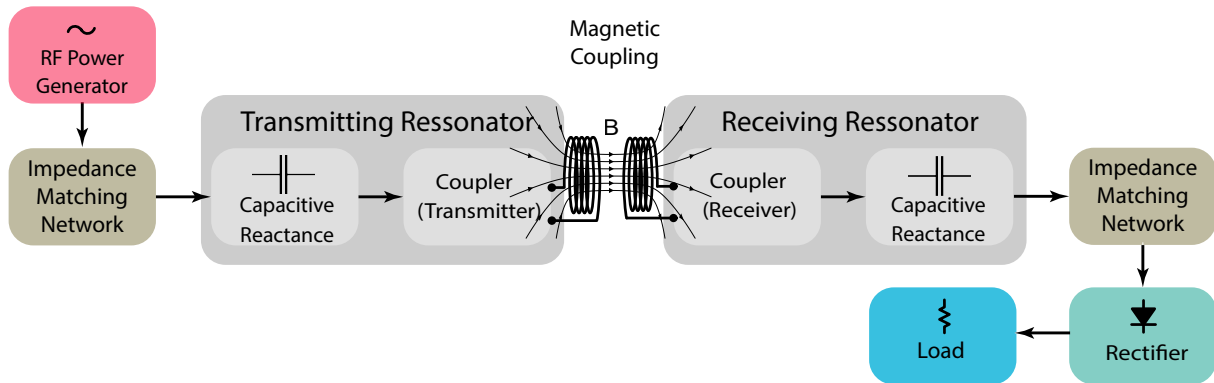


Figure 2.2 – General structure of an MCWPT system.

More complex types of MCWPT can be found in the literature. For instance, multi-transmitter systems, as the name suggests, comprise different transmitters and a single receiver to focus the power of all transmitters on one receiver (DANG et al., 2020). This type of system is robust to misalignments and other variations in the operating conditions, making it possible to power the load dynamically and adaptively. Conversely, some implementations use multiple receivers. In this case, a single transmitter can power several receivers, which is ideal for applications where multiple low-consumption loads must be powered (LEE; KIM; JANG, 2021). Finally, systems with intermediate coils between Tx and Rx have been proposed to increase efficiency (TIAN et al., 2021).

The overall structure depicted in Figure 2.2 can be manufactured through multiple implementations: wire or printed coils with different geometries can be used, among other possibilities, such as using special materials that increase magnetic coupling, such as ferromagnetic slabs. Analogously, there are many topologies of resonance circuits, which can be of two types: serial resonant powered by voltage or parallel resonant powered by the current (SU et al., 2006). The matching circuits can also vary according to the application, nature of the load, or even the size of the loops, and can be purely passive or use active circuits of so-called non-Foster circuits, always employed to increase the WPT efficiency (KIM et al., 2019). The following sub-sections present the main concepts used to analyze MCWPT systems used in this work, such as the circuit model, with which it is possible to calculate the current in the loops, for example.

### 2.2.1 MCWPT Circuit Model

Circuit modeling approaches simplify the analysis of essential phenomena in engineering applications, giving us a better insight into the physics behind those phenomena. For instance, a printed inductor can be represented by a series association of an inductor  $L$ , a resistor  $R$  that models the losses in the coil, and a capacitor  $C$  that takes into account the capacitance

between the coil's turns and any lumped capacitance added to it. Therefore, two-coil MCWPT systems can be modeled by the equivalent circuit shown in Figure 2.3, in which the transmitter side is represented by a source impedance  $Z_s$ , a characteristic resistance of the coil  $r_s$ , and the self-inductance  $L_s$ . Analogously, on the side of the receiver, it has the resistance of the coil  $r_r$ , the self-inductance  $L_r$ , and the load impedance  $Z_L$ . Finally,  $C$  is the lumped capacitance added for tuning the resonance. If MCWPT works in low frequencies, the parasitic capacitance between the loops can be disregarded.

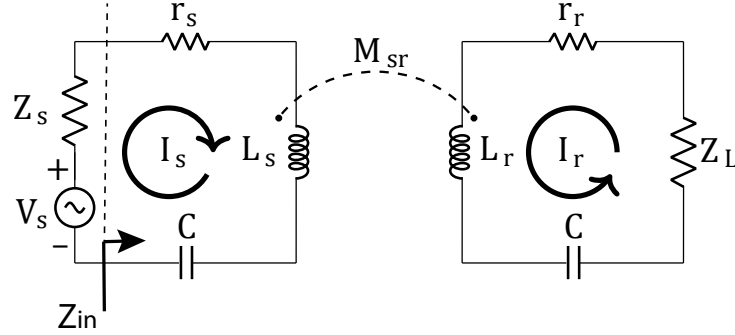


Figure 2.3 – Equivalent circuit for the two-coil MCWPT system.

The magnetic coupling interaction between Tx and Rx is represented by the mutual impedance, defined by the ratio of the voltage in the Rx induced by the temporal variation of the current that flows in the Tx (BALANIS, 2012). Mutual coupling is a significant effect investigated in antenna or metamaterial arrays analysis. In MCWPT systems such as shown in Figure 2.3, the main interest is in magnetic coupling since the parasitic capacitance between coils can be disregarded at the operating frequency range of MCWPT systems. Consequently, the circuit parameter that models the coupling between Tx and Rx is the mutual inductance  $M_{sr}$ .

Once the CM is formulated, it can be mathematically described by the linear system represented in (2.1), in which the matrix of independent elements comprises the excitation voltages, that is, the source voltage  $V_s$  and the receiver voltage  $V_r = 0$  since there is not a voltage source connected to it. In addition, the matrix of coefficients is composed of the impedance elements in each loop: the diagonal elements of the impedance matrix represent the self-impedance of each coil, whereas the off-diagonal elements represent the impedance due to the mutual inductance between the loops. Finally, the matrix of unknowns contains the current that flows in each loop, and it can be evaluated by solving the linear systems.

$$\begin{bmatrix} V_s \\ 0 \end{bmatrix} = \begin{bmatrix} Z_s + r_s + j\omega L_s - \frac{j}{\omega C} & j\omega M_{sr} \\ j\omega M_{sr} & Z_L + r_r + j\omega L_r - \frac{j}{\omega C} \end{bmatrix} \cdot \begin{bmatrix} I_s \\ I_r \end{bmatrix} \quad (2.1)$$

The equivalent circuit model can also be applied to more complex structures (SANDOVAL; MOAZENZADEH; WALLRABE, 2018). However, the model becomes more complex as the number of elements in the MCWPT system increases. Despite the greater complexity, the modeling strategy is similar to that shown in Figure 2.3 once the representation of the elements

Tx and Rx does not change. Therefore, for the sake of simplicity, their equivalent impedances are called  $Z_{Tx}$  and  $Z_{Rx}$ , respectively.

The equivalent CM for an MCWPT system with a resonant metasurface is shown in Figure 2.4, which illustrates a more complex system. It comprises the coil transmitter, a metamaterial composed of a planar array of unit cells, and a coil receiver. In this case, each metamaterial cell is represented by a series RLC circuit, in which  $r$  is the characteristic resistance of the cell,  $L$  is its self-inductance, and  $C$  is the lumped capacitance for tuning its resonance. Finally, each pair of coils and unit cells is associated with a mutual inductance, modeling the interaction between all inductors that compose the system.

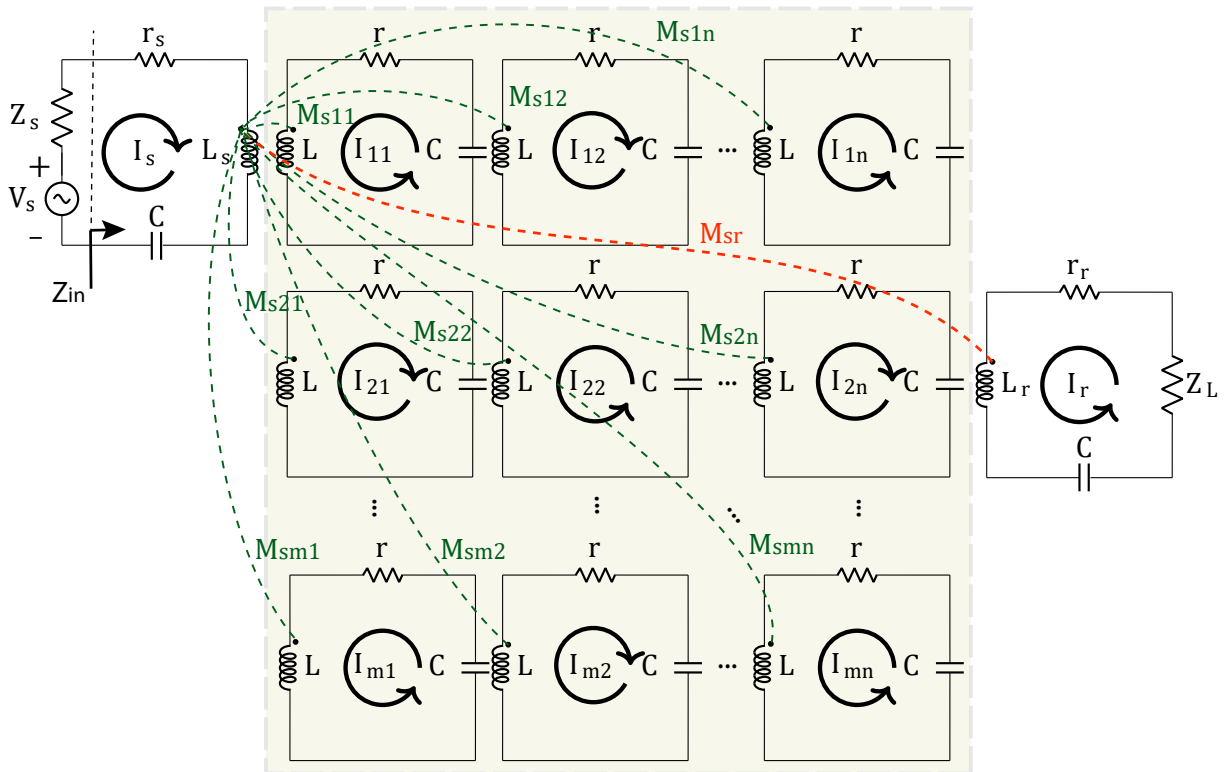


Figure 2.4 – Equivalent circuit for the MCWPT system with a metamaterial structure composed of  $m \times n$  unit cells. The dashed lines represent the interaction of the source coil with the receiver coil (red) and the unit cells (green).

The metamaterial cells in Figure 2.4 are numbered in increasing order from left to right and top to bottom, up to row  $m$  and column  $n$ , totalizing  $N = m \times n$  unit cells. Therefore, in the matrix formulation in (2.2), the diagonal of the impedance matrix represents the self-impedance of each element, whereas the off-diagonal is the impedance due to the mutual inductance between them. In this way, off-diagonal elements of the first row and column comprise the coupling between the source and the other elements. Similarly, the last row and column are constituted by the coupling of the receiver with the transmitter coil and unit cells.

$$\begin{bmatrix} V_s \\ 0 \\ \vdots \\ \vdots \\ 0 \end{bmatrix} = \begin{bmatrix} Z_{Tx} & j\omega M_{s11} & \cdots & j\omega M_{smn} & j\omega M_{sr} \\ j\omega M_{s11} & r + j\omega L - \frac{j}{\omega C} & \cdots & j\omega M_{1n} & j\omega M_{rmn} \\ \vdots & \vdots & \ddots & \vdots & \vdots \\ j\omega M_{smn} & j\omega M_{m1} & \cdots & r + j\omega L - \frac{j}{\omega C} & j\omega M_{r11} \\ j\omega M_{sr} & j\omega M_{rmn} & \cdots & j\omega M_{r11} & Z_{Rx} \end{bmatrix} \begin{bmatrix} I_s \\ \vdots \\ \vdots \\ I_{mn} \\ I_r \end{bmatrix} \quad (2.2)$$

The circuit modeling presented above in (2.2) allows for calculating the basic electrical parameters of the system. For instance, the currents in each element are found out by solving:  $\mathbf{I}_{(N+2) \times 1} = \mathbf{Z}_{(N+2) \times (N+2)}^{-1} \mathbf{V}_{(N+2) \times 1}$ . Therefore, based on the source voltage and the calculated currents, it is possible to evaluate the performance parameters of the MCWPT system, such as the power delivered to the load or efficiency. In addition, with the CM, it is possible to carry out much faster post-processing analysis compared to commercial software based on full-wave electromagnetic analysis, which has a high computational cost.

### 2.2.2 MCWPT Efficiency

Some analyzes were performed in (SOARES, 2020) for RWPT systems consisting of two and four coils. It is important to note that efficiency, in this case, was defined as the relationship between the power delivered to the load and the power supplied by the source; this relationship is given as a function of the transfer quality factor ( $T_Q$ ). For the simple case of two coils, as shown in Figure 2.3. Efficiency is defined as:

$$\eta_{MCWPT} = \frac{T_Q^2}{1 + \frac{R_L}{r_r} + T_Q^2} \cdot \frac{\frac{R_L}{r_r}}{1 + \frac{R_L}{r_r}}, \quad (2.3)$$

where  $T_Q$  is defined by (ZHANG, 2018):

$$T_Q = \frac{\omega M_{sr}}{\sqrt{r_s \cdot r_r}}, \quad (2.4)$$

Based on this formulation, the transfer quality factor defines the maximum transmission efficiency. As seen in (ZHANG, 2018), this relationship can be written as:

$$\eta_{MCWPT}^{max} = \left( \frac{T_Q}{1 + \sqrt{1 + T_Q^2}} \right)^2. \quad (2.5)$$

Considering a system composed of two resonant coils, the maximum efficiency seen in (2.5) is directly linked to the  $T_Q$ , which is, in its turn, directly proportional to the inductive coupling between the coils given by the mutual inductance  $M_{sr}$  loops and inversely proportional to the square root of the product of the characteristic resistances of the two coils. Thus, to enhance

the transmission efficiency, it is necessary to increase the inductive coupling and reduce resistive losses in the Tx and Rx. Therefore, a technique used to increase the coupling between Tx and Rx is using resonant surfaces. This technique allows for achieving greater efficiency, especially when the Tx and Rx are misaligned. In addition, it may also be used as a positioning detection device in some applications.

## 2.3 Magneto-Inductive Waves in the MCWPT Systems

As described in Section 2.1, some MCWPT systems comprise particularly engineered materials called metamaterials. In this context, these materials are designed to support a specific type of wave propagation known as Magneto-Inductive Waves. Since devices based on MIW operate at frequencies in which the wavelength is much larger than the structure size, one advantage is that simple mathematical formulations can be used to study the wave behavior on the metasurface it is possible the modeling the system in the circuit of lumped-element. Moreover, another advantage is that, with a single transmitter, it is possible to supply power to receivers positioned in several locations across the metasurface, increasing its spatial freedom (STEVENS, 2015b). This aspect is exploited in several applications, such as receiver identification in Dynamic Wireless Power Transfer systems. Therefore, this section thoroughly describes MIW and its application to MCWPT systems.

### 2.3.1 Introduction to Magneto-Inductive Waves

The concept of magneto-inductive waves emerged from the study of metamaterials. The simplest way to represent a metamaterial is by using coupled  $RLC$  circuits that model the cells that compose this structure. In this way, the magnetic field propagates from one unit cell to another across the structure through the inductive coupling between neighbor coils. For this reason, the wave propagation supported by these metamaterials is called Magneto-Inductive Waves (SOLYMAR; SHAMONINA, 2009). This type of wave falls into the group of slow waves, which propagates at a speed slower than light. Because the size and separation of the metamaterial cells are much smaller than the wavelength, this phenomenon can be almost entirely analyzed using static and quasi-static approximations (CAMPIONE; MESA; CAPOLINO, 2013).

In MIW applications, most researchers consider unidimensional (1D) arrays of coils excited at one end by a source that feeds a single load at the other, as shown in Figure 2.5. In this configuration, with perfectly matched terminals, MIW waves are emitted by the transmitter, flow through the structure, are attenuated by the resistance of each coil, and then are completely absorbed by the load at the receiver, as considered in (SIMONAZZI; SANDROLINI; MARISCOTTI, 2022). However, there are applications where a bidimensional (2D) array of resonant coils is considered, with excitation in a specific position on the plane. Similarly, a resonant receiver arbitrarily positioned over this in this array is fed, as proposed in (SANDOVAL et al., 2019).

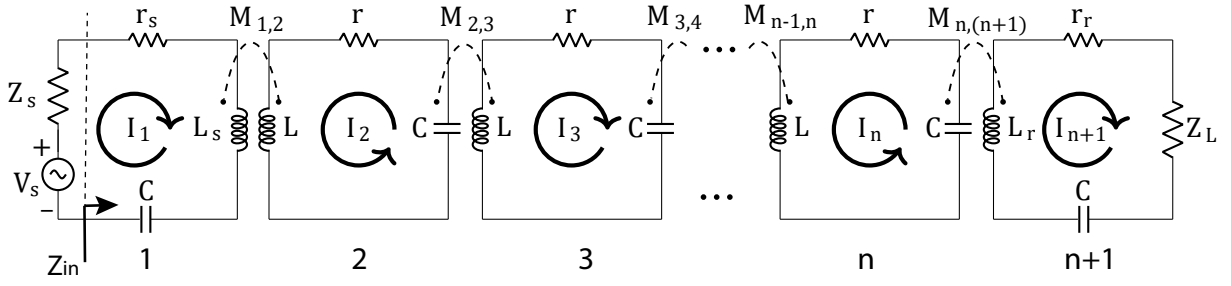


Figure 2.5 – Equivalent circuit of an array of coils with a load connected at the end.

Time-harmonic analyses in the frequency domain are essential in MCWPT systems due to the narrowband nature of this application. In the case of systems that use metamaterial structures, this analysis is even more critical due to the characteristics of these devices, which are often selective at specific frequencies (ZHOU; SHEN, 2021). Another phenomenon observed in strongly-coupled inductive systems is the so-called Frequency Splitting, which is the optimal frequency division and maximum efficiency reduction due to the over-coupling between the coils (ZHANG; ZHAO, 2014). Therefore, evaluating the frequency response of efficiency and output current is required, which becomes computationally simpler and faster using a circuit model than performing full-wave electromagnetic analysis.

In dynamic MCWPT systems, another important design feature to evaluate is the impedance reflected in the transmitter due to the presence of the receiver. In the case shown in Figure 2.5, for each pair of resonators  $i$  and  $i + 1$ , the input impedance can be defined as a continuous function of space. The expression (2.6) models the impedance seen at the source as a function of the receiver displacement across the 1D system when the system operates at the resonant frequency.

$$Z_{in} = r_s + \frac{(\omega_0 M_{1,2})^2}{r + \frac{(\omega_0 M_{2,3})^2}{r + \frac{(\omega_0 M_{3,4})^2}{\vdots \frac{(\omega_0 M_{n,(n+1)})^2}{r_r + \frac{Z_L}{Z_L}}}}}, \quad (2.6)$$

The input source impedance of the 2D system shown in Figure 2.4 can be modeled. When a receptor is above a metasurface-specific location, the total impedance reflected in the metamaterial and source is the sum of its effects on each cell and coil. This evaluation is possible using the relation:

$$Z_{incell} = \frac{\omega_0^2}{r_r + Z_L} \sum_{n=1}^{N+1} M_{r,n}^2, \quad (2.7)$$

where  $\omega_0$  is the resonant frequency of the system given by:

$$\omega_0 = 1/\sqrt{LC}, \quad (2.8)$$

and  $M_{r,n}$  is the mutual inductance between the receptor and  $n$ -cell of the metamaterial surface plus the source, and finally  $Z_L$  is the receptor impedance. On the other hand, the impedance seen by the source is defined in (2.9), where  $I_s$  is the current of the excited coil Tx as shown in Figure 2.3 and Figure 2.4.

$$Z_{in} = \frac{V_s}{I_s} - Z_s \quad (2.9)$$

Finally, using (2.7) and (2.9), it is possible to find the sum term in (2.7), the total coupling between the receptor and the cells is necessary to optimize the efficiency (ZHANG, 2018). For example, a perfect match for maximum efficiency would be the receiver impedance must also match the imaginary part of the group metamaterial plus source. However, in practice is something complex. Other optimization factors, such as the distance between the receiver and the surface, could maximize efficiency. This distance is implied by the sum operator in (2.7); however, finding it analytically is problematic because it depends on all the related mutual inductances, which becomes a computational task. It should also be mentioned that in a situation with impedance matching, that is, in the case of a system without reflection, (2.7) is equal to (2.9).

### 2.3.2 Magneto-Inductive Waves Propagation

Magneto-inductive waves are specific waveforms that propagate in certain metamaterials formed from inductively coupled resonant circuits (STEVENS, 2015a). These waves are produced by the magnetic field variation that induces an electric field, which generates another magnetic field, and so on. This behavior creates a self-sustaining cycle of oscillating magnetic and electric fields that propagate through the metamaterial. The speed at which magneto-inductive waves propagate depends on the electrical and magnetic properties of the medium and the frequency of the wave, the same as any electromagnetic wave.

The phenomenon of MIW in linear arrays, as shown in Figure 2.5, can be described as a function of the currents that flow in this arrangement, which can be written in the form:

$$I_n = I_0 e^{-(\alpha + j\beta)nd}, \quad (2.10)$$

where  $I_0$  is a constant,  $\alpha$  is the attenuation coefficient,  $\beta$  is the phase factor, and  $nd$  is the distance traveled by the wave, given in the number of steps  $n$  and the physical distance  $d$  between the cells of the array. It should be noted that the formulation (2.10) can be extended to the case 2D. For such a representation, it is enough to consider the propagation constant composed by the components in  $x$  and in  $y$ ; thus, it has  $\alpha_x$ ,  $\alpha_y$ ,  $\beta_x$ , and  $\beta_y$ .

The attenuation of the MIW as it propagates across a device operating at the resonant frequency of the cells is given by:

$$\sinh(\alpha d) = \frac{1}{D\kappa Q}, \quad (2.11)$$



where  $D$  is the dimension factor, which usually is 1 for 1D structure or 2 for 2D structure. The  $\kappa$  component is the nearest neighbor coupling given by  $2M/L$ , where  $M$  is the nearest neighbor mutual inductance, and  $L$  is the element self-inductance. Finally,  $Q = \omega L/r$  is the quality factor of the loop.

The propagation of these waves shown in Figure 2.5 can be described in terms of the phase constant by:

$$\cos(\beta d) = \frac{\omega_0^2 - \omega^2}{\kappa\omega^2}. \quad (2.12)$$

The equation (2.12) shows that MIW propagation is not confined to only one frequency. In this way, as shown in (SHAMONINA et al., 2002), the propagation range is defined by:

$$\frac{\omega_0}{\sqrt{1 + D\kappa}} \leq \omega \leq \frac{\omega_0}{\sqrt{1 - D\kappa}} \quad (2.13)$$

From the formulation (2.13), it is possible to verify that the MIW bandwidth in a two-dimensional configuration is larger than in a one-dimensional one. Furthermore, a stronger coupling between the resonators would result in a MIW with a larger frequency bandwidth, as verified in (CHAN; STEVENSY, 2011).

### 2.3.3 Efficiency Analysis of the MCWPT System

In Section 2.2.2, some approaches to obtain the efficiency of a basic MCWMPT system were presented. The presented approach can be extended to a system consisting of Tx, Rx coils, and a metasurface. For this, the two-port network theory will be used as shown in Figure 2.6, in which the entire MCWPT system, no matter in which configuration, with or without metasurfaces, can be fully characterized by its two-port scattering parameters matrix. Therefore, as deduced in (SONG; BELOV; KAPITANOVA, 2017), the energy transfer efficiency in the system can be obtained by (2.14).

$$\eta_{MCWPT} = \frac{|S_{21}|^2 (1 - |\Gamma_L|^2)}{(1 - |\Gamma_{in}|^2) |1 - S_{22}\Gamma_L|^2} \quad (2.14)$$

As also shown in (SONG; BELOV; KAPITANOVA, 2017), the formulation (2.14) can be simplified if the load impedance is matched to the reference impedance  $Z_s$ , so that  $\Gamma_L = 0$  and  $\Gamma_{in} = S_{11}$ , then the efficiency expression reduces in (2.15):

$$\eta_{MCWPT} = \frac{|S_{21}|^2}{1 - |S_{11}|^2}. \quad (2.15)$$

Transmission efficiency is one of the most important performance parameters in WPT system design. A high transmission efficiency means less power is lost in the system and more

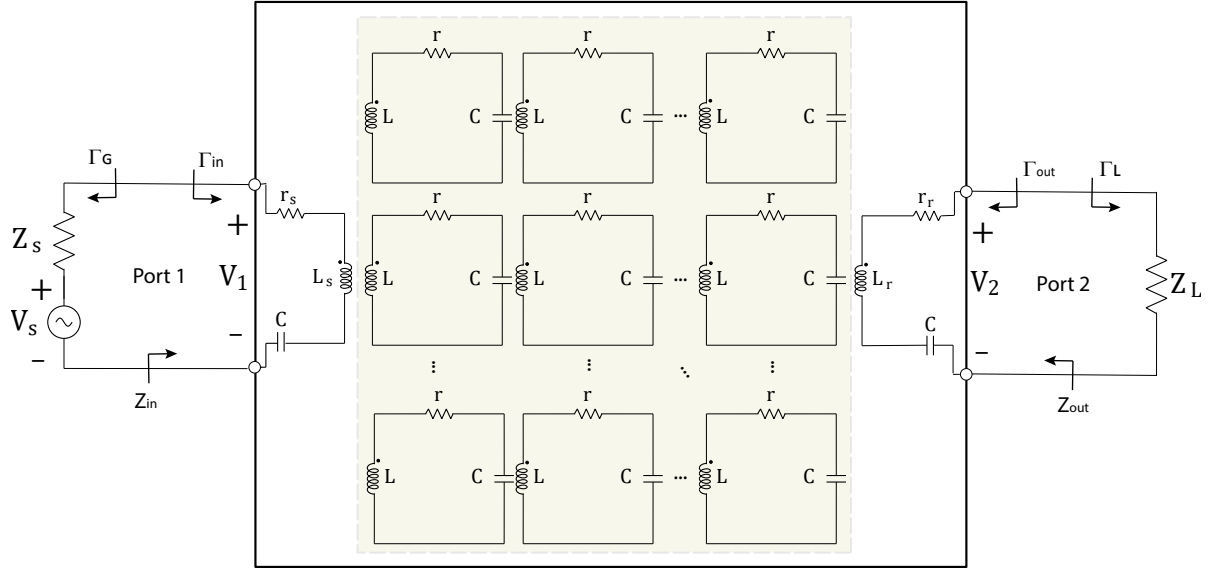


Figure 2.6 – Two port network representation of the equivalent circuit that models the MCWPT system with the metasurface. In this representation,  $\Gamma_G$ ,  $\Gamma_{in}$ ,  $\Gamma_{out}$ ,  $\Gamma_L$  are respectively the reflection coefficients seen at the generator, at the system input, at the system output, and at the load. In addition,  $Z_{in}$  is the input impedance, and  $Z_{out}$  is the output impedance.

power is delivered to the load. Therefore, the Power Transmission Efficiency (PTE) can be expressed as:

$$PTE(\%) = |S_{21}|^2 \cdot 100, \quad (2.16)$$

where  $S_{21}$  is the forward transmission coefficient given by (see the proof in Appendix A):

$$S_{21} = 2 \cdot \frac{V_L}{V_s} \sqrt{\frac{Z_s}{Z_L}}, \quad (2.17)$$

in which  $V_L$  is the voltage on the load and  $V_s$  is the supply voltage. In this way, based on the model shown in Figure 2.3 and its mathematical formulation in (2.1), it is possible to optimize the system parameters in order to achieve maximum PTE.

## 2.4 Impedance Optimization of the MCWPT Systems

One essential step in order to improve the performance of WPT systems is designing impedance optimizer circuits, also known as impedance matching circuits, since they maximize the power transfer from the source to the load. The premise of any impedance matching scheme is transforming the load impedance to the complex conjugate of the source impedance so that the maximum power can be transferred to the load. It should also be noted that impedance matching can reduce the amplitude and phase errors during electrical signal transmission (POZAR, 2011).

There are an infinite number of possibilities for designing an impedance-matching network. It could be something as simple as a two-element LC compensation or a multi-stage filter of multiple elements. In microwave applications, impedance-matching networks can consist

of wave transformers or interdigital components. Thus, some applicability factors must be considered when building impedance-matching circuits, such as complexity, operating bandwidth, implementation, and adjustability.

In the context of MCWPT, a matching network should minimize the power factor at the input, maximize the power transfer at the output, and keep the load current, voltage, and power constant. In some applications, in a system with resistive load, for example, optimizing the system to maximize efficiency is essential, which does not mean maximum power transmission since this is achieved with an efficiency of 50%. Another factor that modifies the impedance matching of coupled systems is the distance between the source and load. With the variation of the distance, there is also a variation in the coupling, that is, a change in the mutual impedance between the coils, which affects the impedance seen by the source. Therefore, the impedance matching also varies with the distance; in this way, for a dynamic system, the matching network should be adaptive in order to keep the current and voltage delivered to the load constant.

### 2.4.1 Passive Matching Circuit

Passive impedance matching circuits are used in WPT systems to optimize power transfer between the transmitter and receiver coils by ensuring that the impedance of the transmitter and receiver coils are matched. Thus, the power reflected by the transmitter is minimized, maximizing the power transfer efficiency and improving the system's stability. The circuits are called passive because they do not require active components, such as transistors or amplifiers. Instead, they rely on passive components such as capacitors and inductors to adjust the impedance of the coils. In addition, the circuit is often optimized together with resonant circuits.

Figure 2.7 features the three most known impedance-matching circuit topologies. Figure 2.7(a) is shown L-type circuit matching, which is a network consisting of two components: an inductor ( $L$ ) and a capacitor ( $C$ ), which are connected in a specific configuration. Analogously, Figure 2.7(b) presents a T-type matching network. However, the T-type network comprises a capacitor ( $C$ ) and two inductors ( $L_1$  and  $L_2$ ). Finally, Figure 2.7(c) presents a  $\pi$ -type matching network, which is composed of an inductor ( $L$ ) and two capacitors ( $C_1$  and  $C_2$ ). In both networks shown, the inductor and capacitor values are chosen such that the total reactances system cancel each other out at the operating frequency, which results in a purely resistive impedance.

The choice of each topology shown in Figure 2.7 is defined according to the characteristics of the WPT system. In (GUO; DONG, 2019), for example, the best topologies of passive impedance optimizer for an MCWPT system of multiple receivers are studied. The advantage of passive matching circuits is that they are simple and easy to implement and provide excellent impedance matching over a wide range of frequencies. In some cases, however, passive matching networks become limited in frequency bandwidth and can increase resistive loss. In this case, the use of active networks becomes essential.

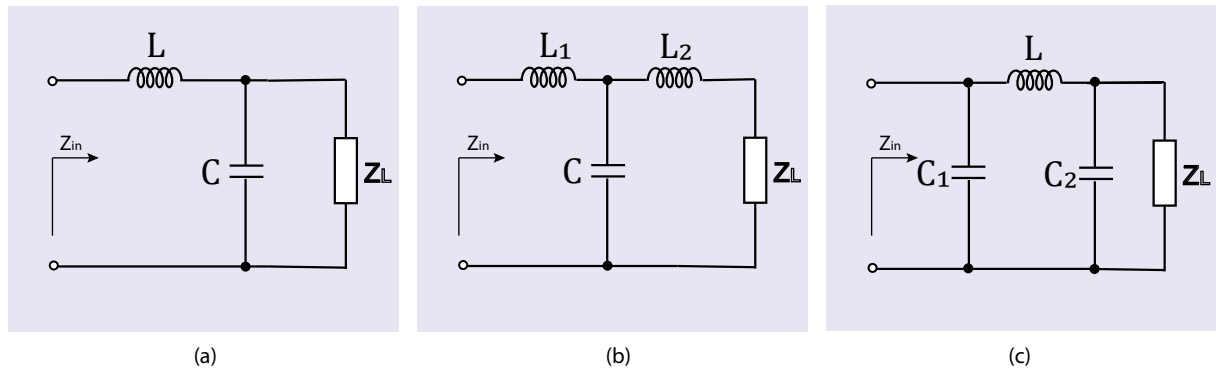


Figure 2.7 – Three types of LC circuit configurations for impedance matching networks: (a) L-type, (b) T-type, and (c)  $\pi$ -type.

## 2.4.2 Active Matching Circuit

Active impedance matching circuits in WPT systems are another way to optimize power transfer from the transmitter coil to the receiver coil in a magnetically coupled system. The active matching circuit includes an amplifier and a feedback loop that adjusts the impedance at the receiver coil to match the impedance of the transmitter coil, maximizing the power transfer efficiency. In addition, this type of circuit can dynamically adjust the impedance to account for variations of load or operating conditions, making it more flexible and efficient than passive matching circuits, as shown in (DAI; LUDOIS, 2015).

Another type of impedance optimizer used in MCWPT systems is the so-called Non-Fosters circuits. In electrical engineering, a non-Foster circuit is a circuit with a negative frequency-dependent impedance; that is, as the input signal frequency increases, the circuit impedance decreases. Non-Foster circuits are often used to optimize the impedance of a circuit, which can improve performance in several ways.

One example of a non-Foster circuit is the Negative Impedance Converter (NIC), which is a circuit that can convert a positive impedance into a negative impedance. As shown in Figure 2.8, the NIC consists of an amplifier and a feedback loop that includes a capacitor and a resistor. The negative impedance created by the NIC can be used to cancel out the positive impedance of other circuit elements, which can improve the overall impedance of the circuit.

Overall, non-Foster circuits are a powerful tool for optimizing the impedance of a circuit. By using negative impedance to cancel out positive impedance, non-Foster circuits can improve the quality factor  $Q$  of the MCWPT, as shown in (KIM et al., 2019), where the loss of the transmitting coil is reduced to  $0.1 \Omega$ , and yielding a quality factor of 7,050, which is 19.1 times higher than that of the conventional coil. Finally, as shown by (2.5) increasing the quality factor, there is also an increase in the efficiency of the system.

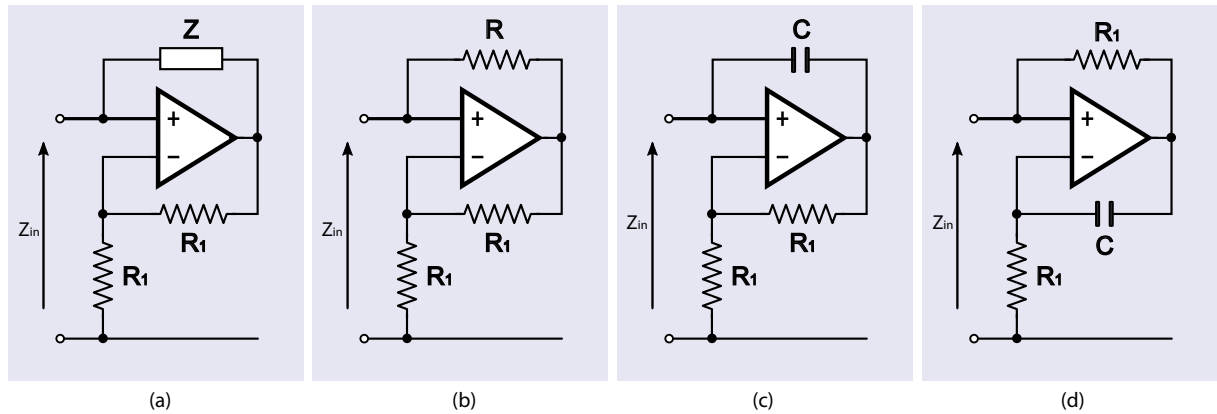


Figure 2.8 – Four types of NIC for non-Foster matching networks: (a) Negative impedance circuit, (b) Negative resistance circuit, (c) Negative capacitance circuit, and (d) Negative inductance circuit.

## 2.5 Partial Conclusions

In this chapter, a review of the literature on wireless power transfer systems is presented. First, a brief introduction to WPT technologies was presented, followed by a discussion of the operating principle of the MCWPT system. In addition, the circuit model of MCWPT systems was also analyzed to investigate the factors that influence their efficiency. For instance, the main factors that define power transfer efficiency are the coupling between the system resonators and the impedance matching of the entire system with the source and load impedances. Subsequently, the effects of metasurfaces on enhancing MCWPT systems and their characteristics were discussed based on magneto-inductive waves theory. Finally, possibilities for optimizing the impedance of WPT systems to increase transmission efficiency were presented.

## 3 Circuit Modeling for Analysis of the MCWPT Systems

In this chapter, the electromagnetic problem concerning MCWPT systems is described and formulated by applying approximate and quasi-static methods in a circuit model proposed in (FREITAS et al., 2022a) and (FREITAS et al., 2022b). First, the characteristic parameters, such as resistance and self-inductance of a printed inductor, are calculated using approximate methods. Next, the one-dimensional numerical formulation analogous to the thin-wire approximation is used to calculate mutual inductance.

For the analysis of the circuit model of the MCWPT, it is considered in the approach the unknown current along the microstrip is regarded as a single value distributed in each modeled coil. First, computational aspects related to the implementation of the developed model are discussed. Then the calculated results are compared step-by-step with commercial software based on electromagnetic methods in the frequency domain. Finally, the microstrip model is experimentally validated with transmission coefficient measurements.

### 3.1 Problem Description

The efficiency of MCWPT systems is directly related to the coil's quality factor ( $Q$ ) (MAO et al., 2018). Since the coil's self-inductance is determined by its electromagnetic and geometrical parameters, the latter must be designed to achieve maximum efficiency. Printed coils are used in this work once these structures can be easily prototyped, are lightweight, and present low production costs. The geometry chosen was a square one, as shown in Figure 3.1, since this topology has a higher  $Q$  factor than other geometries (MAO et al., 2018). Another advantage from the numerical point of view is that this topology simplifies the calculation of the circuit parameters, such as the self-inductance, the characteristic resistance of the inductor, and the mutual inductance between two coils.

The coil topology used in the following analysis is presented in Figure 3.1, and its dimensions are described in Table 3.1. In this chapter, the Tx and Rx coils and the metamaterial cells are geometrically identical. The lumped capacitor specific for RF applications is used in each unit cell of the metasurface with a capacitance of  $(100 \pm 1\%)$  pF. The Tx and Rx coils do not have impedance matching circuits or resonance capacitors; they only have two vias each, connected to an SMA connector for connecting to the power source and load, respectively.

The coils and the metasurface were etched on a fiberglass substrate (Flame Resistant 4 \_ FR4) with 1.60 mm thickness and copper thickness of 0.035 mm. It should be pointed out that the following formulation does not take into account the dielectric properties of the FR4 since simulations and experimental tests showed that at the analyzed frequency range of MCWPT

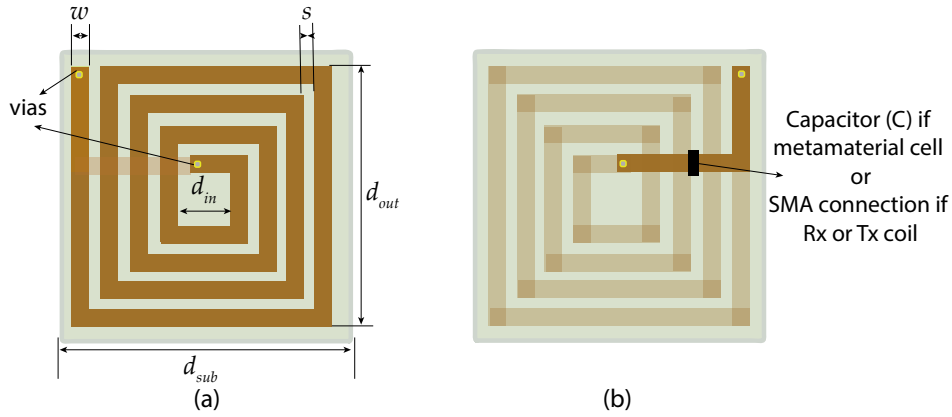


Figure 3.1 – Specification of the square printed coil geometry used in this work: (a) top layer, (b) bottom layer.

Table 3.1 – Characteristic of the printed inductor shown in Figure 3.1 used in the study

Geometric Specifications	
Number of turns ( $n$ )	4
$d_{sub}$	50 mm
$d_{out}$	46 mm
$d_{in}$	10 mm
$w$	3 mm
$s$	2 mm

systems, the influence of this material on the performance of the system can be disregarded.

## 3.2 Calculation of the Characteristic Parameters of the Coil

Some previous works have been published on calculating the self-inductance of a printed inductor. In (NEJADPAK et al., 2011) uses an approximate method to calculate the self-inductance of a planar inductor and performs an optimization of size; the smallest possible inductor size is realized through the utilization of the Finite Element Method (FEM) and genetic algorithms. In (EDN, 2010) is shown a method approximation for calculation self-inductance for designing multilayer planar spiral inductors. On the other hand, in (FARIA et al., 2021), a fast and analytical method for calculation self-inductance of multilayer planar spiral inductors calculation is proposed as more precise than previous. This work applies the formulation presented in (NISHIMURA et al., 2014), in which the coil's inductance is given by:

$$L = \frac{K_1 \mu_0^2 n^2 d_{avg}}{1 + K_2 \rho_L}, \quad (3.1)$$

where  $\mu_0$  is the magnetic permeability of the vacuum,  $d_{avg} = 0.5 \cdot (d_{in} + d_{out})$ ,  $n$  is the number of turns, and  $\rho_L = (d_{in} - d_{out}) / (d_{in} + d_{out})$ . Finally,  $K_1 = 2.34$  and  $K_2 = 2.75$  are constants defined in (MOHAN et al., 1999). It was decided to use the simple expression (3.1), since, in addition

to being simple, it proved to be efficient in the calculation of the proper inductance, leading to values close to those measured as in (NISHIMURA et al., 2014).

The formulation presented here considers the characteristic resistance of the printed coil ( $R_T$ ) to be composed of a static (DC) ( $R_{DC}$ ) and a frequency-dependent (AC) component ( $R_{AC}$ ), that is:

$$R_T = R_{DC} + R_{AC} \quad (3.2)$$

The DC resistance is a function of the coil's geometric parameters and the resistivity  $\rho_r$  of the conductor:

$$R_{DC} = \frac{\rho_r l}{A} \quad (3.3)$$

where  $l$  is the perimeter of the coil, and  $A$  is the conductor cross-section. As presented in (3.3), the  $R_{DC}$  models the static ohmic losses in the coil.

On the other side, the AC resistance of a planar inductor is given by (3.4) (see the proof in Appendix B), where  $\lambda$  is the wavelength. The formulation (3.4) represents the radiation resistance of a small loop (HUI; YISHENG; BAISHAN, 2005):

$$R_{ac} = 320 \frac{\pi^4 d_{out}^4}{\lambda^4} \quad (3.4)$$

In some cases, using only loops of small electrical size, radiation losses are minimized following the radiation resistance (HUI; YISHENG; BAISHAN, 2005). There are other ways to calculate the radiation resistance, as shown in (LORRAIN; CORSON, 1970) and (KUHN; IBRAHIM, 2001). However, this paper used (3.4) discussed in (HUI; YISHENG; BAISHAN, 2005) because it is simpler to implement. However, all methods presented are approximated and derived from the calculation of the Poynting vector.

All formulations presented in this section proved suitable for near-field applications studied in this work. In the sequence, the method is approached to calculate the self-induction of printed loops.

### 3.3 Calculation of the Mutual Inductance Between Coils

The mutual inductance between two coils can be calculated using the Neumann formulation in (3.5). Aiming to explain the Faraday inductance phenomenon using the force between Ampère current elements, Neumann carried out a theoretical development that led to the concept of potential vector and coefficient of inductance. In this work, the path Neumann followed to start from Ampère's theory and arrive at a theory that explained Faraday's induction would not be presented. To better understand the formulation, consider two simple coils  $\Gamma_1$  and  $\Gamma_2$ , which flow the currents  $I_1$  and  $I_2$  respectively, as shown in Figure 3.2. In (3.5), the current element



of the circuit  $\Gamma_1$  is  $I_1 d\vec{r}_i$  located in the position vector  $\vec{r}_i$ , while a circuit element  $\Gamma_2$  is  $I_2 d\vec{r}_j$  located in  $\vec{r}_j$  defined in the tridimensional space  $\mathbb{R}^3$ , respectively, at a distance  $r_{ij}$  from the origin. Therefore, any arbitrary positioning between the coils can be evaluated through (3.5) by properly assigning the vectors  $\vec{r}_i$  and  $\vec{r}_j$ .

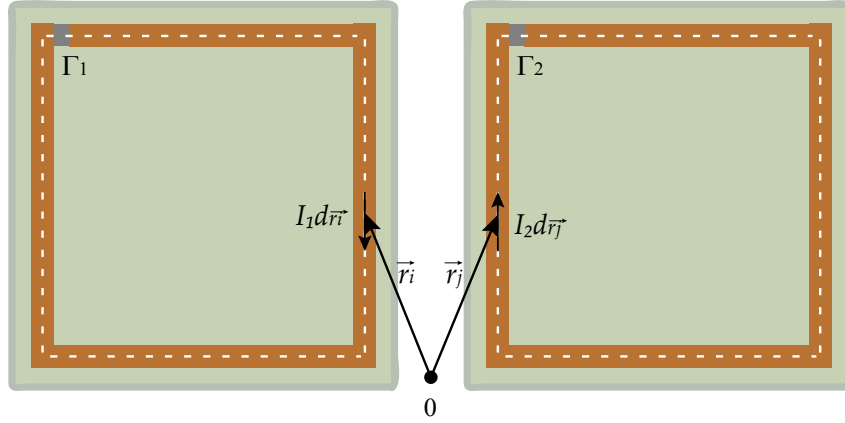


Figure 3.2 – Two simple square printed coils representing two closed circuits  $\Gamma_1$  and  $\Gamma_2$  with current elements  $I_1 d\vec{r}_i$  and  $I_2 d\vec{r}_j$ , respectively.

$$M_{12} \equiv \frac{\mu_0}{4\pi} \oint_{\Gamma_1} \oint_{\Gamma_2} \frac{d\vec{r}_i \cdot d\vec{r}_j}{r_{ij}} = M_{12} \quad (3.5)$$

The integral formulation presented in (3.5) is general and is valid for any geometry. However, this chapter uses a 4-turn coil with square geometry, as shown in Figure 3.1, presenting symmetries that simplify the integral evaluation. Figure 3.3 illustrates two coplanar and parallel coils used in the proposed system, and it shows the numbering of the segments and the origin taken in the  $xy$  plane for the odd and even elements of loops. Figure 3.3 also shows the modeling to calculate the mutual inductance between segment 3 of the first ( $y_{1,3}$ ) and segment 1 of the second ( $y_{2,1}$ ). The integration path indicated by the dashed white line must be closed this way; a small part of the coil extremity highlighted in Figure 3.3 can be excluded from the integration since the current density in this border part can be neglected, as highlighted. The integral that allows this calculation is presented in (3.6).

The analyzed system presents symmetries that simplify the integral evaluation. First, the values of  $m_1$  and  $m'_1$  are calculated for each segment. Figure 3.3, for segment 3 of the left loop,  $m_{1y} = d_{out} - w = a$  and  $m'_{1y} = m_1 + a$  while the values of  $m_2$  and  $m'_2$  can be obtained from the values of  $m_1$  and  $m'_1$  referring to segment 1 of the reference loop. For instance, in the odd segments  $m_{2y} = m_{1y} + dy$  and  $m'_{2y} = m'_{1y} + dy$ , where  $dy = (a + e) \cdot dify$  in which  $a$  is the length of the longest segment,  $e$  is the distance between two vertical segments, and  $dify$  the differential distance in  $y$  of the two coils. Conversely, for the even segments,  $m_{2x} = m_{1x} + dx$  and  $m'_{2x} = m'_{1x} + dx$ , where  $dx = (a + e) \cdot difx$  in which  $a$  is the length of the longest segment,  $e$  is the distance between two between horizontal segments, and  $difx$  the differential distance in  $x$  of the two coils.

Finally, to be able to express the value of  $h$  between some segments correctly, it is necessary to use the distance between the two patterns plus the partial contributions of each segment. We then obtain, for example, for a pair of segments  $i$  and  $j$ : for the case presented in Figure 3.3,  $h = dy + m_{2y} - m_{1y}$  if they are even, and  $h = dx + m_{2x} - m_{1x}$  if they are odd. In this way, the integral that relates segment 3 of the first coil ( $y_{1,3}$ ) and segment 1 of the second ( $y_{2,1}$ ) can be written as (3.6).

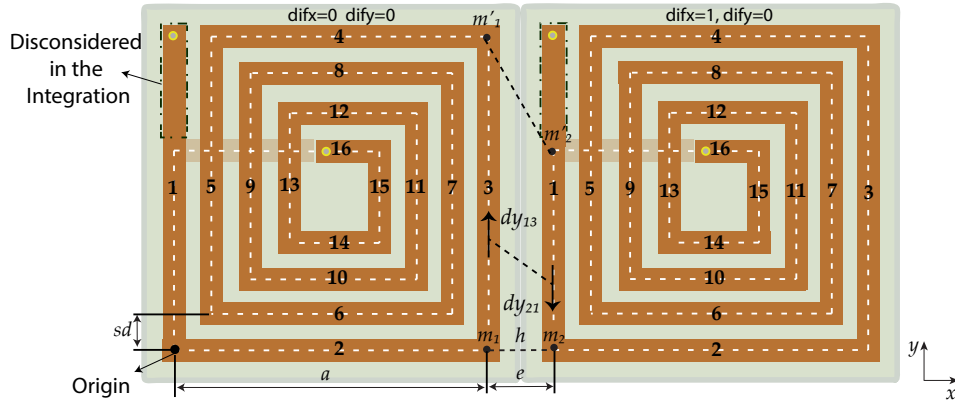


Figure 3.3 – Integration model for the case of two side-by-side coplanar coils, the contribution of segment 3 of the first coil ( $y_{1,3}$ ) with segment 1 of the second coil ( $y_{2,1}$ ).

$$M_{3,1} \equiv \frac{\mu_0}{4\pi} \int_{m_{2y}}^{m'_{2y}} \int_{m_{1y}}^{m'_{1y}} \frac{d\vec{y}_{1,3} \cdot d\vec{y}_{2,1}}{\sqrt{h^2 + (y_{1,3} - y_{2,1})^2}} = M_{3,1} \quad (3.6)$$

For the case where the coils are non-coplanar, as shown in Figure 3.4, the calculations of  $m_1$ ,  $m'_1$ ,  $m_2$ , and  $m'_2$  are the same as in the coplanar case. However, for the calculation of  $h$ , we use  $h = \sqrt{(dy + m_{1y} - m_{2y})^2 + dz^2}$  if they are even, and  $h = \sqrt{(dx + m_{1x} - m_{2x})^2 + dz^2}$  if they are odd. The  $z$ -index indicates that the coil is axially separated from the other loop taken as a reference in the space. Finally, the distance between the segments is given by  $dz$ .

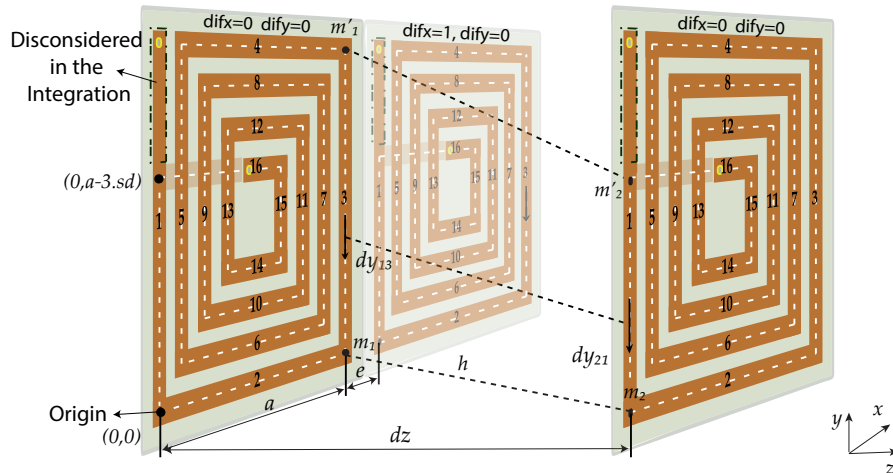


Figure 3.4 – Integration model for the case of two non-coplanar coils, the contribution of segment 1 of the first coil ( $y_{1,1}$ ) with segment 1 of the second coil ( $y_{2,1}$ ).

It must be pointed out that the microstrip lines presented in Figure 3.3 are modeled as thin-wire structures located in the middle of the printed coil trace, which is a valid approximation in the operating frequency of MCWPT systems once the trace thickness is much smaller than the wavelength and the geometrical size of the full structure (BALANIS, 2015). Both (3.5) and (3.6) can be solved using traditional numerical methods such as the Gaussian quadrature, widely used in integration problems. However, as proposed in (DURAND, 1968), it is possible to use an algebraic simplification such as (3.7), which allows the minimization of computational time and is ideal for solving problems with geometry similar to the one proposed in this study.

$$\begin{aligned}
M = \pm \frac{\mu_0}{4\pi} \left\{ \sqrt{h^2 + (m'_2 - m'_1)^2} - (m'_2 - m'_1) \log \left[ (m'_2 - m'_1) + \sqrt{h^2 + (m'_2 - m'_1)^2} \right] - \right. \\
\left. - \sqrt{h^2 + (m'_2 - m_1)^2} + (m'_2 - m_1) \log \left[ (m'_2 - m_1) + \sqrt{h^2 + (m'_2 - m_1)^2} \right] - \right. \\
\left. - \sqrt{h^2 + (m_2 - m'_1)^2} + (m_2 - m'_1) \log \left[ (m_2 - m'_1) + \sqrt{h^2 + (m_2 - m'_1)^2} \right] + \right. \\
\left. + \sqrt{h^2 + (m_2 - m_1)^2} + (m_2 - m_1) \log \left[ (m_2 - m_1) + \sqrt{h^2 + (m_2 - m_1)^2} \right] \right\} \quad (3.7)
\end{aligned}$$

The expression (3.7) returns the contribution of a pair of coil segments. Thus, to calculate the total mutual inductance, it is necessary to repeat this process for each possible couple of segments along the inductor geometry. Therefore, the number of iterations to calculate the mutual inductance between two coils is equal to  $(N_{seg1} \cdot N_{seg2})/2$ , where  $N_{seg1}$  is the number of segments of one loop and  $N_{seg2}$  of the other. However, perpendicular components have null inductance, as in pairs composed of odd and even segments. In this way, the number of iterations for evaluating the mutual inductance can be reduced by calculating only the contribution between the pairs of odd-odd  $M_{odd}$  and even-even segments  $M_{even}$ . Then, the total mutual inductance is given by the sum of these contributions, *i.e.*,  $M_{Total} = \sum_n M_{odd} + \sum_n M_{even}$ .

In this work, the algorithm to calculate the mutual inductance was implemented in Matlab<sup>®</sup>. This script calculates the mutual inductance between the metamaterial unit cells using the coplanar case shown in Figure 3.3, whereas the mutual inductance between the receiver or transmitter coils and the unit cells corresponds to the non-coplanar analysis. In this case, as shown in Figure 3.4, one of the coils (receiver or transmitter) is positioned at a specific axial separation from the resonant surface.

### 3.4 Validation

This section uses the designed and prototyped MCWPT system composed of two coils and a metamaterial to experimentally validate the models proposed in Section 3.1 in the frequency band from 1 to 30 MHz. Thus, the following are analyzed according to modifying the receiver's

position: the efficiency and the frequency division phenomenon are evaluated. We suppose that the excitation voltage  $V_s$  is known. There is no current in the receiver ( $I_r = 0$ ) for the available preliminary approach. The method may be applied to other conditions by considering the corresponding circuit equations in (2.2).

### 3.4.1 Measurement of the Characteristic Parameters of the Coil

The comparison between the coil calculated parameters ( $CV$ ) and measured value ( $MV$ ) are shown in Table 3.2. The self-inductance was calculated using (3.1) and characteristic resistance (3.2). The deviation is calculated as  $(CV - MV)/MV \times 100$ . Therefore, it was observed that the self-impedance was approximately 8%, which is a reasonable value compared to other methods presented in Section 3.2 and to the tolerance of commercial coils that can reach up to 20%. However, an 8% correction on the calculated value was taken into account in order to reduce the propagation error when simulating the full RWPT system. Conversely, the characteristic resistance is shown in Table 3.2. In this case, the deviation was more minor than the deviation from the measured value, less than 3%, which validated the proposed model.

In the measurements presented in Table 3.2, an impedance meter configured at a frequency of 24 MHz was used for both inductance and resistance measurements (see the Measuring Setup in the Appendix C). This frequency is chosen due to the resonant frequency of the metasurface to be used. However, in practice, there would not be significant variations in the operating range (1 to 30 MHz).

Table 3.2 – Values obtained characteristic of the printed inductor used in the study

	Calculated	Measured	Deviation
Self-Inductance	475 nH	437 nH	8.7%
Characteristic Resistance	76 mΩ	78 mΩ	2.6%

### 3.4.2 Evaluation of the Mutual Inductance Between Coils

To validate the numerical approach proposed to evaluate the mutual inductance between the coils, the value is calculated for two coplanar coils by applying the approximation introduced in (3.7) and is compared with the numerical evaluation of (3.6) by using the Gaussian quadrature method. Both approaches were implemented in Matlab<sup>®</sup> on a computer with an Intel<sup>®</sup> Core<sup>™</sup> i5 – 2450M processor, 8 GB RAM, and 2.50 GHz clock.

The mutual inductance obtained from both methods and the computation time are presented in Table 3.3. As can be seen, both methods lead to similar results. However, the integral approximation reduces the simulation time by about 52 times compared to the Gaussian quadrature solver. This difference can become even more significant with more complex elements, such as coils with more turns, or when the calculation involves more loops. The advantage of this type of modeling can be even more significant when compared to commercial software.

Table 3.3 – Values obtained to calculate the mutual inductance between two side-by-side coplanar coils using Gaussian quadrature and approximation

	Gaussian Quadrature	Analytical Approximation
Mutual Inductance	$-14.0897 \text{ nH}$	$-14.0782 \text{ nH}$
Computation Time	$1.57 \text{ s}$	$0.03 \text{ s}$

The geometric simplification of the coil presented in Figure 3.3 and Figure 3.4 can be justified if we consider the surface distribution of the magnetic field in the printed inductor on FR4 substrate for operation at  $24 \text{ MHz}$ . Figure 3.5 shows this magnetic field distribution obtained by a full-wave simulation using the frequency domain solver of CST Studio Suite<sup>®</sup> and adaptive mesh refinement at the frequency of  $24 \text{ MHz}$  to get more precision in the simulation. It is possible to verify that the field is concentrated more in the internal region of the coil, and the extremity not considered has low field levels, which justifies that the geometric simplification is a good choice.

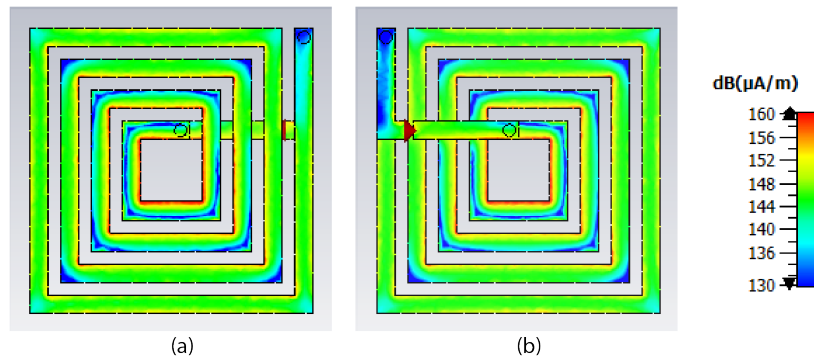
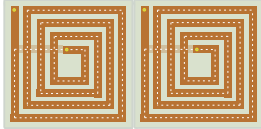
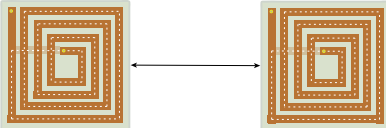
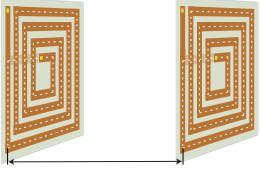


Figure 3.5 – Surface current distribution in the printed inductor: (a) front view, (b) back view.

As shown in Figure 2.4, the modeled MCWPT system has one pair of Tx and Rx coils and a resonant metasurface. First, the algorithm to calculate the mutual inductance of the metamaterial cells was implemented in Matlab<sup>®</sup> using the formulation described in Section 3.3 for coplanar coils and shown in Figure 3.3. This script can also calculate the mutual inductance between the receiver and the cells of the metasurface. In this case, as shown in Figure 3.4, one of the coils is the receiver positioned at a specific axial separation from the resonant surface and in the position  $XY$ . Then, the mutual inductance between the source coil and the metamaterial cells is analyzed.

The validation of the modeling for the two-coils coplanar case, as shown in Figure 3.3, the calculation was performed using (3.7) between the segment pairs, and then measurements were performed on a Vector Network Analyzer (VNA); for this purpose, two types of analysis were used (see the Measuring Setup in the Appendix D). In the first one, the side-by-side case is carried out, which considers the spacing between the coils of  $10 \text{ mm}$ , as it is in the projected metamaterial. Next, the side-by-side gap case was performed to model the mutual inductance between non-adjacent coplanar coils separated by  $50 \text{ mm}$ . Finally, in the face-to-face case shown in Figure 3.4, (3.7) is also used as the appropriate parameter, then measurement was performed  $20 \text{ mm}$  away between coils. The validations described are shown in Table 3.4.

Table 3.4 – Values of the mutual inductance between two printed coils for the experimental case and the case calculated by the proposed model

	Calculated Value	Measured Value	Deviation
 Side-by-side	14.078 nH	14.295 nH	1.52%
 Side-by-side (gap 50 mm)	1.770 nH	1.784 nH	0.8%
 Face-to-face (gap 20 mm)	81.256 nH	83.911 nH	3.16%

The results presented in Table 3.4 corroborate the validation of the model since the difference between the values obtained is very small and demonstrates its applicability for different coil arrangements and positioning. The difference may be due to measurement errors and some parameters not considering, for example, connector influence, and parasitic capacitances. The mutual inductance for the presented cases was evaluated in the VNA and also in the frequency of 24 MHz.

The matrix mutual inductance of the metamaterial is calculated for a script that was used in Matlab<sup>®</sup>. A square block with  $10 \times 10$  cells means that one must find only  $(10 \times 9)/2$  mutual inductances if we consider the reciprocity of each pair of coils. Figure 3.6 shows the level of coupling between the cells of the metamaterial obtained by the script. In this image, the first coil  $i = j = 1$  is used with reference. The script calculates the mutual inductance between the possible coil pairs with the given coordinates, lasting only 0.778 s. However, the computational cost increases exponentially with the increase in the number of metamaterial cells, as shown in Figure 3.7.

Only the magnetic interactions between neighboring coils are considered in many inductive coupling applications using a resonant surface. However, when working with a miniaturized system with a low modulus of inductance, it is essential to carry out a more detailed analysis of the system's sensitivity. For example, in Figure 3.6, it is possible to verify that the interaction between the neighboring coils is more attractive; however, changes in some loops that close but not necessarily neighboring can change the coupling seen by the first coil.

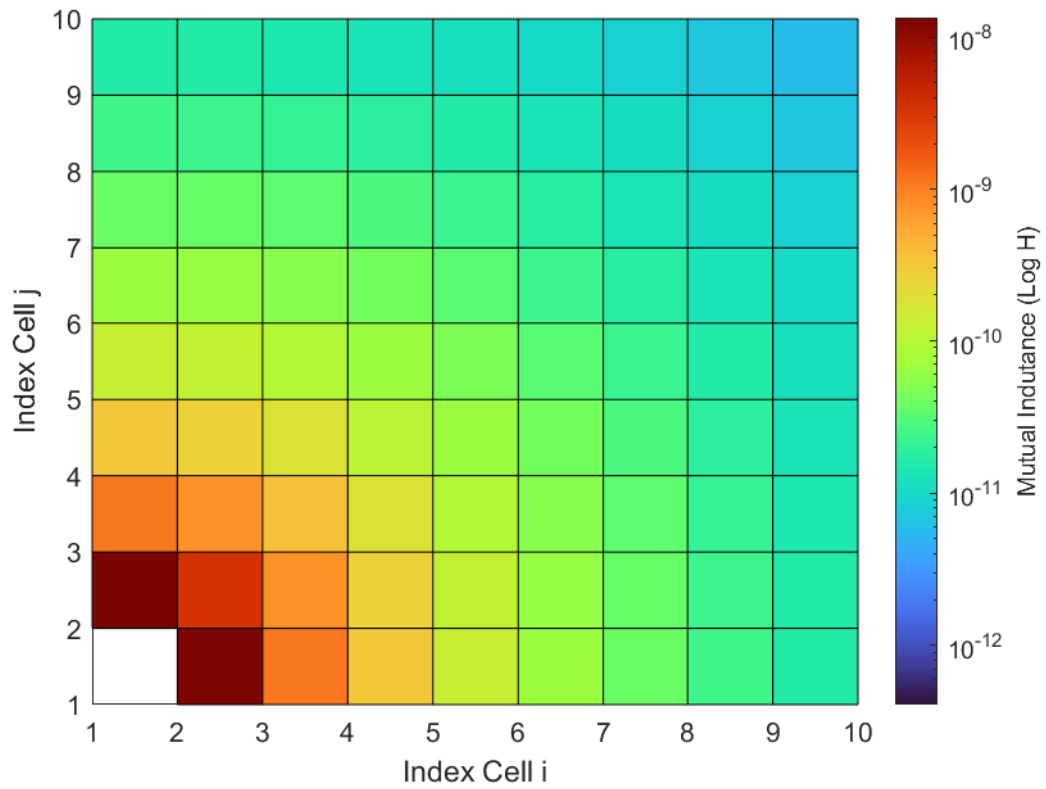


Figure 3.6 – The variations of  $M$  as a function of the cell's relative position  $(x_i, y_j)$  on a 2D metamaterial,  $10 \times 10$  cells. It is taking as reference the cell  $i = j = 1$ .

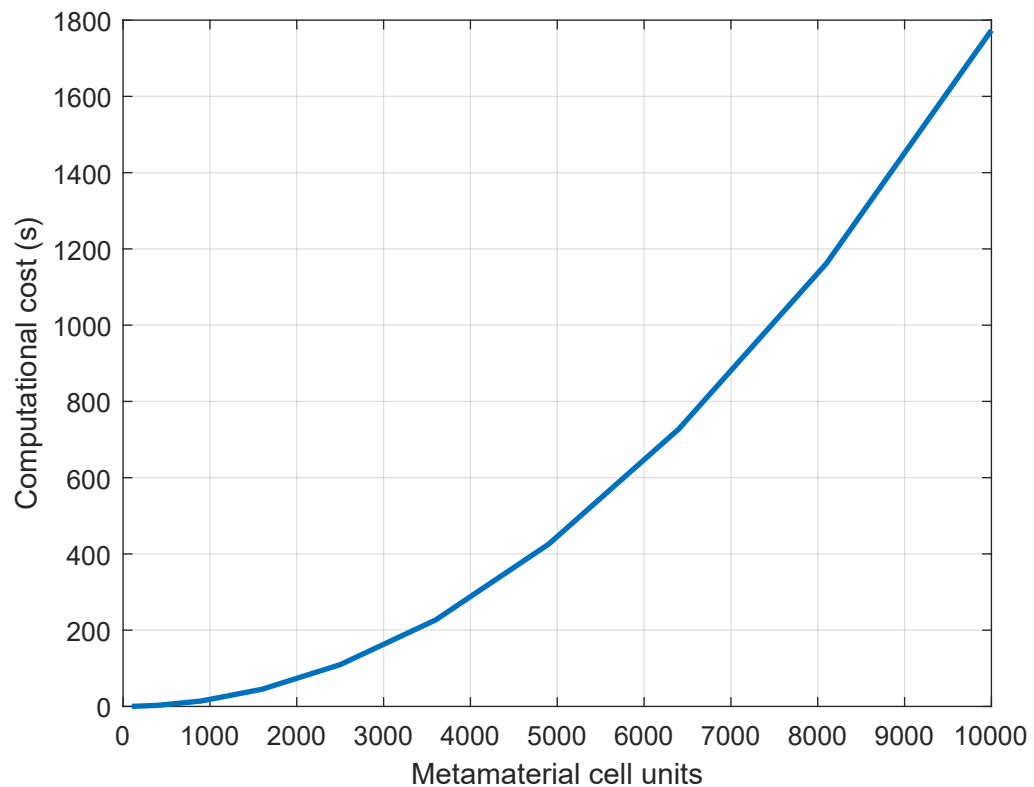


Figure 3.7 – The computational cost for the calculation of the mutual inductance matrix of the metasurface.

### 3.4.3 Frequency Analysis of MCWPT Systems with Resonant Metasurface

Evaluating and measuring the scattering parameters are essential to analyzing the performance of a WPT system. Notably, the reflection ( $S_{11}$ ) and transmission ( $S_{21}$ ) coefficients allow us to evaluate the power loss due to impedance mismatching and the  $PTE$ , among other performance parameters. For our study, we started with the analysis of  $S_{21}$  since it provides information about the amount of power delivered to the receiver. With this, it is possible to evaluate the operating band, as well as the function of the values of each element with the variation of the behavior of the signal in the transmission.

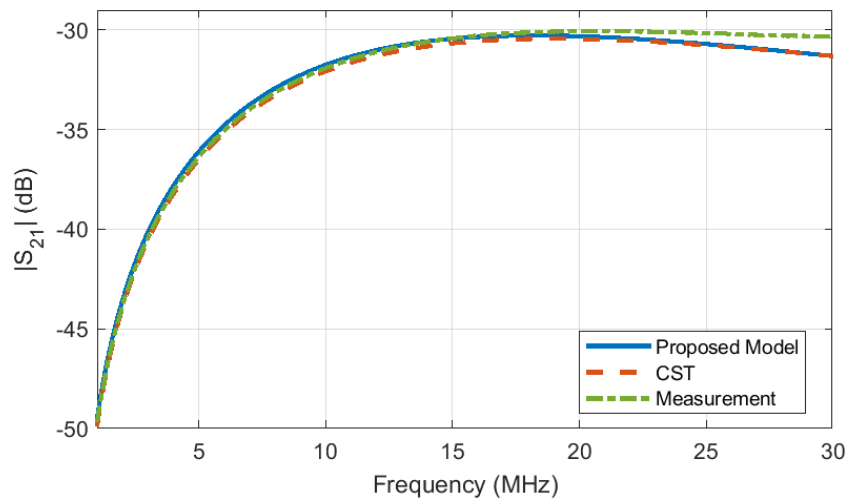
The designed MCWPT system described in Section 3.1 was simulated using the frequency domain solver of CST Studio Suite<sup>®</sup> and adaptive mesh refinement at the frequency of 24 MHz. First of all, a two-coil MCWPT system was considered without the resonant metasurface. In this case, the Tx and Rx were positioned in three different positions: (a) side-by-side separated by 10 mm, (b) side-by-side separated by 50 mm, and (c) face-to-face, separated by 20 mm. The  $|S_{21}|$  results obtained from the full-wave simulation in CST<sup>®</sup>, the proposed circuit model, and measurements are presented in Figure 3.8 for each case (see the Measuring Setup in the Appendix E). It should also be noted that the values of  $Z_s$  and  $Z_L$  of the circuit model considered in this exploration were 50  $\Omega$  each.

As shown in Figure 3.8, the results obtained with the proposed circuit model and the full-wave simulation are in close agreement. However, there is a deviation between simulated and measured results when analyzing the side-by-side cases presented in Figure 3.8(a) and Figure 3.8(b). This deviation becomes more significant for frequencies over 20 MHz, and it is due to electromagnetic interference caused by proximity between the connectors and the low coupling between coils in the side-by-side configuration. Moreover, that deviation is not verified in the face-to-face results in Figure 3.8(c), which has presented a stronger coupling between coils as shown in 3.4. Generally, the results obtained corroborate the proposed two-coplanar model for both coplanar and non-coplanar conditions.

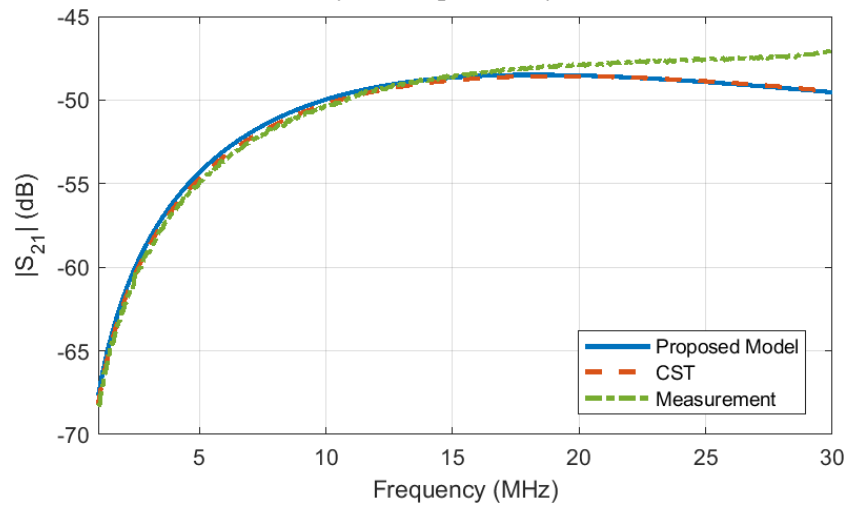
Subsequently, the performance of the designed MCWPT system with a resonant metasurface composed of  $4 \times 4$  cells and two coils Tx and Rx, located in positions (1,1) and (1,3), respectively, on the metasurface, is experimentally evaluated using the measurement setup in 3.9(a). Moreover, the measured results are compared with those obtained with the proposed circuit model and simulations using a frequency solver and adaptive mesh refinement in CST<sup>®</sup>, as presented in Figure 3.9(b). As can be noticed, both results are in good agreement for lower frequencies. However, the deviation increases with frequency once parasitic capacitances between coils and the losses in the substrate are disregarded in the CM but are taken into account in the full-wave simulation. Regarding the computational time, the electromagnetic simulation took about 609 s. In comparison, CM solved in 0.33 s, *i.e.*, almost 1800 times faster, on a computer with an Intel<sup>®</sup> Xeon<sup>™</sup> W – 2275 processor, 256 GB RAM, and 3.30 GHz clock.

It should be noted that an accurate capacitor series model was used to implement the metamaterial to increase the model's accuracy, as shown in Figure 3.10(a). In this case, the

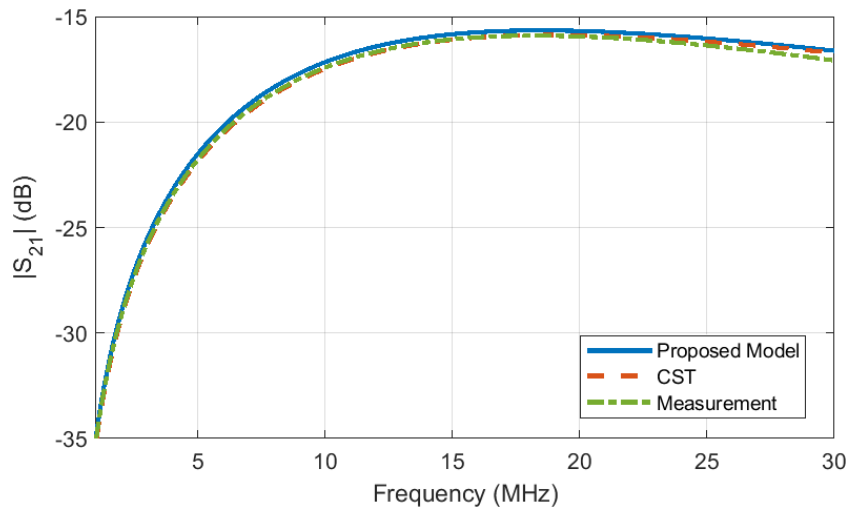




((a)) Side-by-side separated by 10 mm.



((b)) Side-by-side separated by 50 mm.



((c)) Face-to-face separated by 20 mm.

Figure 3.8 –  $|S_{21}|$  results from the proposed circuit model as well as full-wave simulations in CST<sup>®</sup> and measurements for different positioning in a two-coil WIPT system without resonant metasurface.

capacitance  $C$  is the nominal component, the resistance  $R_{ESR}$ , and the inductance  $L_{ESL}$  were obtained by measuring the capacitor on the same impedance meter used earlier to measure the characteristic resistance of the printed coil. The value of  $L_{ESL}$  is much smaller than the inductance of the metamaterial cell, so it was disregarded. However, the value of  $R_{ESR} = 200\text{ m}\Omega$ , greater than the characteristic resistance of each metamaterial cell, thus this value was considered in the implementation; this way, the metamaterial cell model used is shown in Figure 3.10(b).

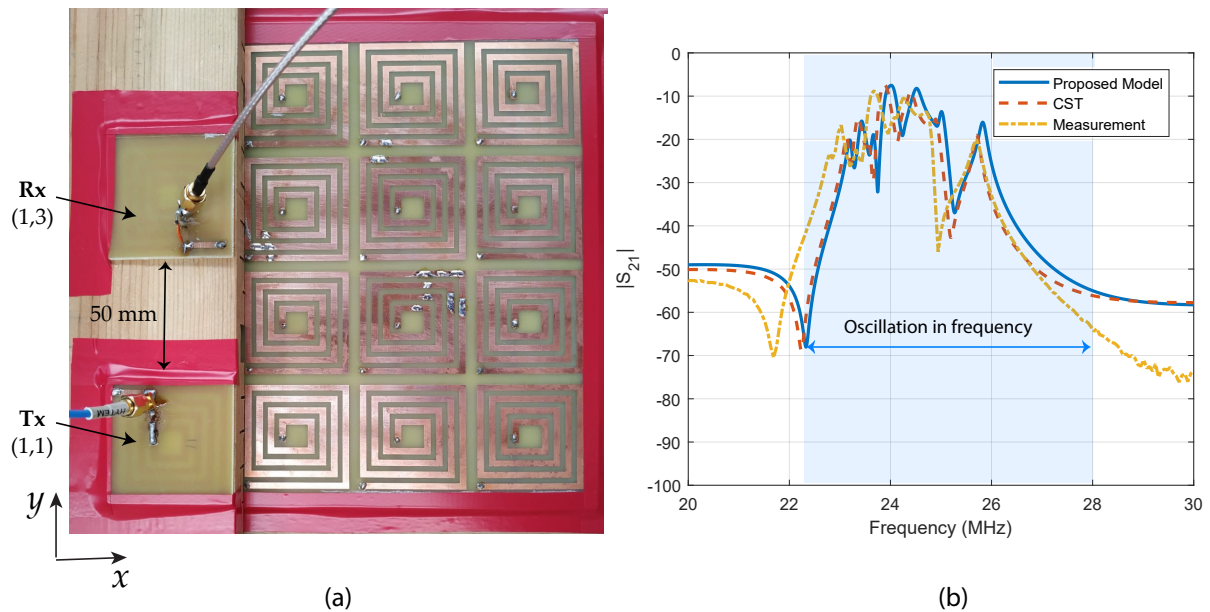


Figure 3.9 – MCWPT system with a resonant surface: (a) experimental setup applied to wireless power coupling studies; (b) simulated, calculated, and measured  $S_{21}$  results.

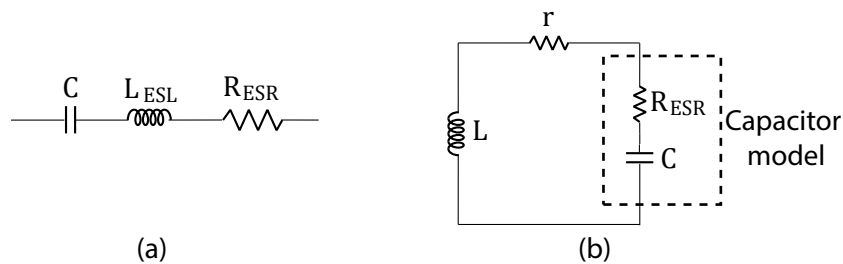


Figure 3.10 – Considerations: (a) capacitor series model, and (b) metasurface cell model used.

Analyzing Figure 3.9(b), the system oscillation in frequency is checked, which ranges from 22.3 to 28 MHz in this case. Based on the calculated circuit parameters presented and validated in Section 3.4.1, the self-inductance value used was 437 nH and the capacitance of 100 pF, leading to a resonant frequency around 24 MHz. Therefore, as indicated in Figure 3.9(b), the optimal frequency, the frequency in which the efficiency reaches its maximum, is precisely the resonant frequency of the metasurface.

A frequency deviation of approximately 300 kHz at the peak of the  $|S_{21}|$  was observed between measured and simulated results, as shown in Figure 3.9(b). This deviation is mainly due to the tolerance of the lumped capacitors of the metasurface cell. Even though the system

was prototyped with capacitors with 1% tolerance capacitor, this slight variation is enough to shift the optimal frequency once resonant WPT systems are significantly narrowband. Not to mention parasitic capacitances, neglected in the circuit modeling but considered in the full-wave simulation. Another difference in the measurement curve is that the metasurface operating band is slightly larger and has a more accentuated decay at higher frequencies. The justification for such behavior is possibly electromagnetic interference in the measurement, and the influence of the connector is not considered in the simulations.

Finally, the circuit analysis method and the numerical approach for calculating the mutual inductance presented in this work are proven to be precise and computationally efficient for analyzing large-sized structures much faster than full-wave simulations. Moreover, the fact that it is a 3D resolution method has advantages over other methods of analyzing large metamaterial-based WPT systems such as the one presented in (KRÄHENBÜHL *et al.*, 2020).

### 3.5 Partial Conclusions

In this chapter, mathematical modeling of thin microstrip structures is proposed to quantitatively evaluate the behavior of coils and metamaterial surfaces. This model is based on a circuit model whose parameters are calculated using approximation methods and quasi-static formulations to calculate self-inductance, mutual inductance, and characteristic resistance.

Different case studies were performed to determine the validity of the proposed approach, and the results were compared with simulations in commercial software and measurements. It was demonstrated that the proposed implementation could accurately describe the behavior of these structures in the frequency range used.

## 4 Analysis of MCWPT Systems

The present chapter is devoted to exploring the optimization variables of a microstrip-printed MCWPT system. A new design based on printed square coils is proposed, but now reduced in size and operating at  $13.56 \text{ MHz}$ . This system is used to perform a frequency-domain analysis on how the frequency and receiver position over the metasurface affects the energy transmission efficiency. This chapter also analyzes the input impedance variation and the current distribution on the metamaterial surface with respect to variations in the receiver position and the charge rate on the resonant surface. For this, the Magneto-Inductive Waves (MIW) theory is used to investigate a specific application: Passive Position Tracking in Dynamic MCWPT Systems. Finally, it discusses the importance of knowing the current distribution and the impedance optimization parameters for an MCWPT system.

### 4.1 The Optimization Variables in MCWPT Printed Systems

In WPT systems, it is often necessary to use optimization tools to maximize the system's efficiency, considering the system design constraints. For example, some optimization parameters must be observed when dealing with a square coil system like the one presented in Chapter 3. Some of the design constraints that need to be taken into account are the operating frequency band, the materials available for construction, and the space available to allocate the elements of the system

Considering a square coil: increasing the number of turns of the printed coil increases the inductance. In turn, if the external dimension of the coil  $d_{out}$  is kept fixed, the increase in turns  $n$  will imply a decrease in the microstrip line, that is, in the variable  $w$ . Subsequently, this will increase the characteristic resistance of the coil, which increases losses. Thus, it is necessary to have a clear objective of the optimization and to work dynamically with the optimization variables.

Exploration can be carried out to evaluate the electric characteristics of these coils and define their circuit model as proposed in Chapter 3. Initially, a coil with a maximum external dimension  $d_{out}$  of  $40 \text{ mm}$  is considered. The optimization variables are the distance between the microstrip traces  $s$ , the width of the microstrip trace  $w$ , and the internal dimension  $d_{in}$ , which should equal or greater than  $3 \text{ mm}$ . Table 4.1 presents the constructive characteristics of the optimized coils within the mentioned design constraints for five different numbers of windings  $n$ .

Table 4.1 confirms the previously mentioned behavior, in which an increase in inductance with an increase in the number of turns would also lead to an increase in characteristic resistance. This behavior can also be verified in (3.1) and (3.3). We tried not to vary too much the width of the trace  $w$  and the distance of these traces  $s$  since the circuit model for calculating the mutual inductance is bifilar; that is, the variation of the microstrip line is disregarded. However, as

in an optimization keeping the external and internal length of the coil fixed, it is natural that these two variables are changed. In the proposed model, the width of the microstrip line directly influences the characteristic resistance  $R_{dc}$ . Likewise, the distance between traces also to the mutual inductance.

Table 4.1 – Characteristic electrical parameters of a printed coil as a function of the number of turns, and there is an optimization of other constructive parameters, such as line width and distance between lines, in addition to external and internal dimensions.

Turns ( $n$ )	$d_{out}$ (mm)	$d_{in}$ (mm)	$w$ (mm)	$s$ (mm)	Self-induction	Characteristic resistance
3*	32.5	10.8	2.59	1.73	211.75 nH	47.6 m $\Omega$
4	39.8	9.6	2.5	1.7	398.75 nH	82.6 m $\Omega$
5	39	7	2	1.5	533.99 nH	112.2 m $\Omega$
6	39.6	5	1.8	1.3	693.11 nH	145.3 m $\Omega$
7	39.9	4.5	1.5	1.2	921.77 nH	202.8 m $\Omega$

\* Optimized by resonance case, more details in the Section 4.2.

The efficiency behavior due to variations in the number of turns and other design variables must be evaluated. For this intent, two-coil systems considering the cases described in Table 4.1 are designed and implemented in Matlab<sup>®</sup> and CST<sup>®</sup> in order to compare the results obtained with the proposed model and full-wave simulations. Furthermore, an analysis was carried out with WPT systems operating in the Industrial, Scientific, and Medical (ISM) radio frequency band of 13.56 MHz, with a bandwidth of 10 MHz. Also, it should be noted that the separation distance between the coils was fixed in 10 mm. For this simulation in CST<sup>®</sup>, the Frequency solver with adaptive meshing refinement at 13.56 MHz was used. Figure 4.1 presents the results obtained.

Figure 4.1 presents the results obtained by simulating a two-coil system for the following cases: Figure 4.1(a) 3-turn, Figure 4.1(b) 4-turn, Figure 4.1(c) 5-turn, Figure 4.1(d) 6-turn, and Figure 4.1(e) 7-turn configurations. As it can be observed, there is an increase in the difference  $\Delta$  between the results. Some hypotheses can be raised to justify such an increase: the first would be the error associated with the numerical method for solving the characteristic parameters of each coil expressed by (3.1) and (3.2): self-inductance, and characteristic resistance, respectively. Another hypothesis is the increase in insertion losses, which are not considered in the model. These losses cause the attenuation in signal strength that occurs when a signal is transmitted through a microstrip structure. The main one, in this case, is the dielectric losses. Finally, another hypothesis is the increased effect of the parasitic capacitance between the traces. Despite being low for the frequency band under analysis, it increases with the number of turns. However, these differences are not critical since the curves obtained in the two simulation conditions for all cases in the analysis have the same behavior.

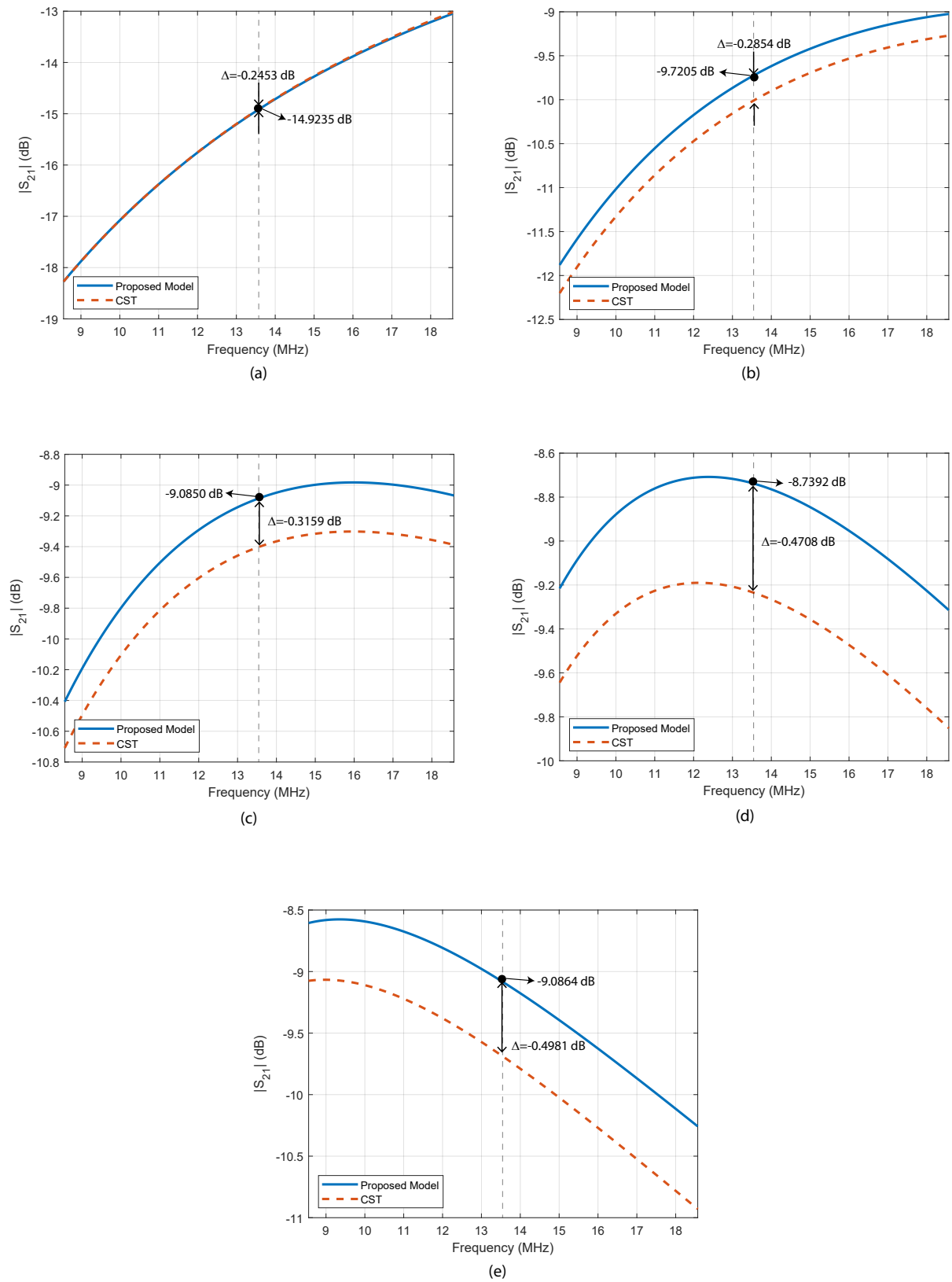


Figure 4.1 – Transmission coefficient values  $S_{21}$  for the two-coil systems described in Table 4.1: curves obtained by the proposed model and by simulation in the CST and the difference found in each case.

Another analysis that can be done based on the results in Figure 4.1 concerns the efficiency of the systems. It is possible to verify by the values of  $S_{21}$  obtained that the most efficient MCWPT system is the 6-turn configuration. It should be noted that the resonance frequency was not optimized in these cases; these analyses so far are focused on topology optimization. This behavior of the 6-turn system is due to the self-resonance of the system being approximately centered at 13.56 MHz. Therefore, it is possible to observe that the efficiency starts to decrease in the 7-turn condition. For a complete analysis of the efficiency, the relationships (2.16) and (2.5) were used to build Table 4.2, which compares the realized efficiency of the system with the maximum achievable values.

Table 4.2 – Power Transmission Efficiency (PTE) and maximum achievable efficiency ( $\eta_{MCWPT}^{max}$ ) values for two-coil MCWPT systems with different configurations.

Turns ( $n$ )	PTE (%)	$\eta_{MCWPT}^{max}$ (%)
3*	3.28	98.16
4	10.66	98.65
5	12.35	98.63
6	13.37	98.67
7	12.34	98.63

\* Optimized by resonance case, more details in the Section 4.2.

Table 4.2 shows that although the 6-turn system is the most efficient, all configurations have comparable values of maximum achievable efficiency  $\eta_{MCWPT}^{max}$ , which means that they have similar potential in transmitting energy. It can be justified once the mutual coupling between coils is similar, as the distance between coils is fixed. However, the input impedance changes as the number of turns increases, causing the variation in the realized efficiency. Therefore, to increase the efficiency  $PET$  and bring it closer to  $\eta_{MCWPT}^{max}$  it is necessary to optimize the impedance as discussed in the Section 2.4, reducing the mismatch losses. Another optimization variable would be the axial distance  $d_z$  that separates both coils. This variable is directly related to the mutual inductance between Tx and Rx, defining the magnetic coupling between them. Figure 4.2 shows the decay of the mutual inductance  $M_{sr}$  between a pair of 3-turn coils (as described in Table 4.1). As can be noticed, the coupling decreases exponentially as the distance between the coils increases. Similar behavior is also verified for efficiency. However, in more complex systems, as seen in the subsequent sections, it is necessary to consider other factors, such as the frequency splitting phenomenon verified in overcoupled resonant systems.

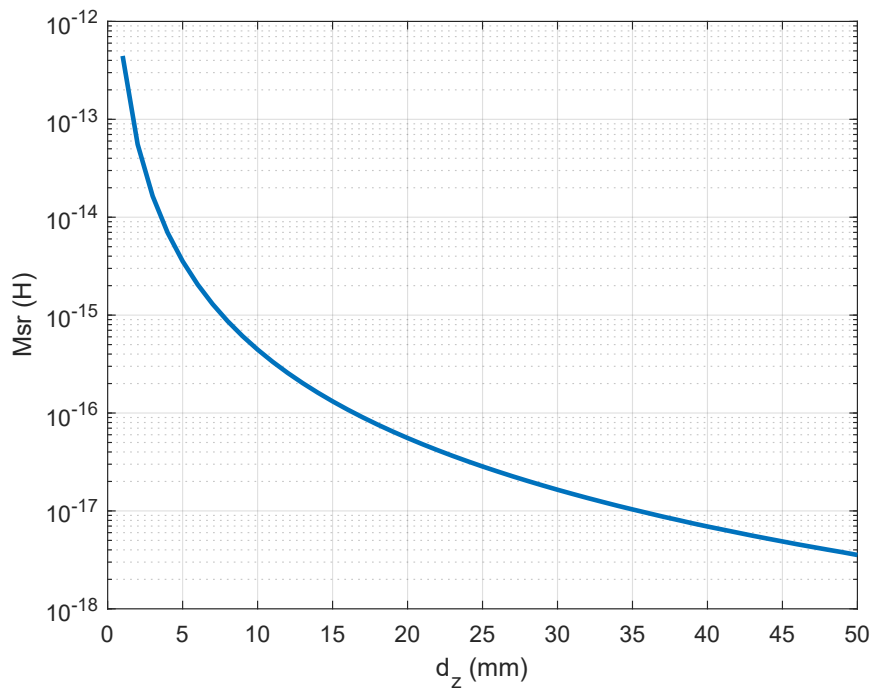


Figure 4.2 – Mutual inductance  $M_{sr}$  decay in a two-coil MCWPT system as the distance between the transmitting coil (Tx) and the receiving coil (Rx) increases.

## 4.2 Revalidation of the Proposed Circuit Model

A miniaturized MWPT system was designed, optimized, and prototyped with the same geometry described in Chapter 3. However, for this miniaturized version, the Tx, Rx coils, and the metamaterial cell have reduced dimensions and only three turns ( $n$ ). First, the dimensions of the metamaterial cell are optimized to achieve resonance at 13.56 MHz, a frequency in the ISM radio band. Thereby, the inductance of a 3-turn coil was calculated using (3.1) and its dimensions were optimized so that when connected to a lumped capacitance of  $(680 \pm 5\%)$  pF, it resonates at 13.56 MHz. For the coil optimization, the Frequency Domain solver on CST<sup>®</sup> was employed with adaptive mesh refinement at the resonant frequency to guarantee greater precision in the results.

An FR-4 substrate with double-faced copper layers was used for prototyping the system. In addition, a tin layer over the metalization was applied with the only objective of avoiding corrosion. Figure 4.3 presents the prototype and the arrangement of connectors and capacitors. The prototyped Rx and Tx coils are shown in Figure 4.4; the SMA Female Panel connector was used to feed the loop through the via and close the circuit as shown in the bottom layer part of Figure 4.4. The resonant surface in Figure 4.5 consists of four plates of  $5 \times 5$  cells, totaling a metasurface of  $10 \times 10$ . It was decided to carry out the study on a larger surface to verify the coupling sensitivity between Tx and Rx. It should also be noted that there is no resonance tuning circuit or lumped element in the Tx and Rx coils.

The electric parameters of this prototype were calculated with the proposed formulation



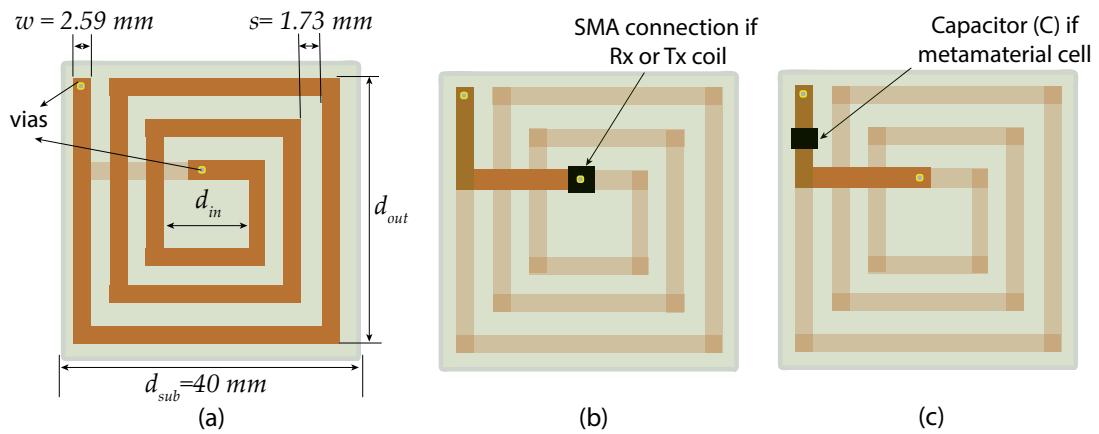


Figure 4.3 – Specification of the square printed coil geometry used in this work: (a) top layer, (b) bottom layer in case of Tx or Rx coils, and (c) bottom layer in case of metamaterial cells. The coils dimensions are:  $d_{out} = 32.5 \text{ mm}$ , and  $d_{in} = 10.08 \text{ mm}$ .

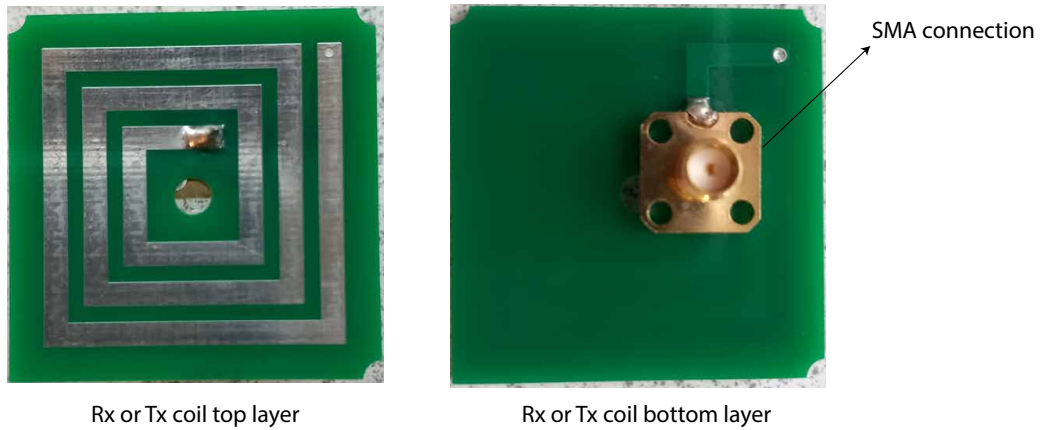


Figure 4.4 – Prototypes of the coils Rx and Tx designed for the MCWPT system.

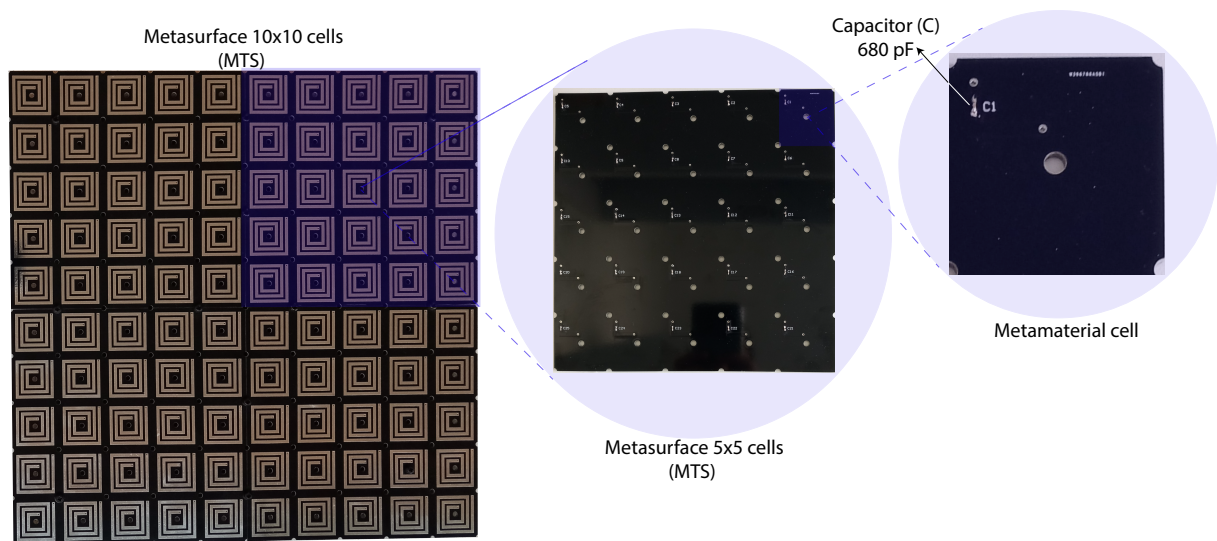


Figure 4.5 – Prototypes of the metasurface designed for the MCWPT system.

and validated based on comparison with measurements of the transmission coefficient using the nanoVNA vector network analyzer (setup in Section 4.3). The measured results are presented in Figure 4.6 and Figure 4.7 as a function of the frequency. For S-Parameter measurements, a probe is connected to the Tx coil and the second to the Rx coil, located on the metasurface in positions (1,1) and (1,3), respectively. As the capacitor used in this application has a higher tolerance (5%) than the one previously used in Chapter 3, a more significant frequency shift is expected when comparing the results simulated with the model and the measured values. Thus, Figure 4.6 shows this deviation range considering the lower and upper limits on the capacitance tolerance. Therefore, it is possible to verify that the measured values are within this variation range. It should also be noted that the values of  $Z_s$  and  $Z_L$  of the circuit model considered in this exploration were  $50 \Omega$  each.

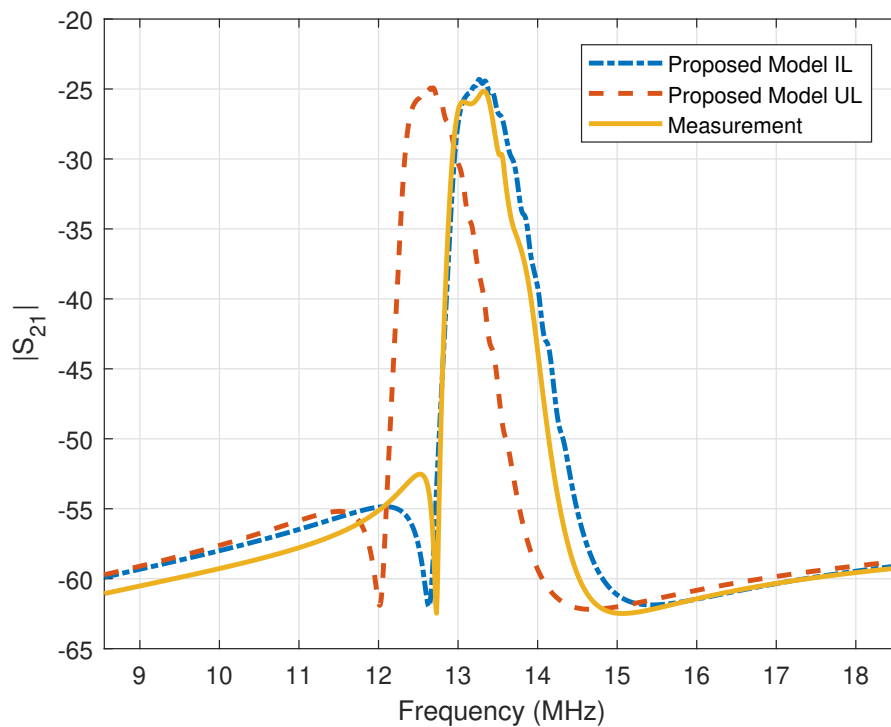


Figure 4.6 – Simulated and measurement  $S_{21}$  results considering the Inferior Limit (IL) and Upper Limit (UL) of capacitor with tolerance of 5%.

In contrast, Figure 4.6 presents the results obtained when considering the tolerance of the capacitor used in the resonant surface. In this case,  $C = 653 \text{ pF}$  was used, that is, a 4% of tolerance of the nominal value of the capacitance, and this value was reached by measuring 10 samples of used capacitors. It should also be noted that in the case of the revaluation, the resistance of the capacitor used in the metasurface was lower compared to the system used in Chapter 3, being only  $100 \text{ m}\Omega$ .

As can be noticed, both results shown in Figure 4.7 are in good agreement at lower frequencies. However, minor deviations can be caused by parasitic capacitances and insertion losses that are not considered in the circuit model but affect the measurement results. This fact

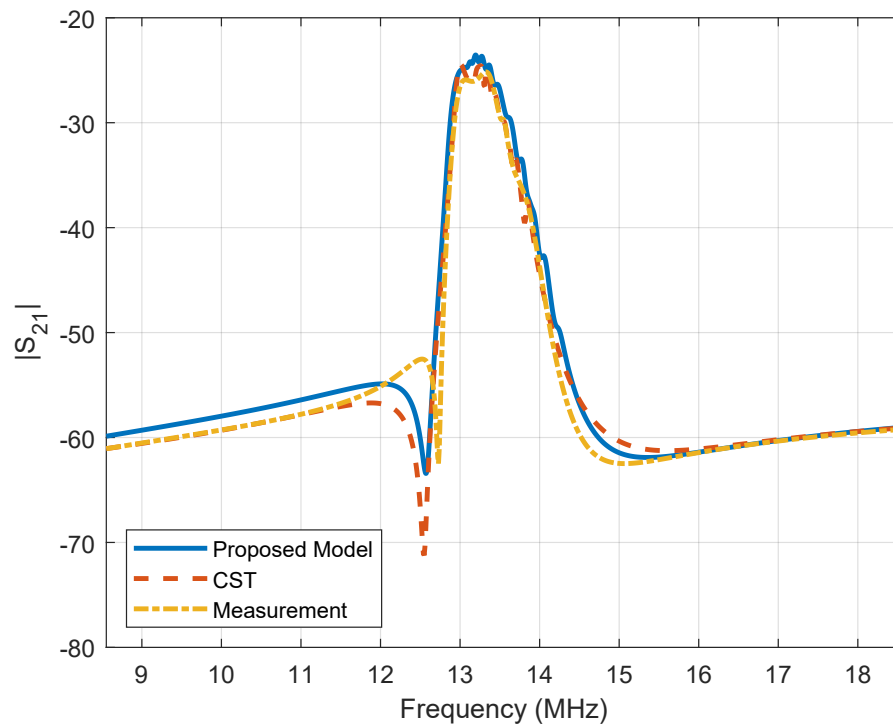


Figure 4.7 – Simulated, calculated, and measured  $S_{21}$  results considering a capacitance 4% bigger than its nominal value.

demonstrates that the proposed MCWPT analysis procedure has repeatability for a system with another configuration and operating in another frequency.

### 4.3 Measurement Setup Description

In order to analyze and compare the behavior of the designed MWPT system, the measurement setup schematized in Figure 4.8 was used. Before the measurements, however, the nanoVNA was calibrated at the ends of the cable using the Short-Open-Load-Thru (SOLT) standard. First, as shown in 4.8, the transmitter coil is connected to Port 1 and the receiver to Port 2 of the nanoVNA, which is connected to a computer. Then, through the nanoVNA interface installed on the computer, the matrix of scattering parameters is measured in a frequency range from 8.56 to 18.56 MHz, and this result is saved as a touchstone file (.s2p). This measurement is carried out by keeping the TX fixed in position (1,1) under the resonant surface at an axial distance of 5 mm and varying the position of the receiving coil on the metasurface at an axial length of 20 mm. In the case described in Section 4.2, the receiver was kept in position (3,1), as shown in Figure 4.8.

The measurement setup presented in Figure 4.8, makes it possible to evaluate the maximum achievable efficiency of an MCWPT system, to characterize the effective properties of the metamaterial, as well as to quantitatively analyze the influence of these structures in enhancing the efficiency of the MCWPT system. In addition, it is possible to evaluate the

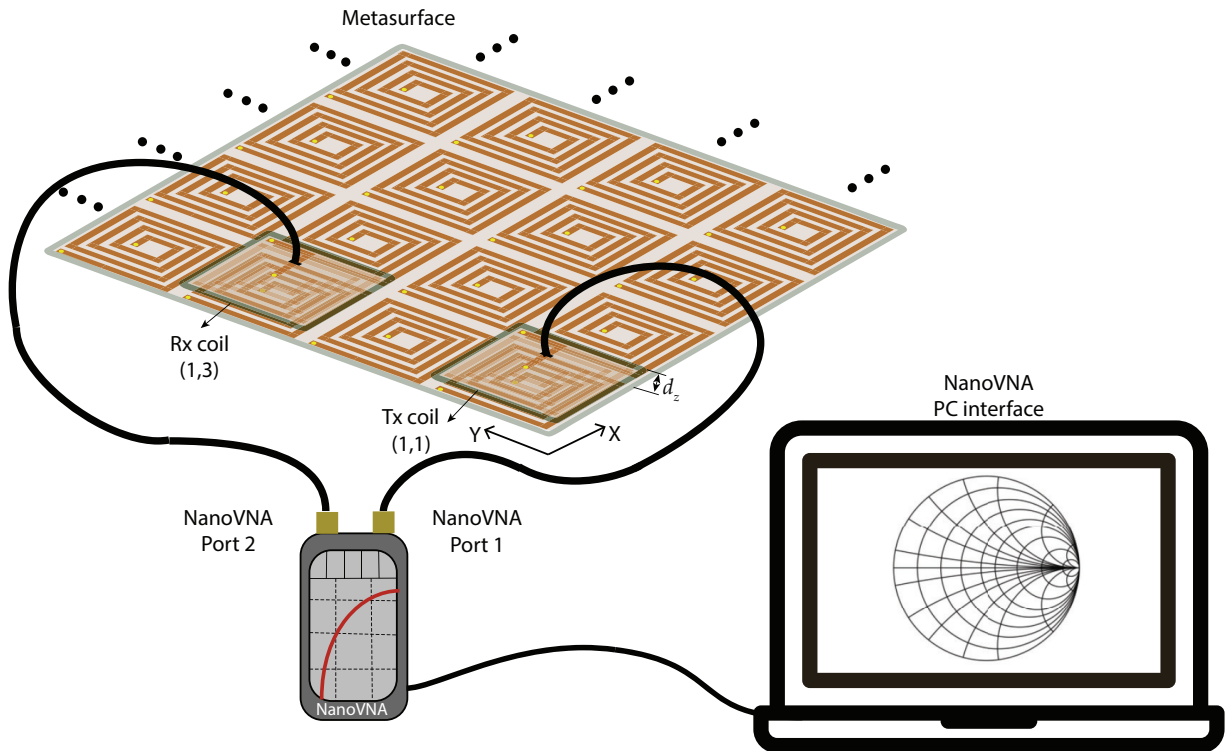


Figure 4.8 – Diagram for the experimental setup used in the transmission coefficient measurements.

impedance variation caused by a change in the receiver coil position. However, in this work, it was not possible to assess all these parameters since the system is very weakly coupled and works at the sensitivity limit of the measuring instruments, a fact that limited the experimental evaluations. An attempt was made to reduce the distance  $d_z$  that separates the Tx and Rx from the surface to  $5\text{ mm}$ , but it was not enough to carry out the measurements. In the subsequent section, the systems will be evaluated via simulation.

#### 4.4 Maximum Efficiency

In this proposed dynamic MCWPT system, it is possible to map the *PTE* as a function of the Rx position and to analyze the optimal frequency in each position. For this study, the circuit model described in Chapter 2 was considered with the Tx position remaining fixed in the first position (1,1), as shown in black in Figure 4.9. On the other side, the Rx was moved over different places on the surface. As a result, the *PTE* results are shown in Figure 4.9(a), whereas the optimal frequencies are shown in Figure 4.9(b).

Based on the results presented in Figure 4.9, it is possible to verify a shift in the optimal frequency with the change in the Rx position. This type of analysis is advantageous for designing and optimizing multi-channel systems; despite being a narrowband variation. Furthermore, optimizing the system can help increase the frequency band. In the case presented, the axial distance of the Tx and Rx coils concerning the surface is  $5\text{ mm}$ . Still, with the variation of this parameter, it is possible to change the point of the most excellent efficiency, as seen before, and

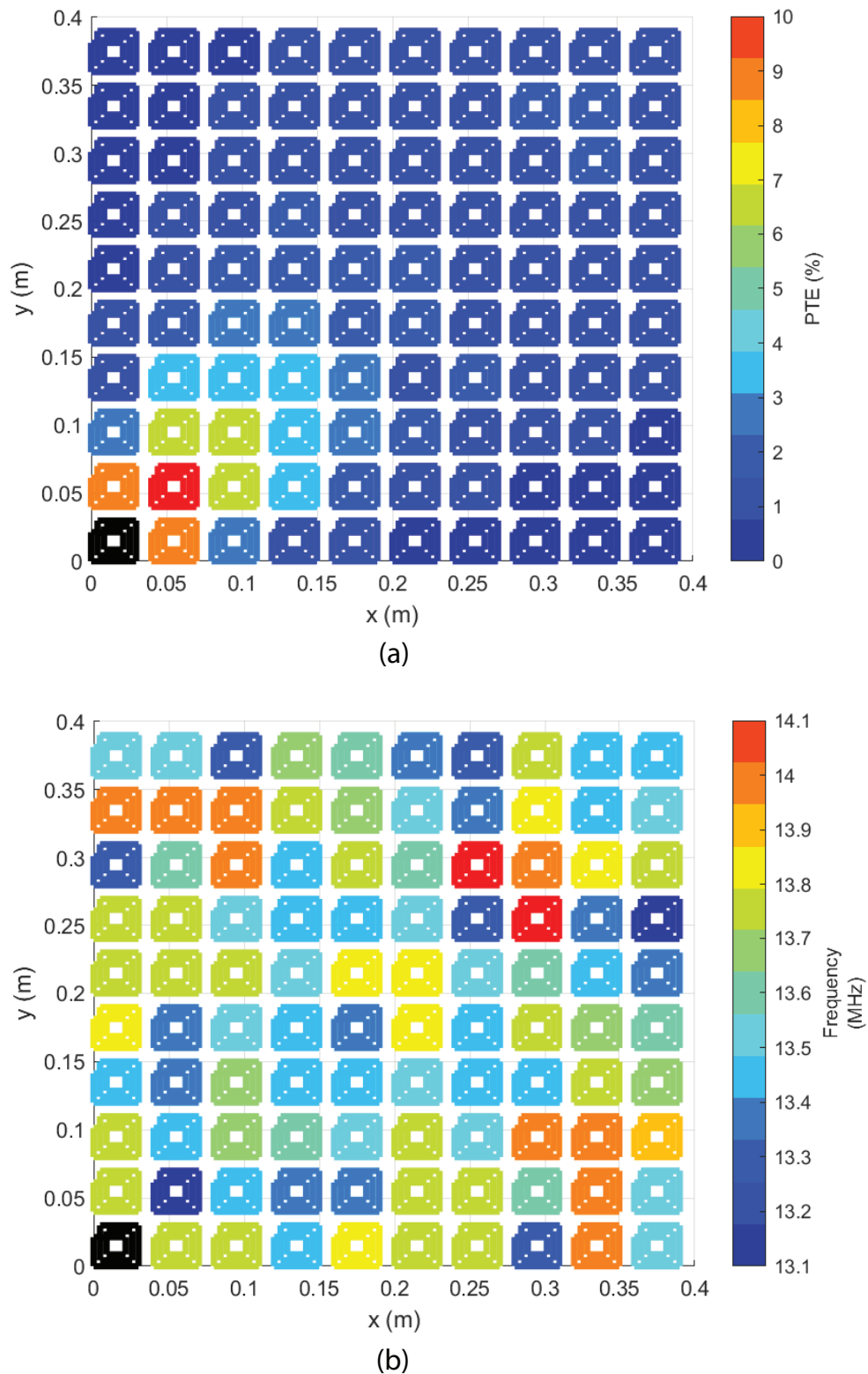


Figure 4.9 – *PTE* of the MCWPT system under analysis. The source coil is on the first cell of the resonant surface 10 x 10 cells while the position of the receiver varies over the other pads: (a) distribution of the maximum *PTE* in respect to the receiver position, (b) frequency where the maximum *PTE* occurs.

vary the frequency.

Another behavior verified in Figure 4.9 is that the results are practically symmetric with the position, reflecting the topology symmetries. However, as this work aims to present the potential of the circuit model method in analyzing several MIW applications, a design optimized for a specific application was not carried out. Still, some techniques to circumvent this symmetry can be used in practice, such as a re-configurable or non-symmetrical multilayer surface.

## 4.5 Variation in Source Current and in the Source Impedance

In a practical application, the receiver position in an MCWPT system can be tracked by measuring the input impedance of the system at a given frequency, which corresponds to the impedance seen by the detector source positioned on the array. In this case, a test signal is applied on the Tx, propagating across the resonant metasurface and being absorbed by the passive Rx. Many studies consider a magneto-inductive wave channel to be formed simply from a resonant circuit or a planar structure. However, this concept can also be extended to conformal magneto-inductive waveguides built with flexible substrates or with articulated elements (MISHRA; KIOURTI, 2021; SYMS et al., 2017). Consequently, depending on the application, different parameters can be tuned to improve the data channel performance. For example, simple 1-D structures can replace wired connections between devices (STEVENS et al., 2010). Conversely, 2-D structures provide a simple multiterminal channel to connect personal electronics (CHAIMOOL et al., 2021).

This work presents a method for designing and optimizing an MCWPT system with a resonant surface. This system can be used in various MIW applications; for example, 2-D structures can replace the Printed Circuit Board (PCB) in an electronic system. However, for such usability, the design should be optimized and well-designed for the function. Also, this technique can be implemented in silicon Integrated Circuits (ICs) to develop miniaturized systems that launch and detect magneto-inductive waves (STEVENS et al., 2010). Furthermore, multi-frequency structures with varying resonant frequencies can be combined to increase bandwidth (SANDOVAL et al., 2019).

A 2-D system composed of a resonant surface and two coplanar coils, transmitter, and receiver emulates a multiterminal channel MIW system in the application under study. Figure 4.10(a) shows the current variation in the source with the displacement of the receiver's position on the surface, as shown in Figure 4.10(b). The behavior observed in the Tx current curves for each case indicates a change in the impedance seen by the source. It is possible to verify the magnitude of this variation using (2.2). It should be noted that the coplanar Tx and Rx coils were considered at an axial distance of 5 mm from the metasurface; this distance was chosen to increase the magnetic coupling between the two coils and the resonant surface.

The curves shown in Figure 4.10(a) reveal the Tx current amplitude variation due to the displacement of the receiver. The behavior observed in the source current for each case indicates

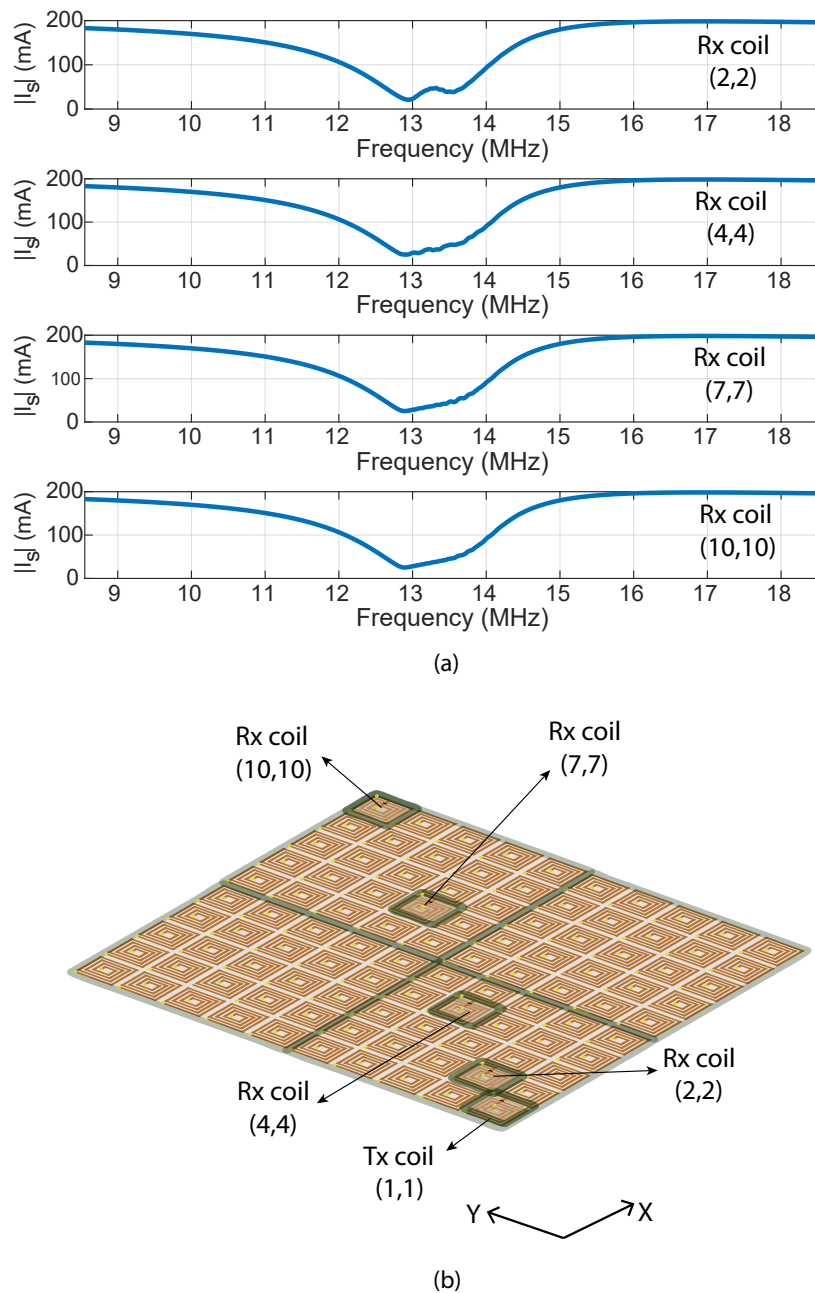


Figure 4.10 – Displacement of the receiver on the surface: (a) Tx current amplitude variation, and (b) the receiver position on the surface.

a change in impedance. However, the variation occurs more strongly in the vicinity of the Tx, which was already expected due to the weak coupling character between the loops of the MCWPT system under analysis. The behavior can be verified in Figure 4.11 and Figure 4.12, which show the source impedance variation in the impedance magnitude and the phase of this impedance, respectively.

The curves found for the impedance  $Z_{in}$  presented in Figure 4.11 and Figure 4.12 were obtained using (2.9), considering the system operating at the resonance frequency. However, as shown in Section 2.3.1, with (2.7), it is possible to model the impedance seen by the metamaterial

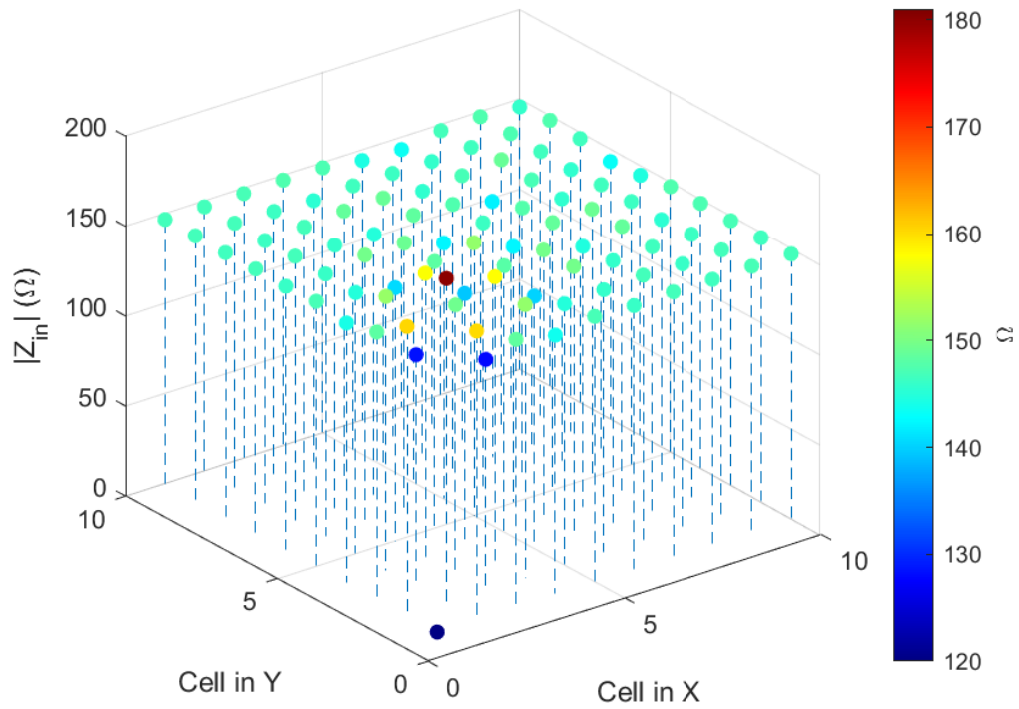


Figure 4.11 – Magnitude of the impedance seen by the source considering the receiver displacement over a metasurface with  $10 \times 10$  cells at  $f = 13.56$  MHz).

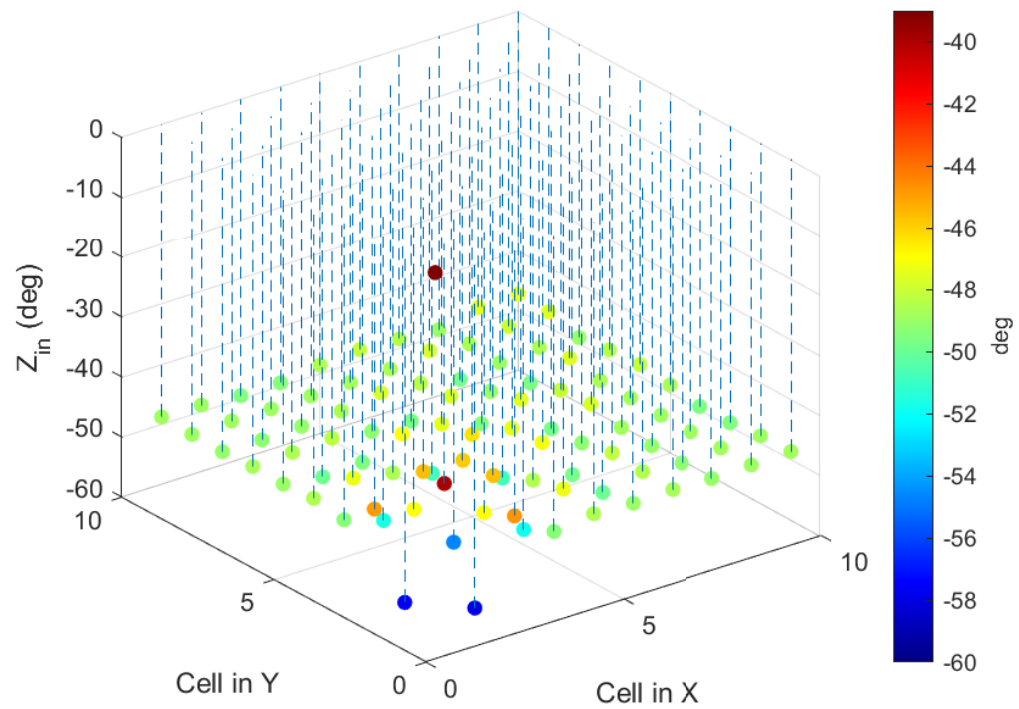


Figure 4.12 – Phase of the impedance seen by the source considering the receiver displacement over a metasurface with  $10 \times 10$  cells at  $f = 13.56$  MHz).



cell on which the receptor is positioned. And that in an impedance matching situation, the relations (2.7) and (2.9) would be the same. However, it should be noted that an out-of-matching case was used in this work, but the described circuit method could be used in a matching situation.

The impedance  $Z_{in}$  results presented in Figure 4.11 and Figure 4.12 were obtained using (2.9), considering the system operating at the resonant frequency  $13.56\text{ MHz}$ . However, as shown in Section 2.3.1, with (2.7), it is possible to model the impedance seen by the metamaterial cell on which the receptor is positioned. And in a case in which the impedance is perfectly matched, the relations (2.7) and (2.9) would be the same. However, it should be noted that the mismatched case considered in this work, but the described circuit method could be used in a matching situation.

The application shown in Figure 4.13 is useful in a dynamic wireless charging system since it allows not only the identification of the receiver position but also to focus of the transmitted power at the identification location. The hypothetical system presented in Figure 4.13 considers that the system consists of coils with 4 turns,  $Z_s = 50\ \Omega$ ,  $d_{in} = 1\text{ m}$ ,  $d_{out} = 1.80\text{ m}$ ,  $s = 10\text{ mm}$  separation between coplanar coils of  $10\text{ cm}$  and axial separation between receiver and surface coils of  $30\text{ cm}$ .

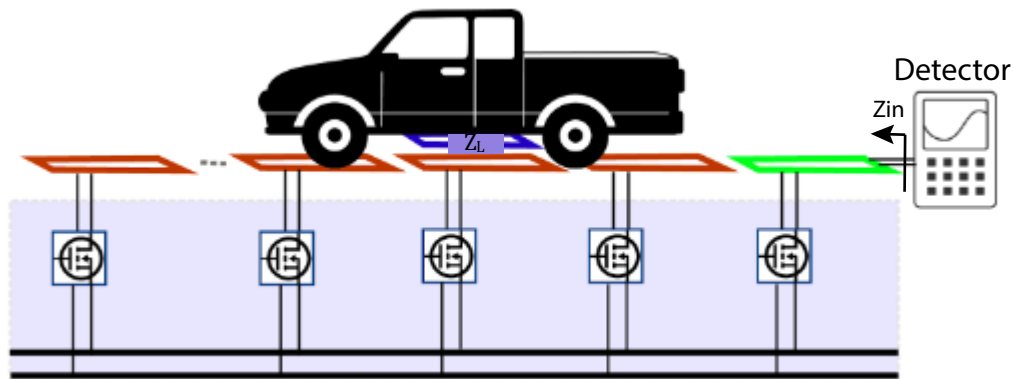


Figure 4.13 – Schematic of a dynamic MCWPT system. The detector block works as a signal transmitter, and it performs the impedance reading algorithm and the detection of the position of the device.

It is possible to verify in Figure 4.14 that the transmitter's input impedance  $Z_{in}$  changes with the variation of the receiver's position, which is also directly linked to the characteristics of the receiver's load  $Z_L$ . Some works, such as (SIMONAZZI; SANDROLINI; MARISCOTTI, 2022), use this strategy as an identification method. However, the method considers only the mutual inductance between the neighboring coils, whereas the method proposed here considers the interaction of all the coils of the system. Besides, this model is suitable for different WPT techniques, even though this work focuses on Inductive Coupling Technique (IPT).

Finally, it should be noted that all the characteristics shown in this section are directly dependent on the geometry of the structure and its operating frequency. In this way, a variation in frequency can increase or decrease the sensitivity of the source. It should also be noted that when using the MIW-based system, the detection frequency is generally different from the wireless powering frequency; this is done to avoid interference between the systems.

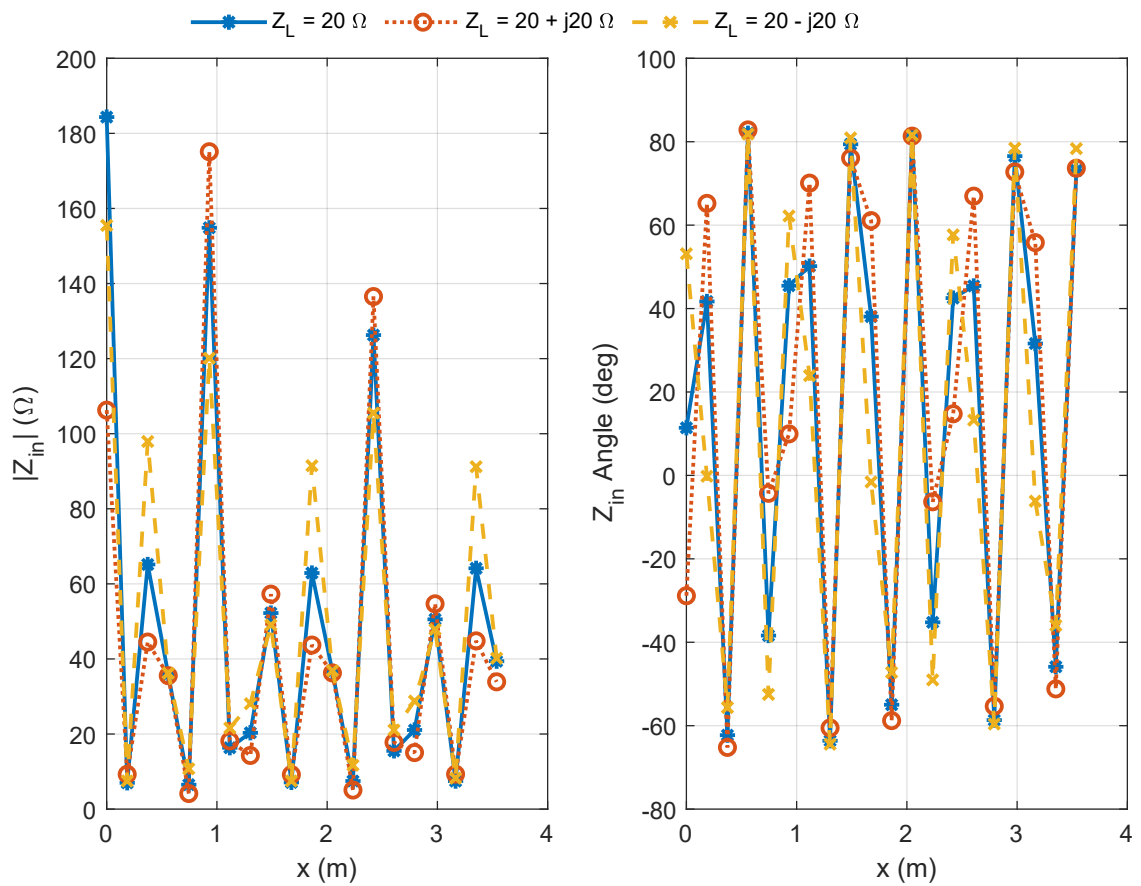


Figure 4.14 – Input impedance  $Z_{in}$  (magnitude and phase) seen by the detector block (Figure 4.13) as a function of the position of the receiver, considering different values for the receiver impedance  $Z_L$ .

## 4.6 Current Distribution Analysis on the Resonant Surface

Another helpful analysis that can be carried out with the proposed circuit model is related to the current distribution in the metamaterial cells. For example, in Figure 4.15, it is possible to verify the current distribution on the metamaterial with  $10 \times 10$  cells, being the Tx coil on the first cell and the Rx on the third coil at the diagonal, both at an axial distance of 5 mm from the plane. The frequency of 13.56 MHz was chosen to verify this distribution, which is within the system's operating band. Similarly, the current density analysis can also be carried out in full-wave simulation software such as CST<sup>®</sup>, as shown in Figure 4.16. However, in this case, the simulation takes about 7h41m, using a computer with an Intel<sup>®</sup> Xeon<sup>™</sup> W – 2275 processor, 256 GB RAM, and 3.30 GHz clock. Conversely, using the computational implementation of the proposed circuit model, the current evaluation is carried out in just 6.83 s, considering the same PC settings.

From visual inspection in Figure 4.15 and Figure 4.16, it is possible to verify a certain similarity between the results. However, the results from the full-wave simulation are more detailed once the current density is locally evaluated at each surface point, as shown in Figure 4.16. Contrarily, the circuit model method considers the current circulating in each cell of the

metasurface as constant; that is, the current is uniformly over the entire coil of the surface, as shown in Figure 4.15. Nevertheless, the results obtained by using the proposed model enable a straightforward and quick analysis of the current on the surface.

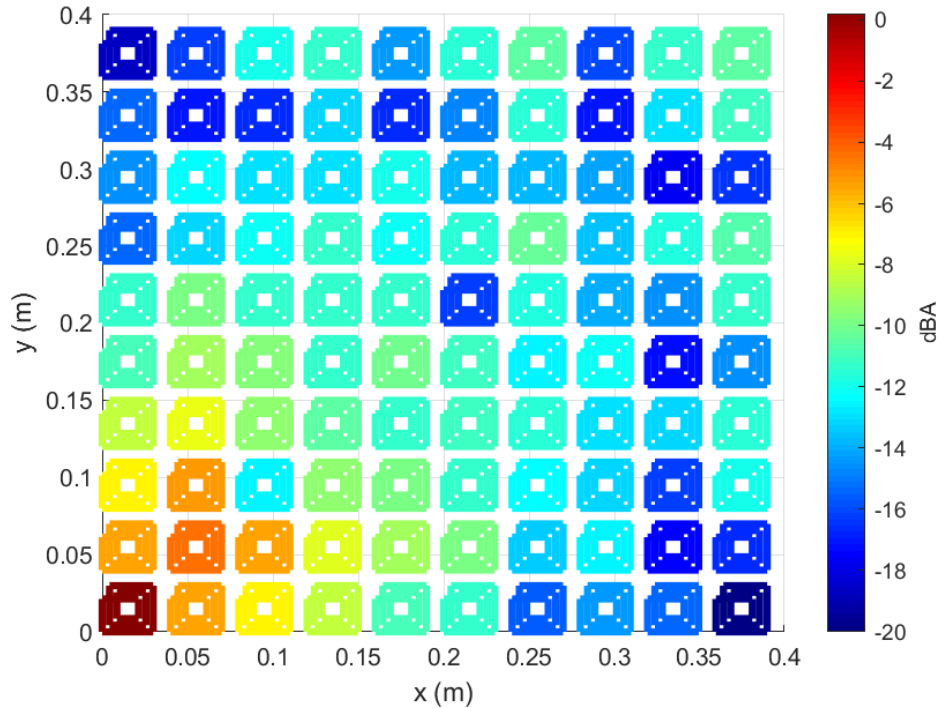


Figure 4.15 – The resonant surface solutions ( $10 \times 10$  cells,  $f = 13.56$  MHz) colors represent the cell the current modulus obtained with the complete circuit the model proposed.



Figure 4.16 – Current density obtained by simulation using *CST*<sup>®</sup> for the  $10 \times 10$  cells MCWPT system operating at  $f = 13.56$  MHz. The colors represent the density of the current obtained with the simulation.

Figure 4.17 shows the current distribution for two different frequencies, Figure 4.17(a) for the 13 MHz and Figure 4.17(b) to 14 MHz. It is possible to identify that the current path in the metamaterial is defined according to the positioning of the source coil. This path occurs diagonally to Tx for the cases under analysis presented in Figure 4.15 and Figure 4.15. The path is created due to the way currents are induced. If we analyze the first cell, for example, it has a higher current magnitude because it is directly coupled to Tx; that is, this cell has the most significant mutual inductance with the source. In turn, the first cell induces a current of the opposite sign in the two adjacent cells. However, these two cells have similar current magnitude and direction since the system is symmetric. Therefore, these cells also induce a current in their neighboring cell, and so on.

Another critical characteristic to observe in Figure 4.15 and Figure 4.17 is the current drop in the third cell of the diagonal for the three analyzed cases due to the presence of the receiver that is strongly coupled to this cell. Hence, a large part of the current contribution from the third cell goes to the receiving coil and, consequently, to the load connected to it. Notably, this behavior was observed in this work for a specific frequency. However, the magnitude and characteristics of the current distribution can change with changing frequency. Another feature that alters the current distribution behavior is the axial distance of Tx and Rx over the metasurface, as mentioned before in Section 4.1.

Finally, the current distribution on the metamaterial surface is directly linked to the characteristics of the load connected to the receiver. In addition, the system's sensitivity to the presence of this load is an essential factor to be taken into account so that the current reaches the receiver and is not lost in the metasurface. Therefore, optimizing the system impedance can increase efficiency and minimize losses on the resonant surface.

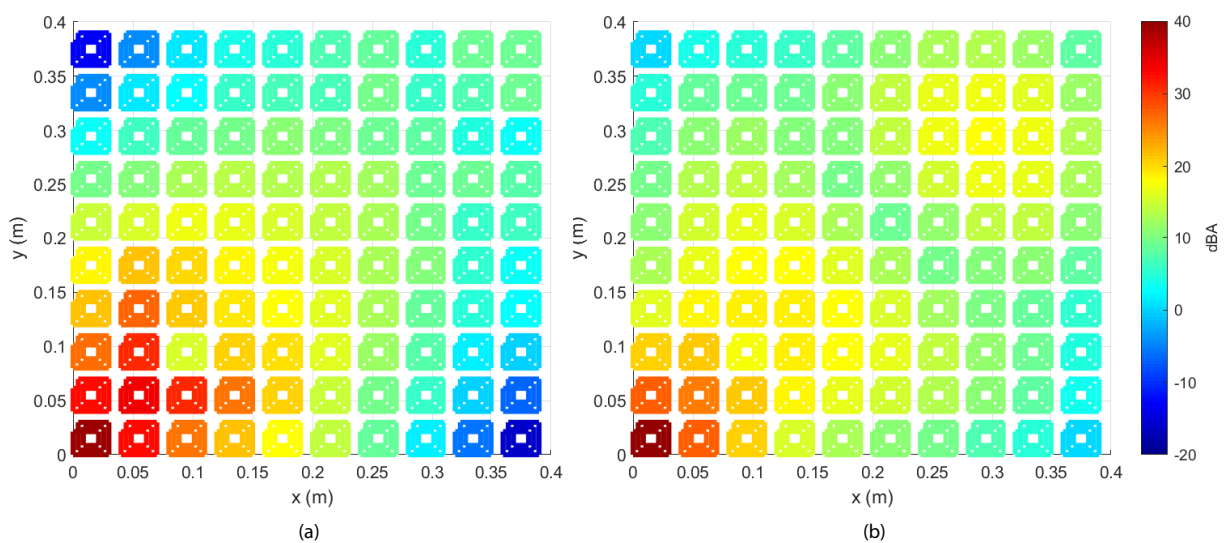


Figure 4.17 – The resonant surface solutions ( $10 \times 10$  cells) colors represent the cell the current modulus obtained with the complete circuit the model proposed: (a) operating in  $f = 13$  MHz, and (b) operating in  $f = 14$  MHz.

## 4.7 Impedance Optimization Analysis

To analyze an MCWPT system from the point of view of impedance optimization, we first consider a simple two-coil system with the topology shown in Section 4.2 and in Table 4.1. As shown in Table 4.1, a system with two coils of three turns and the topology under analysis can reach a maximum efficiency of about 98% when separated by an axial distance of 10 mm. However, as shown in Table 4.2, the system PTE is just over 3%. Thus, an LC-type topology was chosen for the Impedance Optimizer Circuit (IOC) as introduced in (SU et al., 2006), leaving the complete system with the configuration shown in Figure 4.18. The system has four meshes, and the system matrix that expresses the circuit model has been presented in (4.1). Here, an impedance optimization is performed in order to increase the efficiency of the MCWPT system under analysis.

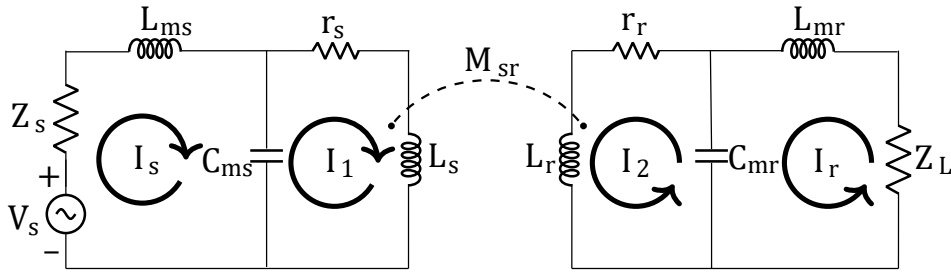


Figure 4.18 – Equivalent circuit for the two-coil MCWPT system structure with IOC.

$$\begin{bmatrix} V_s \\ 0 \\ 0 \\ 0 \end{bmatrix} = \begin{bmatrix} Z_s + j\omega L_{ms} - \frac{j}{\omega C_{ms}} & \frac{j}{\omega C_{ms}} & 0 & 0 \\ \frac{j}{\omega C_{ms}} & r_s + j\omega L_s & j\omega M_{sr} & 0 \\ 0 & j\omega M_{sr} & r_r + j\omega L_r & \frac{j}{\omega C_{mr}} \\ 0 & 0 & \frac{j}{\omega C_{ms}} & Z_L + j\omega L_{mr} - \frac{j}{\omega C_{mr}} \end{bmatrix} \cdot \begin{bmatrix} I_s \\ I_1 \\ I_2 \\ I_r \end{bmatrix} \quad (4.1)$$

The SPICE-based circuit simulation software, *KeysightADS*<sup>®</sup>, was used for the impedance optimization analysis for the system shown in Figure 4.18. The circuit that models the two coupled coils under the described conditions was implemented using this software. The values of the mutual inductance between the coils and their characteristic parameters, such as self-inductance and resistance shown in Table 4.1, were obtained using the methods proposed in Chapter 3. It should be noted that the values refer to the operating frequency of 13.56 MHz; this consideration is essential since the characteristic resistance is a frequency-dependent parameter. Figure 4.19 shows the complete system configuration, *i.e.*, the power supply model  $Z_s = 50 \Omega$ , IOC of the Tx part, model of the coupled coils of the system with  $M_{sr} = 60.02 \text{ nH}$ , IOC of the Rx part, and finally, the load  $Z_L = 50 \Omega$ . The rectifiers and converters were not considered in this analysis once they were out of the scope of this work. However, they could be inserted in CM through its SPICES parameters, probably changing the values of the IOC components or even being necessary to change the topology of this circuit.

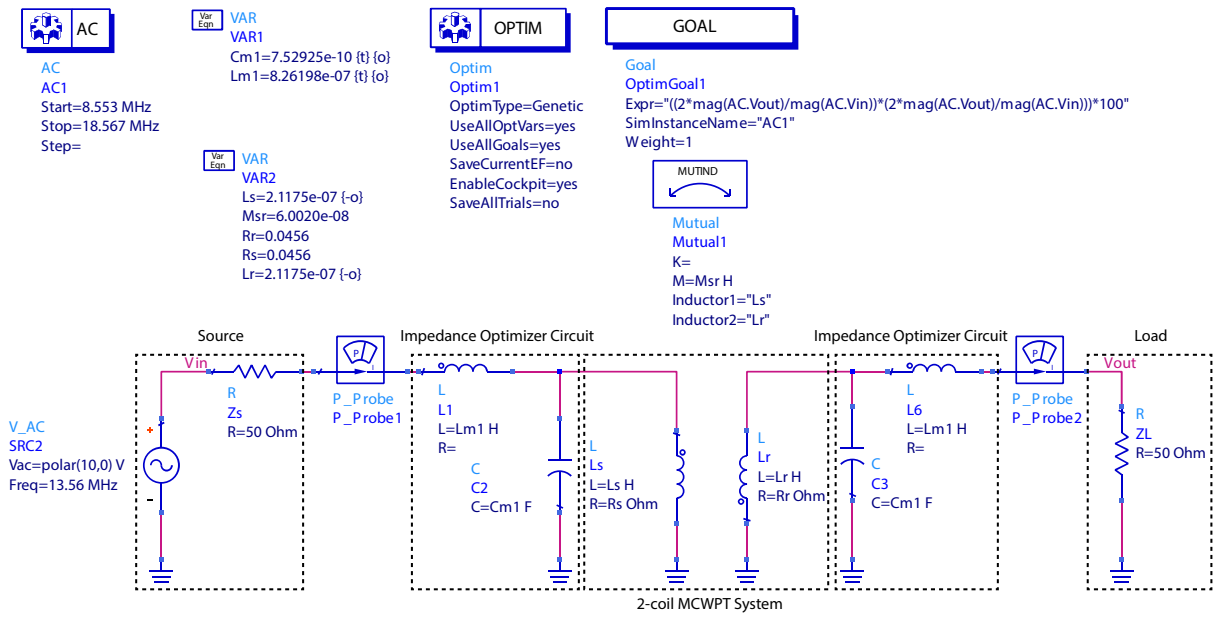


Figure 4.19 – Circuit for the two-coil MCWPT system structure with IOC simulated in ADS®.

As already mentioned, the IOCs in the case shown in Figure 4.19 have an LC-type topology. In this case, the optimization objective was reaching an efficiency around 98%, as estimated in Table 4.2. Thus, using the relation (2.16) and, the values of the inductor  $L_{m1}$  and the capacitor  $C_{m1}$  of the IOC-Tx and IOC-Rx were obtained. Hence, the system efficiency at 13.56 MHz when  $L_{m1} = 826.198 \text{ nH}$  and  $C_{m1} = 752.925 \text{ pF}$  was 98.08% very close to the predicted value. Figure 4.20 presents the curves obtained for the simulation of the circuit of Figure 4.16 in ADS® and for the same simulated circuit using the algorithm implemented in Matlab®. Even though the ADS simulation considers the characteristic resistance of the coils to be a fixed value of 13.56 MHz, the difference between the curves is very small. The fact that this variation is small is that for the analyzed frequency band, the characteristic resistance remains practically unchanged.

Impedance optimization can also be valuable for a more complex system. For example, consider the system illustrated in Figure 4.21. The system shown has a transmitting coil with an IOC and a  $4 \times 4$  metamaterial surface resonant at 13.56 MHz, a receiving coil with an IOC, and a load of  $Z_L = 50 \Omega$ . All coils are identical and have the physical characteristics presented in Section 4.2 and Table 4.1 to the three-turns coil. The receiver is located at position (4,4) of the metamaterial and the source at (1,1) as shown in Figure 4.21 both at a distance  $d_z = 5 \text{ mm}$ . It should be noted that the value of the capacitor used in the metamaterial cell is 680 pF without considering tolerance.

In the exploration presented in Figure 4.21, we chose to work with a smaller metamaterial, that is, with only  $4 \times 4$  cells. The choice was based on previous explorations that indicated the region close to the Tx as a region of more significant interaction between the system components. Another reason for choosing it is to show how the system's efficiency changes with the variation of the surface dimension. Finally, the topology chosen for the IOC used in the Tx and Rx parts

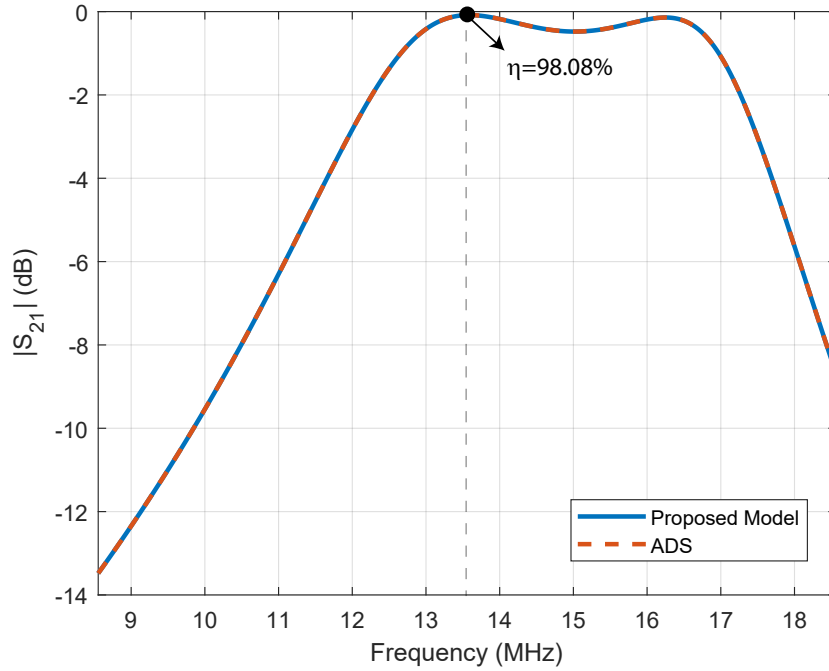


Figure 4.20 –  $S_{21}$  curves for the circuit shown in Figure 4.19 when simulated using the proposed model in *Matlab*<sup>®</sup> and *ADS*<sup>®</sup>.

was the T-LCC type, consisting of an inductor and two capacitors, as shown in Figure 4.21.

The matrix system that models the complete system is represented by (4.2), and it is obtained similarly to the one presented in Section 2.2.1. In this equation,  $M_s$  is the column vector of mutual inductance between the Tx coil and the cells of the metamaterial,  $M_r$  is the column vector of mutual inductance between the Rx coil and the cells of the metamaterial. The system was implemented in the proposed algorithm with values of  $L_{ms} = 1.69 \mu H$ ,  $C_{ms} = 34.40 pF$ ,  $C_s = 918.72 nF$ ,  $L_{mr} = 1.78 \mu H$ ,  $C_{mr} = 40.11 pF$ , and  $C_r = 965.58 nF$ . These values were obtained by a simulation in the software *ADS*<sup>®</sup> (more details on this type of simulation in F).

$$\begin{bmatrix} V_s \\ 0 \\ 0 \\ 0 \\ 0 \end{bmatrix} = \begin{bmatrix} Z_s + j\omega L_{ms} - \frac{j}{\omega C_{ms}} & \frac{j}{\omega C_{ms}} & 0 & 0 & 0 \\ \frac{j}{\omega C_{ms}} & r_s + j\omega L_s + \frac{j}{\omega C_s} + j\omega M'_s & j\omega M_{sr} & 0 & 0 \\ 0 & j\omega M_s & j\omega M & j\omega M_r & 0 \\ 0 & 0 & j\omega M_{sr} & j\omega M'_r r_r + j\omega L_r + \frac{j}{\omega C_r} & \frac{j}{\omega C_{mr}} \\ 0 & 0 & 0 & \frac{j}{\omega C_{ms}} & Z_L + j\omega L_{mr} - \frac{j}{\omega C_{mr}} \end{bmatrix} \cdot \begin{bmatrix} I_s \\ I_x \\ I_M \\ I_y \\ I_r \end{bmatrix} \quad (4.2)$$

The MCWPT system without the IOC in the Tx and Rx part had an efficiency of 37.1%, a much higher value than those obtained for the receiver in the same position on a surface of  $10 \times 10$  cells. This shows that reducing current leakage increases system efficiency. However, with the insertion of the IOCs, the efficiency went to 47.8%; that is, there was an increase of more than 10%. This fact proves the importance of optimizing the impedance of the MCWPT system to enhance efficiency.

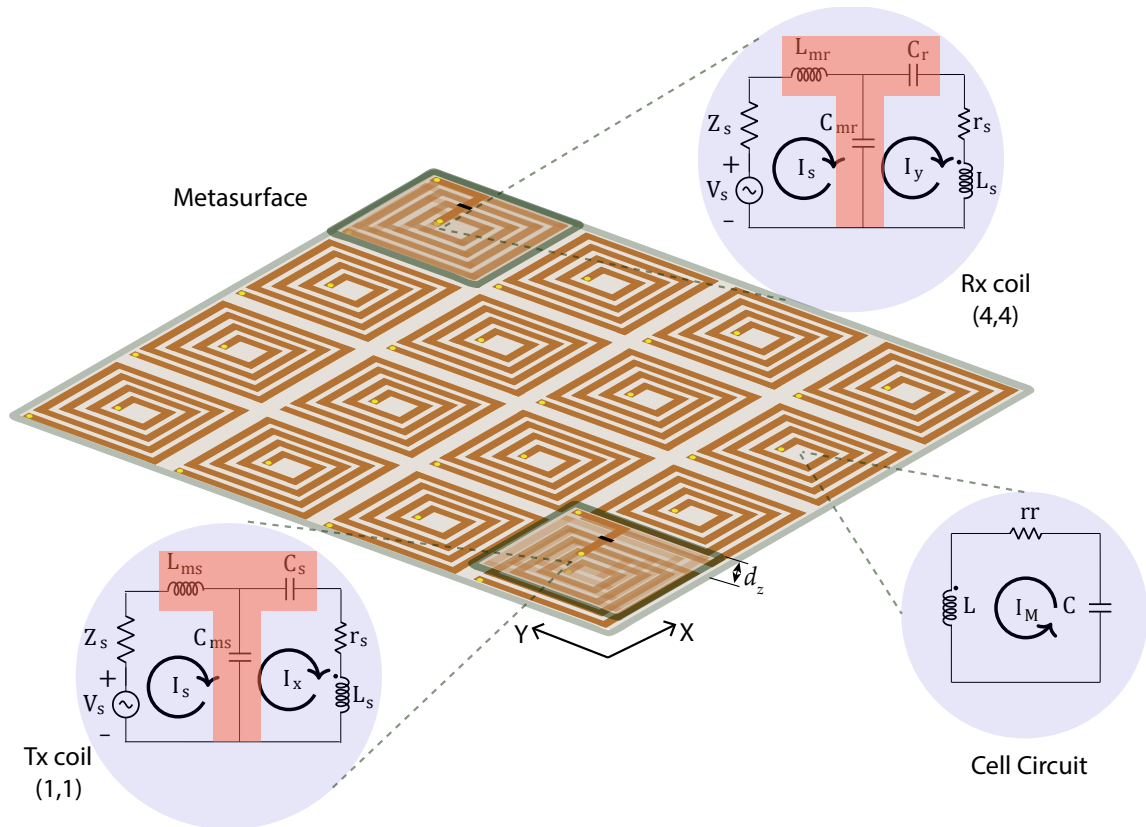


Figure 4.21 – MCWPT system scheme considers the circuit of the Tx element, the circuit of the receiver part, and the circuit model of each cell of the resonant surface.

## 4.8 Partial Conclusions

In this chapter, the analysis of the MCWPT systems based on the metamaterials operation principle is discussed, as well as how these structures enhance the efficiency of these systems. First, the optimization variables of a microstrip-printed MCWPT system were explored. It was verified how important it is to have a clear optimization objective and how the constructive characteristics of the loops can influence a two-coil MCPWT system. Subsequently, a revalidation of the circuit model presented in Chapter 3 was presented, but now with a smaller and more loosely coupled system. With the results obtained, it was possible to revalidate the proposed method and verify how difficult it is in practice to perform measurements with loosely coupled systems due to the sensitivity limit being very low.

Other analyzes were carried out with the objective of evaluating the parameters of an MCWPT system. Explorations were carried out for a frequency analysis on how the parameters: Frequency and position of the receiver over the source on the surface of the metamaterial influence the energy transmission efficiency of the system. The chapter also analyzed how the variation of the source impedance and the current flow on the surface of the metamaterial with the variation of the receiver position and the charge rate on the resonant surface is important in an MCWPT analysis. For this, the MIW theory (Magneto-Inductive Waves) is used in an application: Passive Position Tracking in Dynamic MCWPT Systems as seen in Section 4.5.



# 5 Final Considerations

## 5.1 Conclusions

The main objective of this work is to propose a circuit model to reduce the computational cost of analyzing complete MCWPT systems. Hence, as a starting point, this work aims to theoretically, computationally, and experimentally explore the characteristics of MCWPT systems of small dimensions, built-on microstrip structures, and loosely coupled. For this, a 3-D MIW device design was presented using a wireless power transfer system in which the receiving device can be supplied with power over a resonant charging surface. In addition, methodologies for analyzing and enhancing the efficiency of these devices are evaluated.

First, the circuit formulation of a generic MCWPT system studied was approached. Then the mathematical formulations based on circuit theory are necessary for calculating currents in the coils. Formulations for efficiency analysis and calculation of the impedance seen by the source were also discussed. Subsequently, mathematical formulations were carried out to calculate the circuit parameters of the MCWPT system, such as the self-inductance and characteristic resistance of the coils; in the sequence, the modeling for the calculation of the mutual inductance between the loops was approached.

With the models proposed for the study, they were validated. For this purpose, an experimental system composed of Tx and Rx coils and a resonant surface built-in FR4 was built. As shown in Table 3.2, measurements of own inductance and characteristic resistance were then carried out. The results corroborated with the modeling having a deviation of 8% in the case of self-inductance; it was corrected in the final model.

To validate the model for calculating the mutual inductance, firstly, a comparison was made between the mathematical simplification used to solve the integration of the problem with the Gaussian quadrature method widely used in integration problems. The results presented in Table 3.3 show that the proposed simplification has a much lower computational cost, and both ways lead to very close values. Next, the *CST*<sup>®</sup> software was used to validate the geometric model used to model the loops. As a result, and as shown in Figure 3.5, the proposed geometric simplification is valid since there is a low field concentration in the region disregarded in the model. Subsequently, the measurements of the mutual inductance were carried out considering three arrangements between two coils, as shown in Table 3.4. Again, the calculated and measured results are very close, demonstrating that the method for calculating the coils' mutual inductance is suitable.

Some explorations were carried out after having validated the models. The first was static, which calculated the mutual inductance between the cells of a  $10 \times 10$  metamaterial. The model proved to be efficient, taking only 0.778 s to calculate. Figure 3.6 shows the coupling between

the metasurface loops taking the first cell as a reference. The result makes it possible to evaluate the interaction between the first cell and the others. Subsequently, a frequency analysis was performed using the generic prototype. As a result, it was possible to evaluate the behavior of the simulated system with the measurements, and the results again corroborated with the proposed models, as shown in Figure 3.8 and Figure 3.9.

In Chapter 4, some analyses were carried out concerning the system optimization variables to increase the efficiency of an MCWPT system. Revalidation of the proposed model was carried out, and from the results obtained, it was possible to verify the conformity of the method in analyzing MCWPT systems in the frequency range of some  $MHz$ . Furthermore, the source impedance variation was evaluated in the case of a variation of the receiver position on the resonant surface. As a result, it was possible to verify one of the main characteristics of energy transfer systems in the near field, which is the influence of the receiver on the source impedance. The proposed method has a significant difference compared to the equations in the literature, which is the study of cases where there is an impedance mismatch in the system since the models present in the literature consider perfectly matched systems. Moreover, it was possible to map the relative positions between the source and receiver to study the frequency behavior of transmission efficiency, as shown in Section 4.4.

Verifying current dispersion in the metamaterial allows the analysis of the magnetic field of the MCWPT system. However, this type of analysis in full-wave software demands a high computational cost, making it often unfeasible. The proposed modeling proved to be a good alternative for this type of analysis, as shown in Section 4.6. Finally, another possibility of study is the influence of the receiver on current dispersion and the importance of optimizing the impedance of the constituent parts of an MCWPT system to increase efficiency.

The most original conclusion is that, with all the explorations addressed, it is clear that with the exact modeling and characterization approach presented, it can be applied to other 3-D MCWPT devices that use MIW. Furthermore, the way to calculate the mutual inductance between the coils can be obtained directly with the integration calculation using some other type of numerical method. This way, the proposed circuit model is not restricted to the MCWPT system studied, and the coil geometry or its spatial configuration may vary. Furthermore, the analysis can be extended to large resonant surfaces with correct optimization or parallel computing.

## 5.2 Future Works and Perspectives

Based on the conclusion of this work, some future results can be carried out to improve the formulations and explorations carried out; they are:

- Perform the optimization and prototype of a complete MCWPT system with a purely passive impedance optimizer circuit;

- Perform the optimization and prototyping of a complete MCWPT system with a purely active impedance optimizer circuit;
- Implement an algorithm with the proposed circuit model applied to curved structures in order to carry out practical explorations and applications in the context of MCWPT systems;
- Further, explore the potential of receiver identification in dynamic WPT systems. Perform explorations with multiple receivers and use some identification methods such as Time-Reversal;
- Perform the optimization of a multilayer system and verify the accuracy of the proposed model in this condition;
- Perform system validation and explorations with other coil geometries and different sizes since all investigations carried out in this work were considered equal loops;
- Perform applications with a reconfigurable surface in order to better explore the characteristics of MIWs in MCWPT systems.

### 5.3 Publications and Complementary Activities

In developing the research work, some papers were accepted and presented at scientific and journal conferences. These works are listed below:

- F. M. Freitas et al., "Circuit Model for Fast Computational Analysis of RWPT Applications," 2022 IEEE 20th Biennial Conference on Electromagnetic Field Computation (CEFC), Denver, CO, USA, 2022, pp. 1-2, doi: 10.1109/CEFC55061.2022.9940841. **Published.**
- F. M. Freitas et al., "Numerical Evaluation of Circuit Model for Fast Computational Analysis of Resonant Wireless Power Transfer System," in IEEE Transactions on Magnetics, doi: 10.1109/TMAG.2022.3231366. **Published.**
- F. M. Freitas et al., "Applications of Magnetoinductive Waves for Receiver-Coil Location in WPT system: Circuit Model for 1D Analysis," 2022 IEEE 67th Annual Conference on Magnetism and Magnetic Materials (MMM 2022), Minneapolis, MN, USA. **Accepted but not presented.**

Furthermore, activities were carried out in partnership with international laboratories, which resulted in future publications:

- Internship at Laboratoire Ampère (École Centrale de Lyon - Écully - France) February 2022 to July 2022.

- Internship at L'Institut d'Electronique et des Technologies du numéRique (IETR) (Université de Rennes - Rennes - France) August 2022 to December 2022.

# Bibliography

- ALMEIDA, J. V. de; FEITOZA, R. S. Metamaterial-enhanced magnetic coupling: An inductive wireless power transmission system assisted by metamaterial-based  $\mu$ -negative lenses. **IEEE Microwave Magazine**, v. 19, p. 95–100, 2018. Cited in page 23.
- BALANIS, C. A. **Advanced engineering electromagnetics**. [S.l.]: John Wiley & sons, 2012. Cited in page 26.
- BALANIS, C. A. **Antenna theory: analysis and design**. [S.l.]: John Wiley & sons, 2015. Cited in page 42.
- BASIR, A.; YOO, H. Efficient wireless power transfer system with a miniaturized quad-band implantable antenna for deep-body multitasking implants. **IEEE Transactions on Microwave Theory and Techniques**, v. 68, n. 5, p. 1943–1953, 2020. Cited in page 24.
- BROWN, W. C. The history of the development of the rectenna. **NASA. Johnson Space Center Solar Power Satellite Microwave Transmission and Reception**, 1980. Cited in page 16.
- CALIÒ, R. et al. Piezoelectric energy harvesting solutions. **Sensors**, Mdpi, v. 14, n. 3, p. 4755–4790, 2014. Cited in page 23.
- CAMPIONE, S.; MESA, F.; CAPOLINO, F. Magnetoinductive waves and complex modes in two-dimensional periodic arrays of split ring resonators. **IEEE Transactions on Antennas and Propagation**, v. 61, n. 7, p. 3554–3563, 2013. Cited in page 29.
- CHAIMOOL, S. et al. **A Defected Metasurface for Field-Localizing Wireless Power Transfer**. [S.l.]: IntechOpen, 2021. Cited in page 61.
- CHAN, C. W.; STEVENSY, C. J. Two-dimensional magneto-inductive wave data structures. In: **IEEE. Proceedings of the 5th European Conference on Antennas and Propagation (EUCAP)**. [S.l.], 2011. p. 1071–1075. Cited in page 32.
- CHEN, W.-C. et al. A multi-channel passive brain implant for wireless neuropotential monitoring. **IEEE Journal of Electromagnetics, RF and Microwaves in Medicine and Biology**, v. 2, n. 4, p. 262–269, 2018. Cited in page 22.
- DAI, J.; LUDOIS, D. C. A survey of wireless power transfer and a critical comparison of inductive and capacitive coupling for small gap applications. **IEEE Transactions on Power Electronics**, v. 30, n. 11, p. 6017–6029, 2015. Cited 2 times in pages 24 and 35.
- DANG, X. et al. Self-tuning multi-transmitter wireless power transfer to freely positioned receivers. **IEEE Access**, v. 8, p. 119940–119950, 2020. Cited in page 25.
- DAS, R.; YOO, H. A multiband antenna associating wireless monitoring and nonleaky wireless power transfer system for biomedical implants. **IEEE Transactions on Microwave Theory and Techniques**, v. 65, n. 7, p. 2485–2495, 2017. Cited in page 22.
- DURAND, E. **Magnétostatique**. [S.l.]: Elsevier Masson, 1968. Cited in page 42.

EDN. **A new calculation for designing multilayer planar spiral inductors**. 2010. Disponível em: <<https://www.edn.com/a-new-calculation-for-designing-multilayer-planar-spiral-inductors/>><https://www.edn.com/a-new-calculation-for-designing-multilayer-planar-spiral-inductors/>. Cited in page 38.

FARIA, A. et al. A Fast and Precise Tool for Multi-Layer Planar Coil Self-Inductance Calculation. **Sensors**, v. 21, n. 14, p. 4864, jan. 2021. ISSN 1424-8220. Number: 14 Publisher: Multidisciplinary Digital Publishing Institute. Disponível em: <<https://www.mdpi.com/1424-8220/21/14/4864>><https://www.mdpi.com/1424-8220/21/14/4864>. Cited in page 38.

FREITAS, F. M. et al. Numerical evaluation of circuit model for fast computational analysis of resonant wireless power transfer system. **IEEE Transactions on Magnetics**, p. 1–1, 2022. Cited in page 37.

FREITAS, F. M. et al. Circuit model for fast computational analysis of rwpt applications. In: **2022 IEEE 20th Biennial Conference on Electromagnetic Field Computation (CEFC)**. [S.l.: s.n.], 2022. p. 1–2. Cited in page 37.

GUO, Z.-H.; DONG, S.-E. Receiver power allocation and transmitter power control analysis for multiple-receiver wireless power transfer systems. **Journal of Electronic Science and Technology**, Elsevier, v. 17, n. 4, p. 100009, 2019. Cited in page 34.

HO, J. S.; KIM, S.; POON, A. S. Y. Midfield wireless powering for implantable systems. **Proceedings of the IEEE**, v. 101, n. 6, p. 1369–1378, 2013. Cited in page 23.

HUI, D.; YISHENG, Z.; BAISHAN, Z. Research on the electromagnetic radiation of a PCB planar inductor. In: **2005 Asia-Pacific Microwave Conference Proceedings**. [S.l.: s.n.], 2005. v. 1, p. 3 pp.–. ISSN: 2165-4743. Cited in page 39.

KHAN, S. R. et al. Wireless power transfer techniques for implantable medical devices: A review. **Sensors**, MDPI, v. 20, n. 12, p. 3487, 2020. Cited in page 17.

KIM, T.-H. et al. Highly efficient wpt system with negative impedance converter for q-factor improvement. **IEEE Access**, v. 7, p. 108750–108760, 2019. Cited 2 times in pages 25 and 35.

KRÄHENBÜHL, L. et al. Large surface lc-resonant metamaterials: From circuit model to modal theory and efficient numerical methods. **IEEE Transactions on Magnetics**, v. 56, p. 1–4, 2020. Cited in page 50.

KUHN, W.; IBRAHIM, N. Analysis of current crowding effects in multiturn spiral inductors. **IEEE Transactions on Microwave Theory and Techniques**, v. 49, n. 1, p. 31–38, jan. 2001. ISSN 1557-9670. Conference Name: IEEE Transactions on Microwave Theory and Techniques. Cited in page 39.

KURS, A. et al. Wireless power transfer via strongly coupled magnetic resonances. **science**, American Association for the Advancement of Science, v. 317, n. 5834, p. 83–86, 2007. Cited in page 16.

LEE, S. B.; KIM, M.; JANG, I. G. Determination of the optimal resonant condition for multireceiver wireless power transfer systems considering the transfer efficiency and different rated powers with altered coupling effects. **IEEE Journal of Emerging and Selected Topics in Power Electronics**, v. 9, n. 2, p. 2384–2393, 2021. Cited in page 25.

LESKARAC, D. et al. Pev charging technologies and v2g on distributed systems and utility interfaces. **Vehicle-to-Grid: Linking Electric Vehicles to the Smart Grid**, London, United Kingdom: The Institution of Electrical Engineers, v. 79, p. 157–209, 2015. Cited in page 16.

LIN, R. et al. Wireless battery-free body sensor networks using near-field-enabled clothing. **Nature communications**, Nature Publishing Group UK London, v. 11, n. 1, p. 444, 2020. Cited 2 times in pages 17 and 19.

LORRAIN, P.; CORSON, D. R. **Electromagnetic fields and waves**. [S.l.]: W. H. Freeman, 1970. Cited in page 39.

MAO, S. et al. A polygonal double-layer coil design for high-efficiency wireless power transfer. **AIP Advances**, v. 8, n. 5, p. 056631, maio 2018. Publisher: American Institute of Physics. Disponível em: <<https://aip.scitation.org/doi/10.1063/1.5007259>><https://aip.scitation.org/doi/10.1063/1.5007259>. Cited in page 37.

MENG, M.; KIANI, M. Design and optimization of ultrasonic wireless power transmission links for millimeter-sized biomedical implants. **IEEE Transactions on Biomedical Circuits and Systems**, v. 11, n. 1, p. 98–107, 2017. Cited in page 23.

MISHRA, V.; KIOURTI, A. Wearable planar magnetoinductive waveguide wbans: Bending around anatomical curvatures. In: **2021 IEEE International Symposium on Antennas and Propagation and USNC-URSI Radio Science Meeting (APS/URSI)**. [S.l.: s.n.], 2021. p. 1039–1040. Cited in page 61.

MOHAN, S. et al. Simple accurate expressions for planar spiral inductances. **IEEE Journal of Solid-State Circuits**, v. 34, n. 10, p. 1419–1424, out. 1999. ISSN 1558-173X. Conference Name: IEEE Journal of Solid-State Circuits. Cited in page 38.

NEJADPAK, A. et al. Design of planar inductor based Z-source inverter for residential alternate energy sources. In: **2011 Twenty-Sixth Annual IEEE Applied Power Electronics Conference and Exposition (APEC)**. [S.l.: s.n.], 2011. p. 1698–1703. ISSN: 1048-2334. Cited in page 38.

NISHIMURA, S. I. et al. Enhancing the inductive coupling and efficiency of wireless power transmission system by using metamaterials. In: **MOMAG**. Curitiba, Brazil: [s.n.], 2014. p. 121–125. Disponível em: <<https://hal.archives-ouvertes.fr/hal-01064690>><https://hal.archives-ouvertes.fr/hal-01064690>. Cited 2 times in pages 38 and 39.

PATIL, V. L.; PATIL, V. L. Marconi's exploitation of em-waves. **Chronological Developments of Wireless Radio Systems before World War II**, Springer, p. 33–47, 2021. Cited in page 16.

PELEKANIDIS, A. G. et al. Wireless power transfer via negative permittivity metamaterials as resonating elements. In: **2017 International Applied Computational Electromagnetics Society Symposium - Italy (ACES)**. [S.l.: s.n.], 2017. p. 1–2. Cited in page 23.

PENDRY, J. B. Negative refraction makes a perfect lens. **Phys. Rev. Lett.**, v. 85, p. 3966–3969, 2000. Cited in page 23.

POZAR, D. **Microwave Engineering Fourth Edition.(2011)**. [S.l.]: Wiley and Sons, 2011. Cited in page 33.

RAKLUEA, C. et al. True nulls-free magnetoinductive waveguides using alternate coupling polarities for batteryless dynamic wireless power transfer applications. **IEEE Transactions on Power Electronics**, v. 37, n. 8, p. 8835–8854, 2022. Cited in page 18.

RAO<sup>1</sup>, T. C.; GEETHA, K. Categories, standards and recent trends in wireless power transfer: A survey. **Indian journal of science and technology**, v. 9, p. 20, 2016. Cited in page 17.

SANDOVAL, F. S. et al. A 2-D Magnetoinductive Wave Device for Freer Wireless Power Transfer. **IEEE Transactions on Power Electronics**, v. 34, n. 11, p. 10433–10445, nov. 2019. ISSN 1941-0107. Conference Name: IEEE Transactions on Power Electronics. Cited 2 times in pages 29 and 61.

SANDOVAL, F. S.; MOAZENZADEH, A.; WALLRABE, U. Comprehensive modeling of magnetoinductive wave devices for wireless power transfer. **IEEE Transactions on Power Electronics**, v. 33, p. 8905–8915, 2018. Cited in page 26.

SHAMONINA, E. et al. Magnetoinductive waves in one, two, and three dimensions. **Journal of Applied Physics**, American Institute of Physics, v. 92, n. 10, p. 6252–6261, 2002. Cited in page 32.

SHAN, D. et al. Wireless power transfer system with enhanced efficiency by using frequency reconfigurable metamaterial. **Scientific Reports**, v. 12, p. 1–11, 2022. Cited in page 23.

SIMONAZZI, M.; SANDROLINI, L.; MARISCOTTI, A. Receiver-Coil Location Detection in a Dynamic Wireless Power Transfer System for Electric Vehicle Charging. **Sensors (Basel, Switzerland)**, v. 22, n. 6, p. 2317, mar. 2022. ISSN 1424-8220. Cited 2 times in pages 29 and 64.

SOARES, I.; RESENDE, U. Radially periodic metasurface lenses for magnetic field collimation in resonant wireless power transfer applications. **Journal of Microwaves, Optoelectronics and Electromagnetic Applications**, v. 21, p. 48–60, 2022. Cited in page 23.

SOARES, **Analysis of Resonant Wireless Power Transfer Systems with Magnetic Metasurface Lenses**. Tese (Doutorado) — Centro Federal de Educação Tecnológica de Minas Gerais, Belo Horizonte - MG, Brazil, 2020. Disponível em: <<https://drive.google.com/file/d/1ZtHDKIdk6ngUmbMF7-ZjiYvoHF7j7jWq/view?usp=sharing>><https://drive.google.com/file/d/1ZtHDKIdk6ngUmbMF7-ZjiYvoHF7j7jWq/view?usp=sharing>. Cited in page 28.

SOLYMAR, L.; SHAMONINA, E. **Waves in metamaterials**. Oxford ; New York: Oxford University Press, 2009. OCLC: ocn245558989. ISBN 978-0-19-921533-1. Cited in page 29.

SONG, M.; BELOV, P.; KAPITANOVA, P. Wireless power transfer inspired by the modern trends in electromagnetics. **Applied physics reviews**, AIP Publishing LLC, v. 4, n. 2, p. 021102, 2017. Cited in page 32.

STEVENS, C. J. A magneto-inductive wave wireless power transfer device. **Wireless Power Transfer**, Cambridge University Press, v. 2, n. 1, p. 51–59, 2015. Cited in page 31.

STEVENS, C. J. Magnetoinductive waves and wireless power transfer. **IEEE Transactions on Power Electronics**, v. 30, p. 6182–6190, 2015. Cited in page 29.

STEVENS, C. J. et al. Magnetic metamaterials as 1-d data transfer channels: An application for magneto-inductive waves. **IEEE Transactions on Microwave Theory and Techniques**, v. 58, p. 1248–1256, 2010. Cited in page 61.

SU, Y. et al. Research of lcl resonant inverter in wireless power transfer system. In: **2006 International Conference on Power System Technology**. [S.l.: s.n.], 2006. p. 1–6. Cited 2 times in pages 25 and 68.



SYMS, R. R. A. et al. Metamaterial magnetic resonance imaging endoscope. In: **2017 11th International Congress on Engineered Materials Platforms for Novel Wave Phenomena (Metamaterials)**. [S.l.: s.n.], 2017. p. 337–339. Cited in page 61.

TESLA, N. **My Inventions: Nikola Tesla's Autobiography**. [S.l.]: e-artnow, 2021. Cited in page 16.

TIAN, L. et al. High misalignment tolerance in efficiency of wpt system with movable intermediate coil and adjustable frequency. **IEEE Access**, v. 9, p. 139527–139535, 2021. Cited in page 25.

TRIVIÑO, A.; GONZÁLEZ-GONZÁLEZ, J. M.; AGUADO, J. A. Wireless power transfer technologies applied to electric vehicles: A review. **Energies**, MDPI, v. 14, n. 6, p. 1547, 2021. Cited in page 18.

UMAY, I.; FIDAN, B.; BARSHAN, B. Localization and tracking of implantable biomedical sensors. **Sensors**, MDPI, v. 17, n. 3, p. 583, 2017. Cited in page 19.

YASIR, M.; HAQUE, M. S. The witricity: Revolution in power transmission technology. **International Journal of Scientific & Engineering Research**, v. 4, n. 8, p. 565–570, 2013. Cited in page 17.

ZHANG, Y. Transfer Efficiency Analysis. In: ZHANG, Y. (Ed.). **Key Technologies of Magnetically-Coupled Resonant Wireless Power Transfer**. Singapore: Springer, 2018, (Springer Theses). p. 23–38. ISBN 978-981-10-6538-5. Disponível em: <[https://doi.org/10.1007/978-981-10-6538-5\\_2](https://doi.org/10.1007/978-981-10-6538-5_2)>[https://doi.org/10.1007/978-981-10-6538-5\\_2](https://doi.org/10.1007/978-981-10-6538-5_2). Cited 2 times in pages 28 and 31.

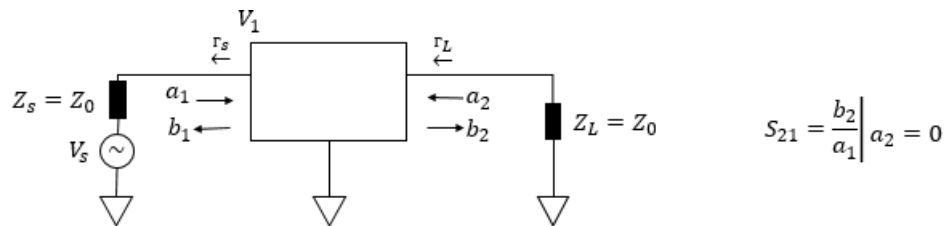
ZHANG, Y.; ZHAO, Z. Frequency Splitting Analysis of Two-Coil Resonant Wireless Power Transfer. **IEEE Antennas and Wireless Propagation Letters**, v. 13, p. 400–402, 2014. ISSN 1548-5757. Conference Name: IEEE Antennas and Wireless Propagation Letters. Cited in page 30.

ZHOU, L.; SHEN, Z. Hybrid frequency-selective raserber with low-frequency diffusion and high-frequency absorption. **IEEE Transactions on Antennas and Propagation**, v. 69, n. 3, p. 1469–1476, 2021. Cited in page 30.

# Appendix

# APPENDIX A – Finding Parameter $S_{21}$

The direct transmission coefficient can be found:



What is  $a_1$  in this case?

We know that:  $a_1 = \frac{V_1^+}{\sqrt{Z_0}}$ , and  $V_1^+ = \frac{V_s}{2}$  (Voltage Divider)  $\rightarrow a_1 = \frac{V_s}{2\sqrt{Z_0}}$

Considering the load:  $b_2 = \frac{V_L}{\sqrt{Z_0}}$  Why?  $\rightarrow$   $a_2 = r_L b_2$

But,  $r_L = 0$  because  $Z_L = Z_0$ , so  $a_2 = 0$

$$V_L = V_1^+ + V_1^- = a_2 \cdot \sqrt{Z_0} + b_2 \cdot \sqrt{Z_0} \xrightarrow{a_2=0} V_L = b_2 \cdot \sqrt{Z_0}$$

Now find  $V_L/V_s$ :

$$V_L = b_2 \cdot \sqrt{Z_0} = (S_{21}a_1 + S_{22}a_2) \cdot \sqrt{Z_0} \xrightarrow{a_2=0} V_L = S_{21}a_1 \cdot \sqrt{Z_0}$$

$\Downarrow$  Substitute  $a_1 = \frac{V_s}{2\sqrt{Z_0}}$

$$S_{21} = \frac{2V_L}{V_s} \sqrt{\frac{Z_s}{Z_L}} \xrightarrow{Z_s=Z_L} \boxed{S_{21} = \frac{2V_L}{V_s}}$$

The validation of this formulation was performed in the *Keysight ADS* software.

# APPENDIX B – Radiation Resistance of a Loop Antenna

STEP 1: Calculate the Electric and Magnetic field of a loop antenna:

$$\text{Magnetic field: } \vec{H} = \left( \frac{\pi I_0 \sin\theta}{r} \cdot \frac{A}{\lambda^2} \right) \hat{a}_\theta$$

$$\text{Electric field: } E_\phi = \eta H_\theta$$

STEP 2: Calculate the Average Power Density  $\vec{W}_{avg}$ :

$$\vec{W}_{avg} = \frac{1}{2} \cdot \text{Re} \left( \vec{E} \times \vec{H} \right)$$

$$\vec{W}_{avg} = \frac{1}{2} \cdot \text{Re} \left( E_\phi \hat{a}_\phi \times H_\theta \hat{a}_\theta \right)$$

$$\vec{W}_{avg} = \frac{1}{2} \cdot \text{Re} \left( E_\phi \cdot H_\theta \hat{a}_r \right)$$

$$\text{How } E_\phi = \eta H_\theta, \text{ then: } \vec{W}_{avg} = \frac{1}{2} \cdot H_\theta^2 \hat{a}_r$$

STEP 3: Calculate Radiated Power:

$$P_{rad} = \int \vec{W}_{avg} \, d\vec{s}$$

$$P_{rad} = \int_{\theta=0}^{\pi} \int_{\phi=0}^{2\pi} \frac{1}{2} \cdot \eta H_\theta^2 (r^2 \cdot \sin\theta) \, d\theta d\phi$$

$$P_{rad} = \int_{\theta=0}^{\pi} \int_{\phi=0}^{2\pi} \frac{1}{2} \cdot (120\pi) \left( \frac{\pi^2 \cdot I_0^2 \cdot \sin^2\theta}{r^2} \right) (r^2 \cdot \sin\theta) \, d\theta d\phi$$

$$P_{rad} = \int_0^{2\pi} \int_{\theta=0}^{\pi} 60\pi^3 \cdot I_0^2 \cdot \frac{A^2}{\lambda^4} \cdot \sin^3\theta \, d\theta$$

$$P_{rad} = 120\pi^4 \cdot I_0^2 \cdot \frac{A^2}{\lambda^4} \int_{\theta=0}^{\pi} \sin^3\theta \, d\theta$$

$$P_{rad} = 160\pi^4 \cdot I_0^2 \cdot \frac{A^2}{\lambda^4}$$

STEP 4: Compare the equation from step 3 with  $P_{rad} = \frac{1}{2} \cdot I_0^2 \cdot R_{rad}$

$$\frac{1}{2} \cdot I_0^2 \cdot R_{rad} = 160\pi^4 \cdot I_0^2 \cdot \frac{A^2}{\lambda^4}$$

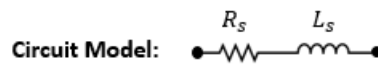
$$R_{rad} = 320 \cdot \pi^4 \cdot \frac{A^2}{\lambda^4}$$

As in this work, the coil is square with a side equal to  $d_{out}$ , then:

$$R_{rad} = 320 \cdot \pi^4 \cdot \frac{d_{out}^2}{\lambda^4} = R_{ac}$$

# APPENDIX C – Measurement Setup of the Characteristic Parameters of Coil

The coil's characteristic parameters were measured using a precision impedance meter using the series  $RL$  circuit model with a frequency range from 1 to 30  $MHz$ . The instrument used in the measurements is shown below:

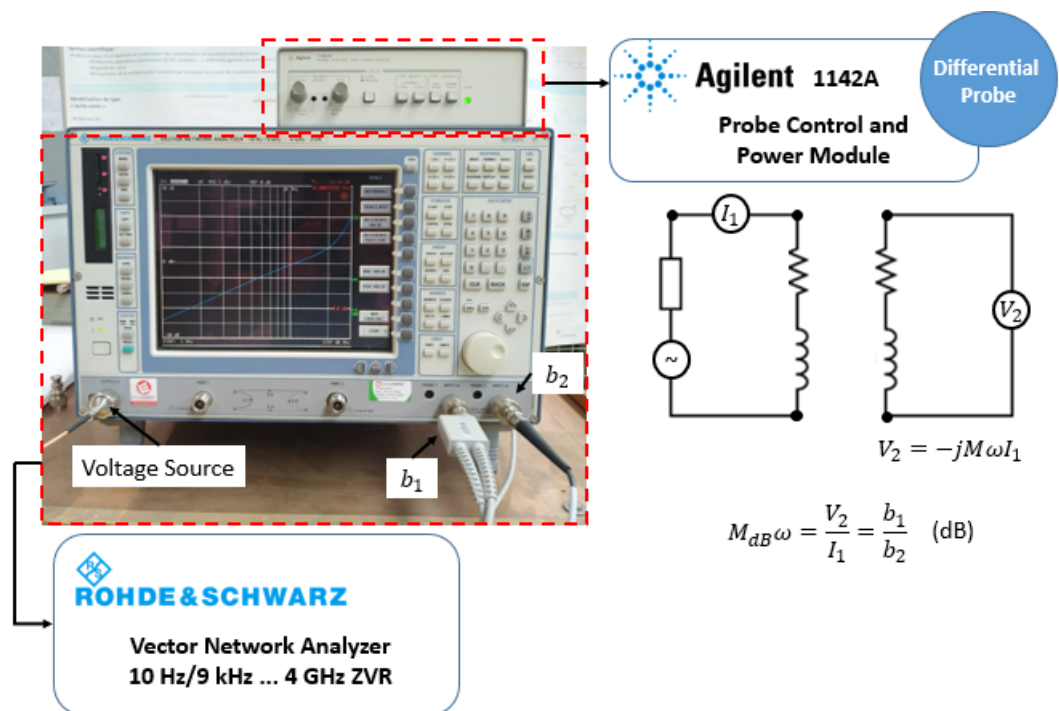


Range frequency: 1 ~ 30  $MHz$

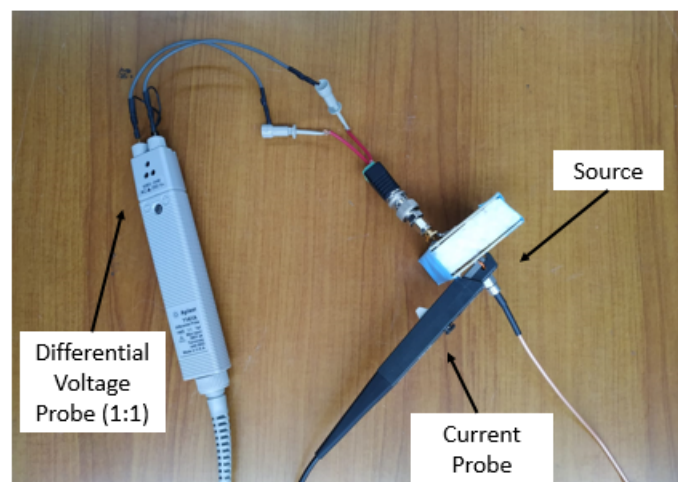
NOTE: You need to calibrate the instrument to take measurements.

# APPENDIX D – Measurement Setup of the Mutual Inductance

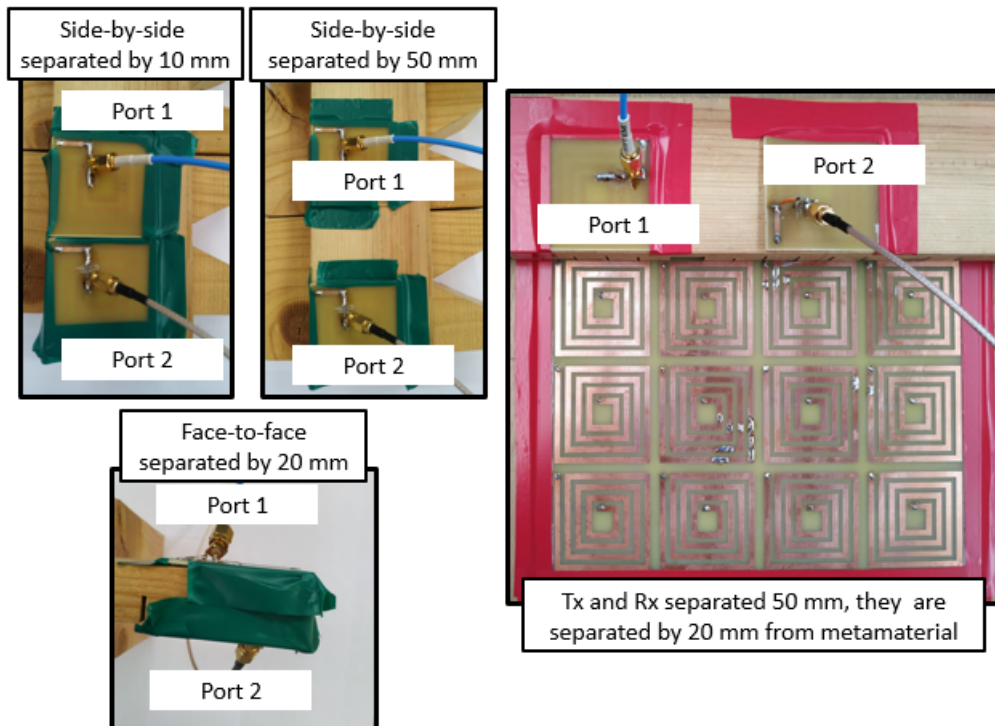
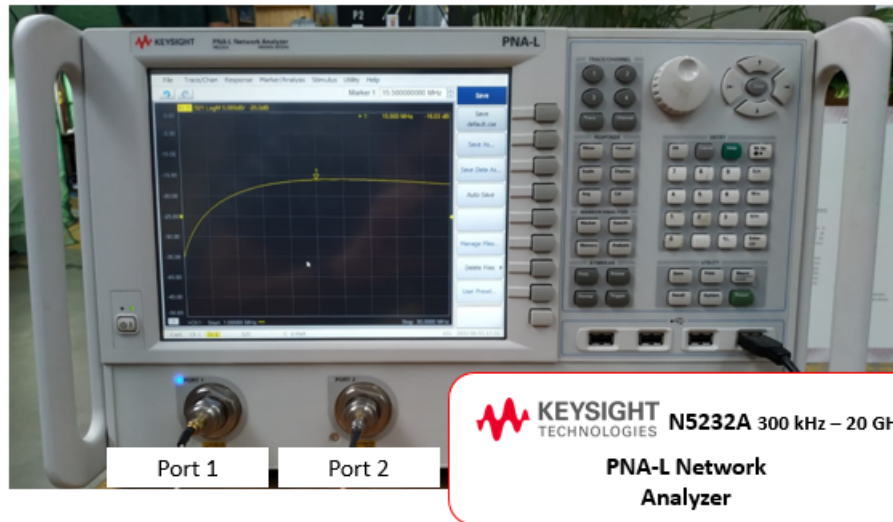
The Measurements of the Mutual Inductance have been realized with a frequency range from 1 to 30 MHz, and the instrument used is shown below:



$$M = \frac{10^{\frac{M_{dB}}{20}}}{2\pi f} \text{ (H)}$$



# APPENDIX E – Measurement Setup of the S-Parameter of the System



# APPENDIX F – ADS Simulation

ADS simulation of the circuit in Figure 4.21:

